UNIVERSITÀ DEGLI STUDI
DI GENOVA

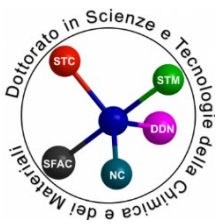

Exploiting Cation Exchange Reactions in Doped Colloidal NIR Semiconductor Nanocrystals: from synthesis to applications

by Irene Rosina

a dissertation for the degree of

Doctor of Philosophy in Science and Technologies of Chemistry and Materials

Curriculum: Nanochemistry

XXXII cycle

Supervisors:

Prof. Liberato Manna (IIT),

Dr. Luca De Trizio (IIT),

Prof. Paola Riani

Dipartimento di Chimica e Chimica Industriale

Università degli Studi di Genova

Genova, Italy,

10 September, 2020

Index

Thesis abstract

Colloidal quantum dots (CQDs) have tunable optical properties through manipulation of their size, shape, and surface chemistry. Among pholuminescent QDs, near-infrared (NIR) emitting ones are of particular interest since they can be used in several applications, from the labeling in living tissues, to the integration in commercial optoelectronic devices, like photovoltaics for solar energy conversion or photodetectors from visible to the near-infrared and mid-infrared. In addition, the exciting promise of CQDs is that is associated with easy and low-cost device fabrication process. In fact, solution-based techniques like spin-coating, dip coating and ink-jet printing are typically used for solution CQDs readily to be used in large-area processing techniques.

Thus, to obtain an ink solution of nanocrystals (NCs) ready to be used in device fabrication process, in this thesis, cation exchange (CE) reactions have been used as a convenient tool to finely transform NCs directly in solution or deposited as thin films. These reactions allow to substitute a fraction or all "host" metal cations of pre-synthesized NCs with new "guest" cations while preserving both NCs' size, shape and, typically, crystal structure. Depending on the miscibility of the reactant and product materials, and on the kinetics of the CE reaction, different types of nanostructures can be accessed ranging from alloy NCs, doped systems, dimers, core@shell (or core@graded-shell) heterostructures even with elaborated architectures (i.e., quantum wells, multiple-cores@shell). Unlike ion substitution in solids, cation exchange at nanoscale results in fast reaction rate and an easy modulation of the thermodynamics through selective ion coordination in solution.

This study provides an overview of the CE on semiconductor NCs, in particular on II-VI, I-III-VI_2 and III-VI compounds. We first explore the exchange between cadmium chalcogenides and mercury ions to produce $Cd_{1-x}Hg_xTe$ CQDs which can be potentially employed in NIR photodetectors and photovoltaic devices. Our developed synthesis is a result of a wide systematic investigation process, in which we varied specific physical parameters, such as the reaction temperature, the feed molar ratio of the precursor and the solvent. More specifically, these aspects were studied to have control on the size, shape, surface composition and crystalline phase after mild conditions of annealing into stable connected crystals. This peculiarity could be exploited to boost the photogenerated charges diffusion in polycrystalline photoconducting films fabricated by means of an ink of NCs solution.

Additionally, another aspect studied was the surface passivation of $Cd_{1-x}Hg_xTe$ colloidal NCs, in order to understand how to optimize the charge transfer efficiency among the nanocrystals. The carrier transport in QD devices differs fundamentally from band transport in bulk

semiconductors. In nanocrystal film it is of fundamental relevance to improve the mobility of the photogenerated charges. Noteworthy, the granularity of the system and the consequent coupling between adjacent dots can produce additional physical parameters, as charge recombination. The carrier diffusion length can be limited by trapping sites[1]. To overcome these limitations, post-synthetic strategies that couple the high quality NCs solutions with ideal properties (band gap, absorption, monodispersivity) and high-quality films (quantum dot packing, passivation, and absorptive/conductive properties) are necessary. Indeed, to improve the inter-NCs conductivity in a NC film, ligand exchange and stripping procedures are widely used, with the aim of replacing insulating surfactants with more conductive species. These procedures have some drawbacks, for example metal cations can desorb from the surface of the NCs during the stripping. On the contrary, here we will show how our nano heterostructures (NHCs) enable to avoid the post-process ligand stripping and to perform the final annealing step in milder conditions.

Above these considerations, CE can be exploited to address NCs solution through surface uniformity from the nano- to the macroscopic scale. This is the first step toward electronic coupling between the separate building blocks of nanocrystals.

Apart from III-V QDs, we shifted our research activity on valid alternative material which do not contain toxic heavy metals such as Cd, Pb, As or Hg, and that offer a high flexibility for tuning band gap in the NIR window. In chapter 5, the results about the study of a III-V system are reported. Thus, we studied InP system, which is probably the only one that could provide a compatible emission color range similar to that of Cd-based QDs but without intrinsic toxicity. Nevertheless, the synthesis of III-V NCs, due to their covalent-bond character, is limited by long reaction times or an uncontrollably fast nucleation that may lead to the formation of amorphous or bulk compounds. The role of our work is to explore the reported InP synthesis and to further improve the luminescent properties of these systems Here we study the effect of different parameter (molar concentration in reaction mixture, the use of different phosphorous precursors) to enhance the control over the particle size and size distribution. After that, we studied different Sulphur source precursors to obtain InP@ZnS core@shell NCs with high quantum Yield (QY).

In the last chapter, we describe also I-III-VI_2 system as $CuInS_2$ for photoluminescence modulation. In this Chapter Copper Indium Sulfide nanocrystals are prepared using a single-step heating up method relying on the low thermal stability of ter- dodecanethiol used as stabilizing agent, solvent, and sulfur precursors. The obtained particles exhibit an emission varying from 710 to 940 nm. This range depends on the extent of the heating time (pre-heating)

before the threshold temperature of 230°C for the growth process of ternary semiconductor NCs such as of CIS nanocrystals. Afterwards we report on the procedure for the growth of a ZnS shell, which enables a blueshift of the PL emission wavelength with respect to those of their parent CIS, due to the widening of the band gap for the entrance of zinc ions into the CIS structures.

Chapter 1. Introduction

1.1 Nanocrystals: definition

With the term nanocrystals (NCs) one refers to a class of materials having a size ranging from around 1 to 100 nm, consisting of hundreds to few thousands of atoms, at the same time preserving crystal structure of their bulk counterparts.[2] Typically, they are composed of metal, metal oxide and semiconductor materials, and their combination in various heterostructures.[3–5] In a range where the number of atoms starts to be reduced, certain material properties such as electronic, optical, magnetic and chemical, start to become very different from the properties of their bulk counterparts. This aspect can be considered as an additional feature which led the scientific community to "go nano" because it would allow an extra tunability. It would therefore be possible to alter optical and conductive properties of a material by altering its size in the nanoscale range rather than adjusting its composition or its molecular structure. Now the scientific community has an excellent understanding of how the nanoscale influences the properties of nanocrystals, but they are still far from transposing NCs from laboratory studies to industrial commercialization as fundamental building blocks for transistors light emitting diodes, lasers, and solar cells. The goal is, therefore, to have a full control over the shape and size and composition of the colloidal NCs and to arrange and interconnect them in complex low-cost architectures.

In this introduction section, we will report a brief history of nanocrystals. We will try to explain with a few examples why the behavior of nanoscale materials can be very different from that of their bulk and their atomic counterparts and how quantum mechanics can help us in rationalizing this. Following this discussion, we will give a definition of .quantum dot. We then follow a bottom-up approach and give a simplified picture of a solid as being a very large molecule, where the energy levels of each individual atomic component have merged to form bands. The electronic structure of a quantum dot, being intermediate between the two extreme cases of single atoms and the bulk, will then be an easier concept to grasp. A free electron gas model and the concept of quantum confinement will be used to explain what happens to a solid when its dimensions shrink one by one. This will lead us to a more accurate definition of quantum wells, quantum wires and quantum dots. Finally, we will examine in more detail the electronic structure of quantum dots, although we will try to keep the level of the discussion relatively simple.

1.2 Brief history of nanocystals (NCs)

Although nanomaterials have played a pivotal role in the advancement of nano / bio / info technology to date, their history began immediately after the Big Bang, when nanostructures formed in early meteorites and later evolved in many other nanostructures, such as seashells and skeletons. Obviously, first-hand nanotechnologies and nanomaterials appear as accidental discoveries of ancient artisans without a deep knowledge of their nature and structure. The first trace of the history of the use of nanomaterials dates back more than 4000 years ago in ancient Egyptian times when they uses lead salts for cosmetics and hair darkening (see Figure 1.1).[6]

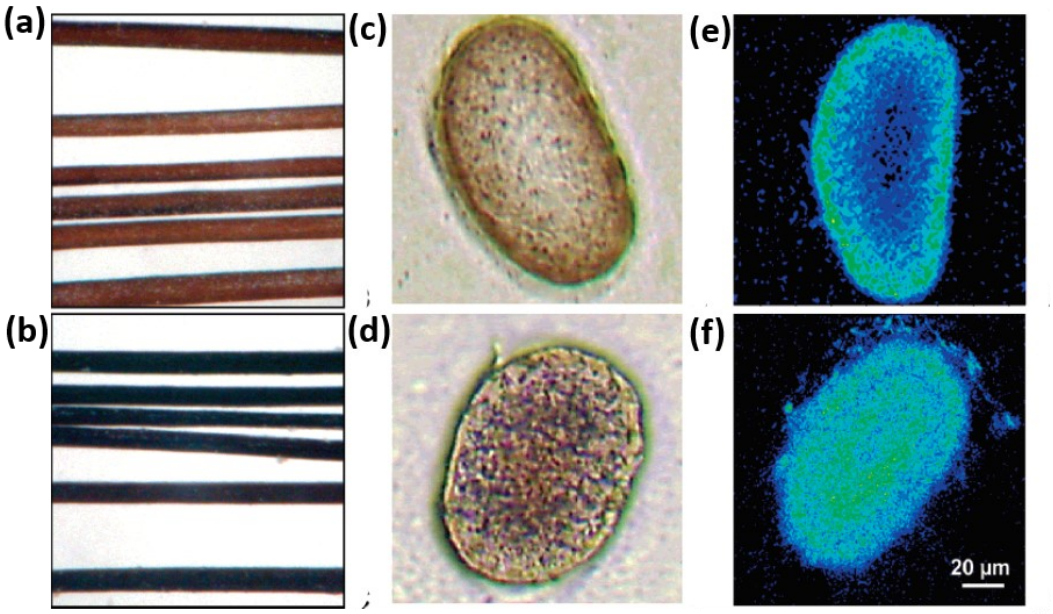

Figure 1.1. (a) (b) Optical macrophotographs of hair from brown to black color (c) (d) microphotographs of hair cross sections showing blackening during treatment with lime and lead oxide in water. (e) (f) Pb maps of the respective treated samples obtained by SEM-EDX after 6 and 72 hours, showing a progressive radial fixation toward the center of the hair. Adapted partly from

It was recently demonstrated that Pb salts and lime mixture reacts with sulfur present in hair's keratin proteins to form lead sulfide (PbS) nanocrystals of the size of ~5 nm which are very similar to PbS nanocrystals that can be synthesized by modern approaches. [6]

There are still some very fascinating examples of ancient artifacts created with nanocrystals even in Roman Era [7,8], when colloidal metals of tin oxide, silver and gold were used as coloring in glass and textiles. One of them is the well-known "Lycurgus" glass cup, a decorative Roman treasure of the 4th century AD characterized by the red color under transmitted light (light source within the cup) and by the green color under reflected light (external light source) (see Figure 1.2).[8]

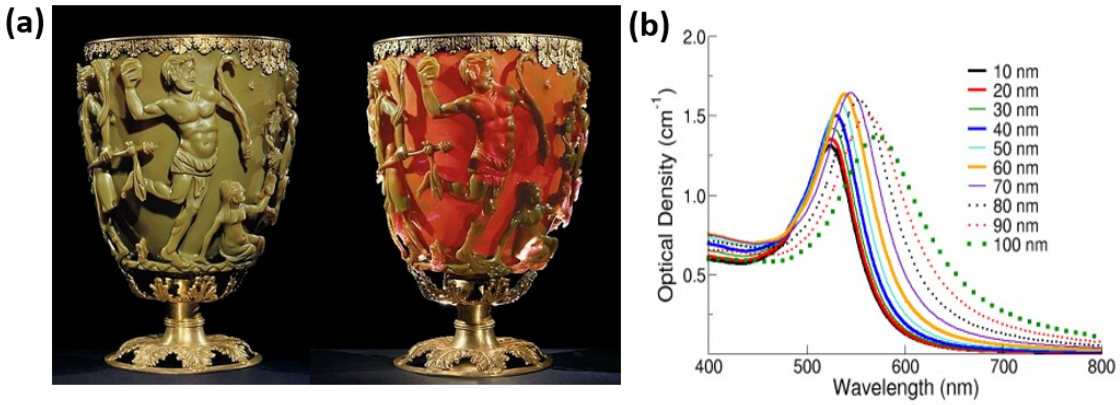

Figure 1.2. (a) Lycurgus cup showing different color depending on the way the light passing through it. The glass contains gold-silver colloidal nanoparticles (adapted from Atwater et al. (2007)). (c) optical density to measure the refractivity of the gold nanoparticles. Gold nanoparticles' interaction with light is strongly dictated by their environment, size and physical dimensions. Smaller monodisperse gold nanoparticles absorb light in the blue-green portion of the spectrum while red light is reflected,giving a rich red color. As particle size increases, absorption shifts to longer, redder wavelengths(known as red- shifting). Then red light is then absorbed, and green-blue light is reflected (Adapted from http://www.sigmaaldrich.com/materials-science/nanomaterials/goldnanoparticles).

This phenomenon wasn't clarified until 1990, when scientists studied the cup and concluded that this dichroism is due to the presence of silver and gold nanoparticles up to 100 nm, dispersed in the glass matrix.[9] Their interaction with light strongly depends on their environment, size and physical dimensions. Gold gives a red color when using an internal light source. This because the larger nanoparticles in the glass absorb short wavelengths (green and blue~520 nm) while the red component penetrates through the glass. The green color is due to the light scattering by colloidal dispersions of silver particles with size bigger than 40 nm. [9–11]

Besides the Egyptians and Romans, gold and silver nanoparticles have been used for centuries by artisans for their vivacious colors produced by their interaction with visible light: medieval artisans also studied to manufacture stained glass (colored glass) windows by incorporating metal particles in them (see Figure 1.3).[12] History, thus, includes a multiplicity of examples in which ancient culture already understood the potential applications of colloidal dispersion, but they did not have science-based explanations.

However, the study of nanomaterials began more recently, in 1857 when Michael Faraday reported on the synthesis of colloidal gold particles, which he called "activated gold" and when he revealed the color of these colloidal nanoparticles are very dissimilar compared to their respective bulk counterpart.[13] This was the first study observing size dependent effects of nanoparticles (quantum size effect). The explanation behind the different colors of metal

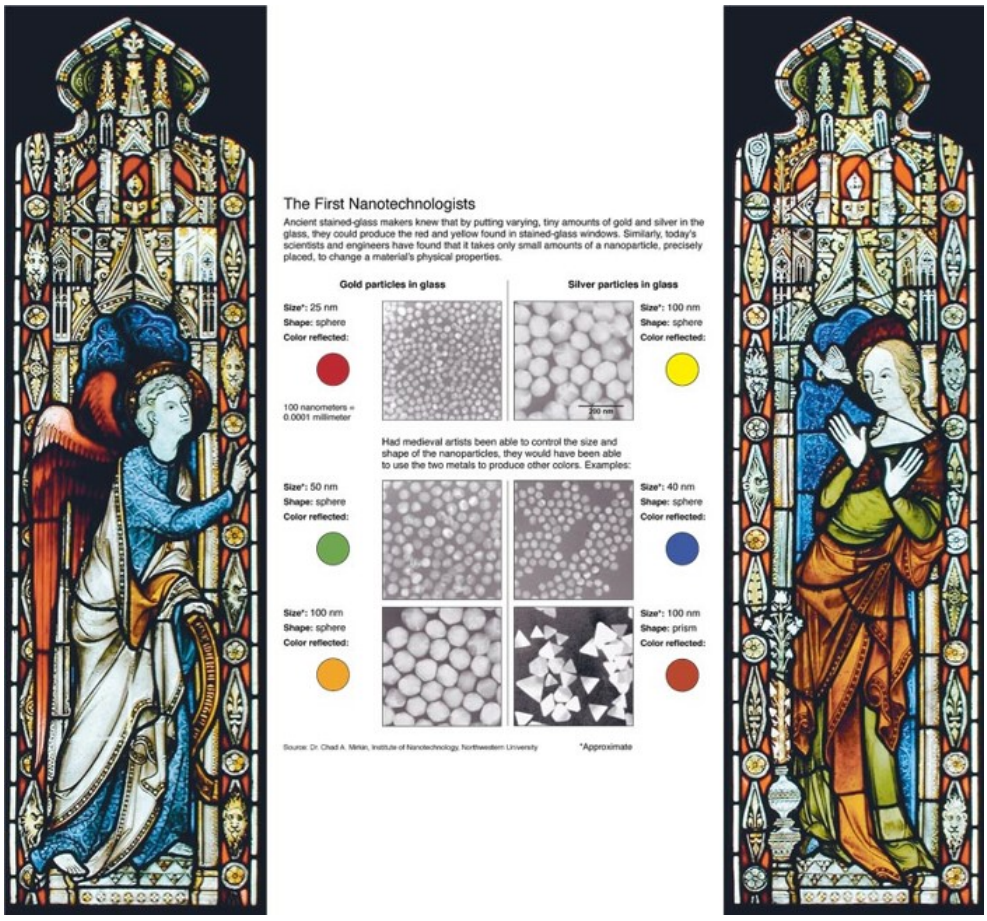

Figure 1.3. Notre Dame Cathedral's famous stained-glass windows. They owe their color to the effect of gold nanoparticles. The artisans of stained glass for medieval cathedrals across Europe had recipes for their glass, casting soluble gold into the glass mixture during its manufacturing. They knew that only particles of certain very small sizes gave vivid colors but they didn't know why. Figure reproduced from Ashby at al. (2009).

colloids [14] was later clarified by Mie (in 1908) which gave the basis to the optical properties size-dependent metallic particles, and soon afterwards extended by Richard Gans for gold particle in 1912 [15] and silver particles in 1915.[16]

The first size dependent optical properties of semiconductor NCs were reported in the 1920s for CdS NCs.[17] G. Jaeckel found that the growth of CdS particles inside the glass shifted the absorption and luminescence color to longer wavelengths. Then, F. Hamiltonian and R. Kubo contributed new theories and predicted that colloidal NCs have different electronic properties compared to macroscopic materials.[18] In the 1960s, size dependent phenomena were also observed in other semiconductor materials. C. R. Berry pointed out that the absorbance wavelengths of AgBr NCs[17,19] and AgI NCs[20] shifted to shorter wavelengths as compared to bulk AgBr and AgI. In 1982, A. L. Efros introduced a simple model to explain the influence of size quantization on interband absorption in a spherical semiconductor NCs. At the same time A. Henglein[17,21] reported on the surface chemistry, photodegradation, and the catalytic processes shown in colloidal semiconductor particles. This is the first work where the

absorption spectrum of colloidal solutions of CdS NCs was revealed. In 1983, L. E. Brus first interpreted explicitly that this absorption behavior was a quantum mechanical effect.[22,23] By tuning the size and controlling the size distribution of CdS NCs, he observed a blue shift of the absorption of CdS NCs compared to bulk CdS.

Meanwhile, at the beginning of the 1940ies, nanoparticles found their way to the production and consumption when U.S. and Germany replaced ultra-fined carbon black for rubber reinforcement with precipitated and fumed silica nanoparticles.

As a result of the new understanding over recent decades of how the size reduction may affect a whole range of new physico-chemical properties, research has expanded exponentially in the field of nanocrystals with many future potential applications and economic impacts.

1.3 Chemical and Physical Properties of NCs

In order to better understand the potential of nanoscale material, it is important to comprehend how the properties of a nano-crystalline material are affected, limiting its crystalline structure in one, two or three dimensions.[24] Indeed, while the chemical and physical properties of a bulk crystal are independent of the size and are only chemical composition-dependent, everything changes when the size of a crystal decreases to the nanometer regime. In this case the size of the particle begins to modify the properties of the crystal such absorption, fluorescence, melting point, phase stability, catalytic activity, magnetism, electric and thermal conductivity, which differ considerably from those of the corresponding bulk material. [25] Here we illustrate some of the fundamental concepts used in this thesis and recalls the fundamental definitions of semiconductors and nanocrystal semiconductors, as well as the fundamentals of how their size can alter the electronic properties. These will explain how to control the optoelectronic properties of nanocrystals by adjusting their size without changing the chemical composition. The reason at the base of the unique chemical and physical properties of nanocrystals are: (i)the ratio of surface atoms to inner atoms is much higher than that of bulk solids, then relative surface area increases;(ii)the charge carrier motion is restricted to a small material volume;(iii)the number of unit cells in a single nanocrystal is small.

1.3.1 Size-dependent properties of semiconductor nanocrystals: Quantum size effect

To understand the properties of semiconductors nanocrystals is essential to pay attention to their electronic structure. To understand this, different theoretical approaches have been

studied by researchers. In one approach, called "bottom-up" perspective, the properties of the larger QD are built up from the sequential addition of individual atoms to a core particle. Historically limited to very small QDs, this approach became increasingly important with the increase in the available computational power allowing calculations on QDs made up of hundreds of atoms.[26] Alternatively, it was also studied a "top-down" view. Here the properties of the larger crystal are influenced by the finite size of the QD. Due to the analogies with familiar quantum mechanical model of the particle in a box, this approach has proved to be particularly useful and provides a convenient basis for a fundamental understanding of QD photophysics.

1.3.1.1 Bottom up approach: linear combination of atomic orbital theory - molecular orbital theory (LCAO-MO)

Discussing the properties of nanocrystals, chemists may prefer to a bottom up approach by considering nano objects as large molecules (where physicists see them usually as small crystals) and calculating the evolution of the electronic structure from atoms to QDs to bulk materials and predicting the dependence of bandgap on size of the crystals.

The basic premise of the atomistic approach is that the wavefunction, ψ, of any crystal system composed by N atoms, can written from a linear combination of atomic orbitals (LCAO or Hűcker theory)[7]:

$$\psi = \sum_{i,a} \varphi_{i,a} \qquad (1.1)$$

With $\varphi_{i,a}$ is *a*-th atomic orbital of atom *i*.

Given the wavefunction defined by Eq.1.1, the energy levels ε of a system is:

$$det|H - \varepsilon S| = 0 \qquad (1.2)$$

Where H is the Hamiltonian matrix and S is the overlap integral defined by:

$$S = \int \varphi_{i,a}\, \varphi_{i,b}\, dx \qquad (1.3)$$

Different approaches exist to solve Eq 1.1. One typical assumption is to limit the sum only to valence atomic orbitals. This considers only the Hamiltonian matrix elements of σ and π atomic

orbital interaction (i.e. s-s and p-p respectively) occurring between first and second neighbors and neglecting other interatomic overlap integrals.[27] Considering a diatomic molecule, the atomic orbitals (AO) of two individual atoms are combined, producing bonding and anti-bonding molecular orbitals (Figure 1.4).

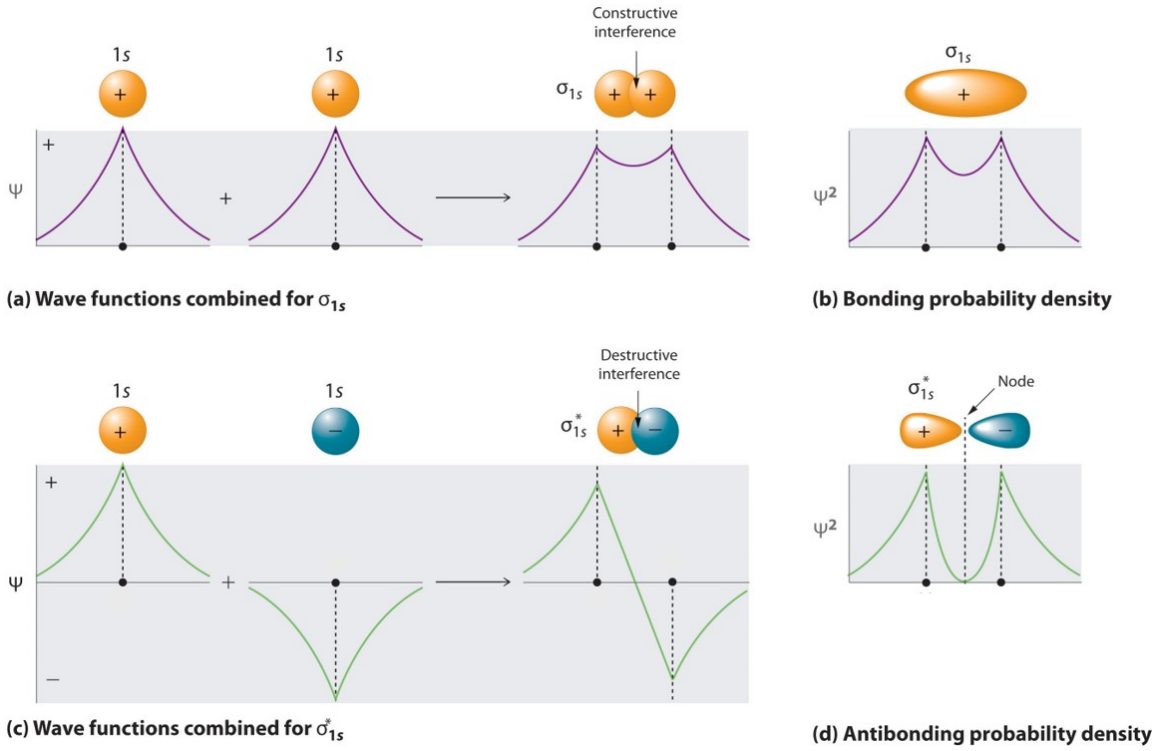

Figure 1.4. Molecular Orbitals for the H_2 Molecule. (a) formation of a bonding σ1s molecular orbital for H_2 as constructive linear combination of atomic orbitals of two H 1s atomic orbitals (b)in the resulting bonding molecular orbital the square of the wave function (Ψ^2) illustrates the increased electron probability density between the two hydrogen nuclei (c)) formation of an antibonding molecular orbital σ*1s as the deconstructive linear combination of atomic orbitals difference of the wave functions (Ψ) of two H 1s atomic orbitals. (d) resulting bonding molecular orbital where the square of the wave function (Ψ^2) for the σ*1s illustrates the node corresponding to zero electron probability density between the two hydrogen nuclei.

As the number of atoms increase, the discrete energy band structure changes from large energy steps to small energy steps, hence to a more continuous energy band. The occupied (bonding) molecular orbital quantum states (equivalent to the valence band) are called the highest occupied molecular orbital (HOMO) levels. The unoccupied antibonding orbitals (equivalent to the conduction band) are called the lowest unoccupied molecular orbital (LUMO) levels. The energy difference between the top of the HOMO and bottom of the LUMO (known as band gap, Eg in Figure 1.5), where there are no allowed energy states, increases and the bands split into discrete energy levels of reduced mixing of AOs for a small number of atoms. Therefore, the small NCs' electronic band structures result in an intermediate between atomic/molecular and bulk crystalline with quantized energy levels. The LCAO-MO model

provides a methodology to calculate the electronic structure for smaller NCs, however, it cannot be used to calculate the energy levels of larger NCs due to mathematical complexity and limitations of the computing systems.

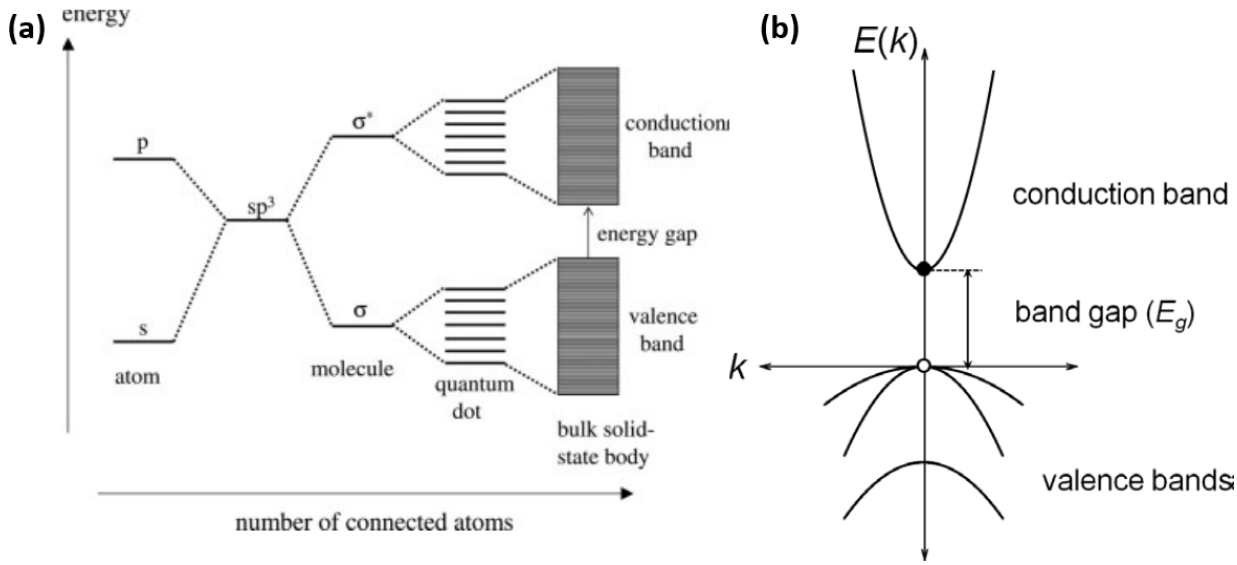

Figure 1.5. (a) formation of energy bands from atomic orbitals: as the number of atoms increase, the spacing between energy levels decreases. Ina bulk solid, a macroscopic crystal containing 1023 atoms, the spacing is sufficiently small that the energy levels may be treated as a continuous energy band, rather than a discrete energy level. (b) Dispersion curve for a general semiconductor near k=0. The energy bands scale as k^2 and a gap opens between the bands where no energy states exist (Eg)

The quantum size effect (also called size quantization effect or quantum confinement) takes place only in semiconductor NCs and metal NCs with sizes usually smaller than 10 nm[21,23,28]. In general, all NCs' electronic structure can be described as intermediate between discrete energy levels of an atomic/molecular system and the continuous band structure of a macroscopic bulk materials. This fact can be well understood looking at Figure 1.6, which compares the different energy diagrams. It is observed that, as the size decreases, the continuous bands of the macroscopic solids are modified by the appearance of discrete energy levels and the widening of the forbidden energy gap.

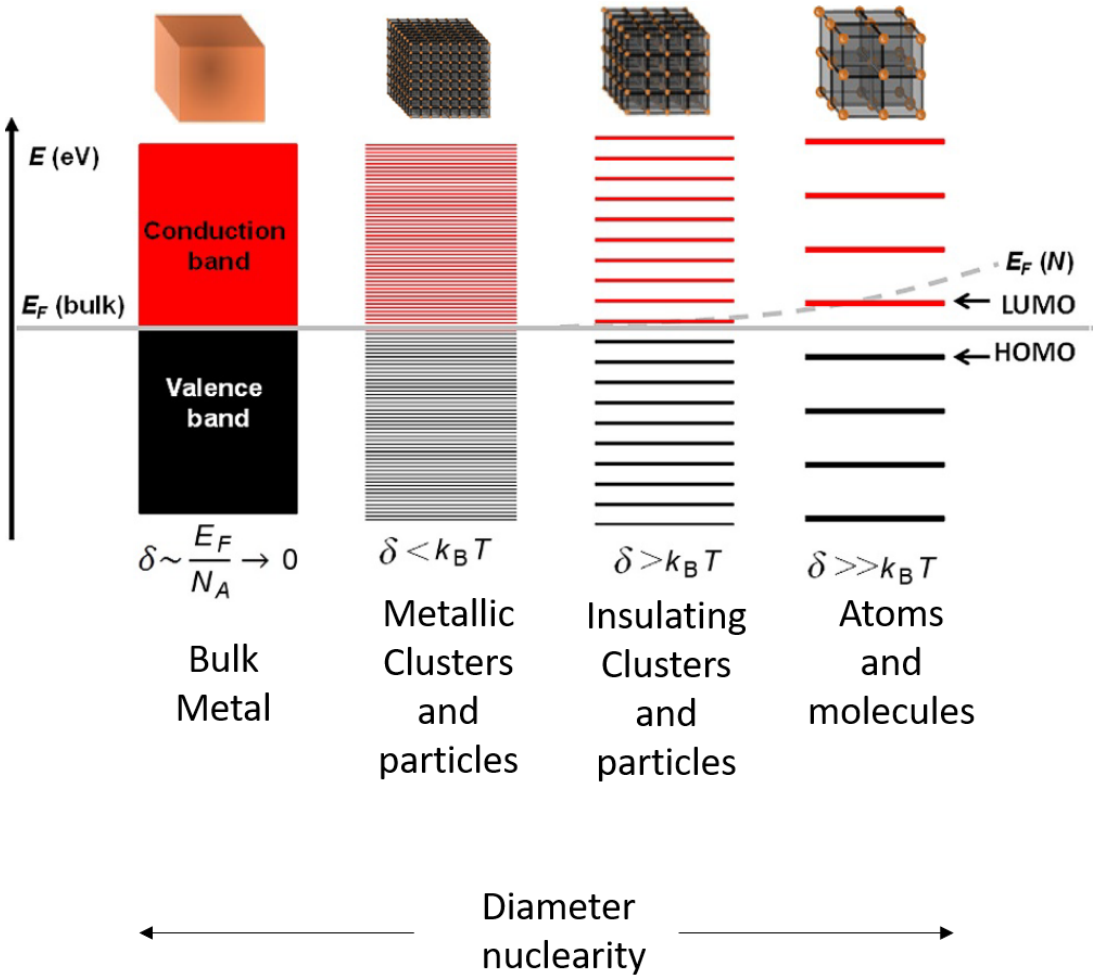

Figure 1.6. Evolution of the electronic structure and density of states as the number of atoms decreases from bulk material to QDs of different size (from left to right).δ is the so-called Kubo gag. Confinement leads to size-induces discretization of energy levels resulting in an increasing of energy gaps. Figure partially adapted from Colloidal Foundations of Nanoscience[29]

1.3.2 Top-down approach

Physicists apply the band theory of macroscopic solids to nanocrystals describing the behavior of the charge carriers as a free electron gas within a bulk crystal. The model assumes that the crystalline structure of a bulk metal solid is composed by a positively charged background due to nuclei and core localized electrons, with a gas of delocalized electrons. Instead of bands they talk of delocalized molecular orbitals, and the Kubo gap becomes the HOMO–LUMO gap. In such a view it is obvious that high cluster symmetry leads to correspondingly degenerate molecular orbitals.

1.3.2.1 Electron-confinement: particle in a box model and the effective mass approximation

The band theory considered the solid to be of infinite size, so that the contribution of the surface atoms can be neglected. This approximation cannot be acceptable in the case of a NC where

the ratio of surface atoms to inner atoms is high and this latter contributes to the total potential of the solid. When the size of the crystal become comparable to the De Broglie's wavelength associated with the particle interacting with it, the motion of the charge carrier is strongly confined within the structure. The description of their behavior has, therefore, similarities with the quantum problem of the particle in the box by the resolution of the Schrödinger's equation associated with it. This approach allows to obtain a discretization of energy levels in the vicinity of the bands, which is a distinctive feature compared to the continuous energy levels associated with the corresponding bulk.

To illustrate the effects of confinement, quantum mechanics is a powerful tool with the free electron confined in a box model. The simplest form of the particle in a box model considers a one-dimensional system and was proposed by Efros [21]in 1982 and later modified by Brus[23]. The walls on one-dimensional box can be visualized as regions of space with an infinitely large potential energy (see Figure 1.7). Conversely, the interior of the box has a constant, zero potential energy. This implies that the particle inside the box is not influenced by any force and it can move freely in that region. However, the particle is repelled by infinite forces if it touches the walls of the box, preventing it from escaping.

The potential energy is given by:

$$V(x) = \begin{cases} 0, & 0 < x < L \\ \infty, & otherwise \end{cases} \qquad (1.4)$$

Where L is the length of the box and x the position within the box.

A general description of any quantum mechanical system can be done by formulating the time-dependent Schrödinger's equation:

$$-\frac{\hbar}{2m}\frac{\delta^2}{\delta x^2}\varphi(x,t) + V(x,t)\varphi(x,t) = i\frac{h}{2\pi}\frac{\delta}{\delta t}\varphi(x,t) \qquad (1.5)$$

Where the first term of the equation is the kinetic energy, the second is the potential energy of the forces acting on the system, and the third comprises the total energy. For the case of a non-reacting systems, the potentials are time-independent, and the equation can be simplified as:$\varphi(\mathrm{x},\mathrm{t}) = \psi(\mathrm{x})\ \mathrm{T}(\mathrm{t})$.Then:

$$-\frac{\hbar}{2m}\frac{\partial\delta^2}{\partial\delta x^2}\psi(x) + V(x)\psi(x) = E\psi(x) \qquad (1.6)$$

Thus, an electron whose momentum depends only on its kinetic energy and whenever is confined in a limited region. It will have only a finite set of quantum mechanically allowed discrete states. The only possible solutions allowed by Eq.(1.6) are standing waves with discrete nodes in between of which the electron presents the maximum probability of being located:

$$\psi(x) = [A\,sin(kx) + B\,cos(kx)]\,e^{-i\omega x} \qquad (1.7)$$

Where ψ is the wavefunction of the particle at position x, A and B are complex number, k is the wavenumber $k=\frac{n\pi}{L}$ with n=1,3,5,…$\in N$ and ω is the frequency.

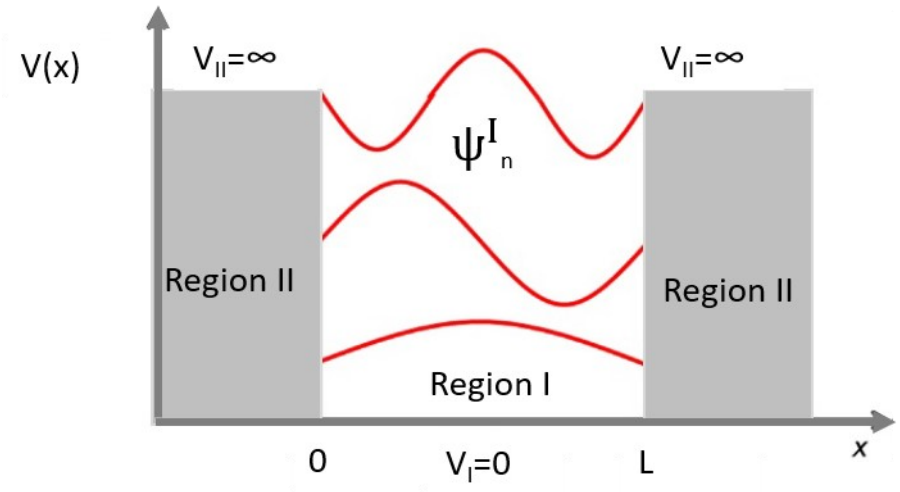

Figure 1.7. the one-dimensional case sketch of a box limited in the x-dimension by infinite potential barriers, which mathematically define the physical orders of the box

The energies which correspond with each of the permitted wavenumbers may be written as:

$$E_n = \frac{n^2\hbar^2\pi^2}{2\,mL^2}=\frac{k^2\hbar^2}{2m^*} \qquad (1.8)$$

Where $\hbar^2$ is the Planck's constant, k the wave vector and m* the effective mass.

Of course, the QDs differ from the particle in the case of an ideal box and some small adjustments to the above equations are needed. Firstly, QDs are three-dimensional and spherical rather than one-dimensional and square. Then Eq.(1.8) becomes:

$$E_n = \frac{n^2\hbar^2\pi^2}{2\,mR^2} \qquad (1.9)$$

Where R is the radius of the QD.

Second, there are actually two particles within each QD rather than just on (the electron and the hole):

$$E_n = \frac{n^2\hbar^2\pi^2}{2\,m_eR^2} + \frac{n^2\hbar^2\pi^2}{2\,m_hR^2} = \frac{n^2\hbar^2\pi^2}{2\,m^*R^2} = \frac{k^2\hbar^2}{2m^*} \qquad (1.10)$$

Finally, the QD box is not empty but is filled with a semiconductor:

$$E_n = \frac{n^2\hbar^2\pi^2}{2\,m^*R^2} + E_g \qquad (1.11)$$

In the effective mass approximation model, the Eq.(1.8) is assumed to hold an electron or a hole in the semiconductor, therefore energy band is parabolic near the band-edge. The shift of band-gap energy (ΔE_g) due to the confinement of the exciton in a QD with a diameter R can be expressed as following:

$$\Delta E_g = \frac{\hbar^2\pi^2}{2\,\mu R^2} - \frac{1.8e^2}{2\varepsilon R} = \frac{\hbar^2\pi^2}{2\,R^2}\left(\frac{1}{m_e} + \frac{1}{m_h}\right) - \frac{1.78e^2}{\varepsilon R} - 0.248\,E_{Ry}^* \qquad (1.12)$$

Where μ is the reduced mass and E_{Ry}^* is the Rydberg's energy $E_{Ry}^* = \frac{\hbar^2}{2\,\mu}$.

The first term represents a relation between the confinement energy and the radius of the QD (R), whereas the second term shows the Columbic interaction energy with a 1/R dependence. The Rydberg's energy term is size independent and is usually negligible, except for semiconductors with small dielectric constant.

The model of an electron in a box described above, in its simplicity captures the essentials of real systems with confined free electrons: the energy levels and spacing among levels increase in magnitude when confinement becomes more restrictive.

1.3.2.2 Top-down Density of states (DOS)

The model above is a first approximation to describe the energy bands using the calculation of the Density of states (DOS). The lowest unoccupied and highest occupied energy levels in the molecule evolve in the crystal to form the conduction band and the valence band, respectively, which are separated by a characteristic gap in which there are no allowed energy states, known as the band gap Eg. Since each of N atoms contributes with its atomic states to a band (valence electrons), the DOS, ρ, of a semiconductor is basically proportional to the number of atoms and it scales with the dimensionality, d, as described by:

$$\rho\,(E) \propto \sqrt{E^{(d-2)}} \qquad , d=1,2,3 \qquad (1.13)$$

Where E is energy.

The situation changes when the solid is not infinite anymore along the three dimensions x, y and z. In a quasi bi-dimensional system, i.e. infinitely extended in x and y directions, and with a z dimensions of few nanometers, quantization effects are due entirely to the confinement of the charge carriers in the z-direction ("quantum well" or an infinite sheet). In this case, the particle in a box model has an infinite potential along z axis and the solution of the Schrödinger equation are the standing waves:

$$\psi(z) \propto A\,sin(k_z z) \qquad , k_z = \frac{n\pi}{d_z} \qquad , n \in N \tag{1.14}$$

Then, for this system the energy levels are quasi-continuous along x-y plane but assume only certain values quantized along the z direction. The level spacing is inversely proportional to the thickness of the material. Thus, the DOS is defined by a step function where the energy levels are quasi-continuous with respect to k_z (each step) losing its dependence from energy, E. In the case of a one-dimensional system ("quantum wire"), the confinement is in two directions, for example along y and z. In this case the density of states $\rho\,(E)$ depends on $\frac{1}{\sqrt{E}}$ .Each hyperbole branch defines a continuous k_x state distribution and a discrete k_y and k_z state distribution. Two-dimensional quantization has significant implications for the transport of charges. Electrons can move freely along the x-axis with quasi-continuous energy levels, but discrete states along y and z can be occupied by them. So, they act as discrete channels of conduction.

In the last case of a zero-dimensional solid where the confinement extends to the three dimensions (“quantum dot” or quantum points) also the electrons freedom is restricted in all directions. The allowed k states are discrete and the distribution $\rho\,(E)$ appears as a delta function δ for allowed energy levels being very similar to that of an atomic system (see Figure 1.8)

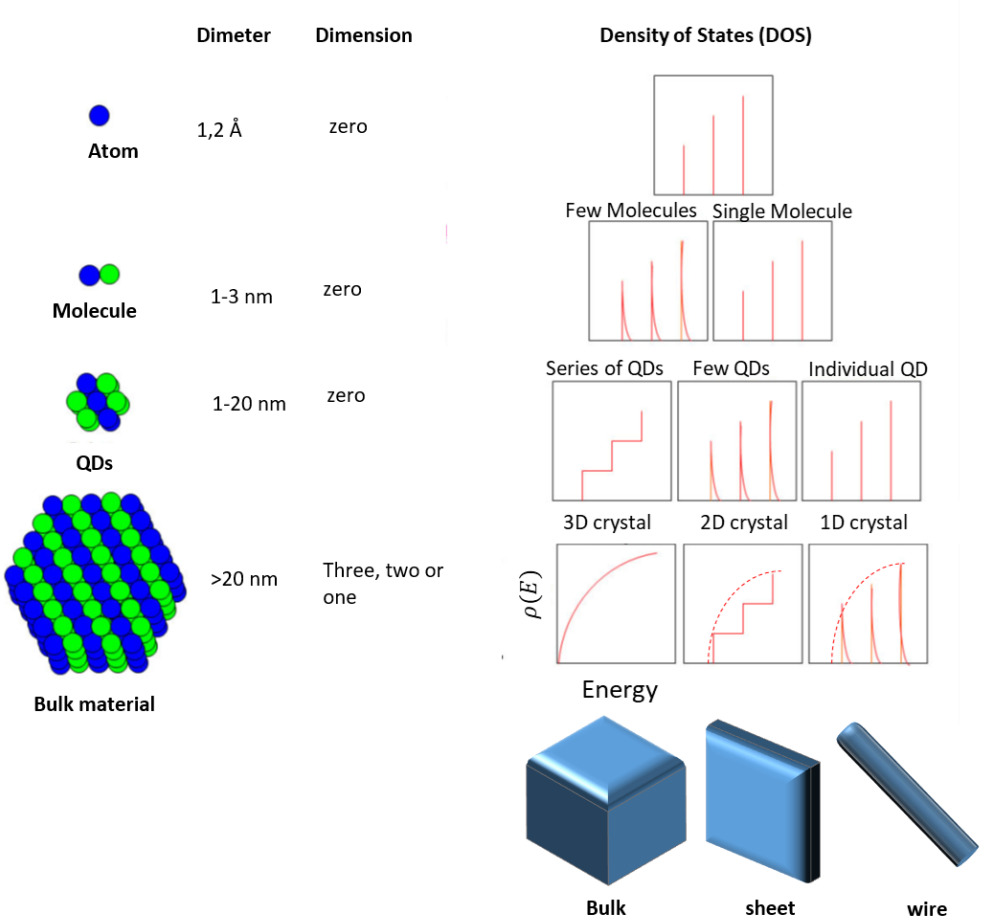

Figure 1.8. Density of energy states of electrons in an atom and crystals od increased dimensionality. The dotted line in the two-,one- dimensional structure indicates the corresponding density of states from a macroscopic crystal. In zero-dimensional crystal QD, the density of states is a set of delta functions. Adapted from Bera et al. [30]

An important threshold is reached when the gap between the highest occupied and the lowest unoccupied state (called the Kubo gap d) equals thermal energy.[29] When electrons get thermally excited across the Kubo gap, a low temperature insulator becomes a semiconductor and at higher temperatures a metal. In this case, also the magnetic properties of small clusters can change dramatically. This non-metal-to-metal transition can take place within a single incompletely filled band, or when two bands begin to overlap because of band broadening. The development of the DOS with cluster size is illustrated in Figure 1.6

1.4 Semiconductors Nanocrystals Quantum Dots (NCs QDs) properties

The absorption of a photon (light) is one of the possible way an electron from valence band (VB) can be moved to the conduction band (CB), as shown in Figure 1.9. An electron from the VB attains sufficient energy to overcome the energy gap and moves to the conduction band, leaving a hole behind. This excited electron and holes forms a part of the charge carriers in semiconductor devices and moves through defect states (which lie below the CB or above the

VB) where they relax and recombine after a finite time with release of energy. This excess of energy may be radiative (with emission of photons) or non-radiative (emitting phonons or Auger electrons).

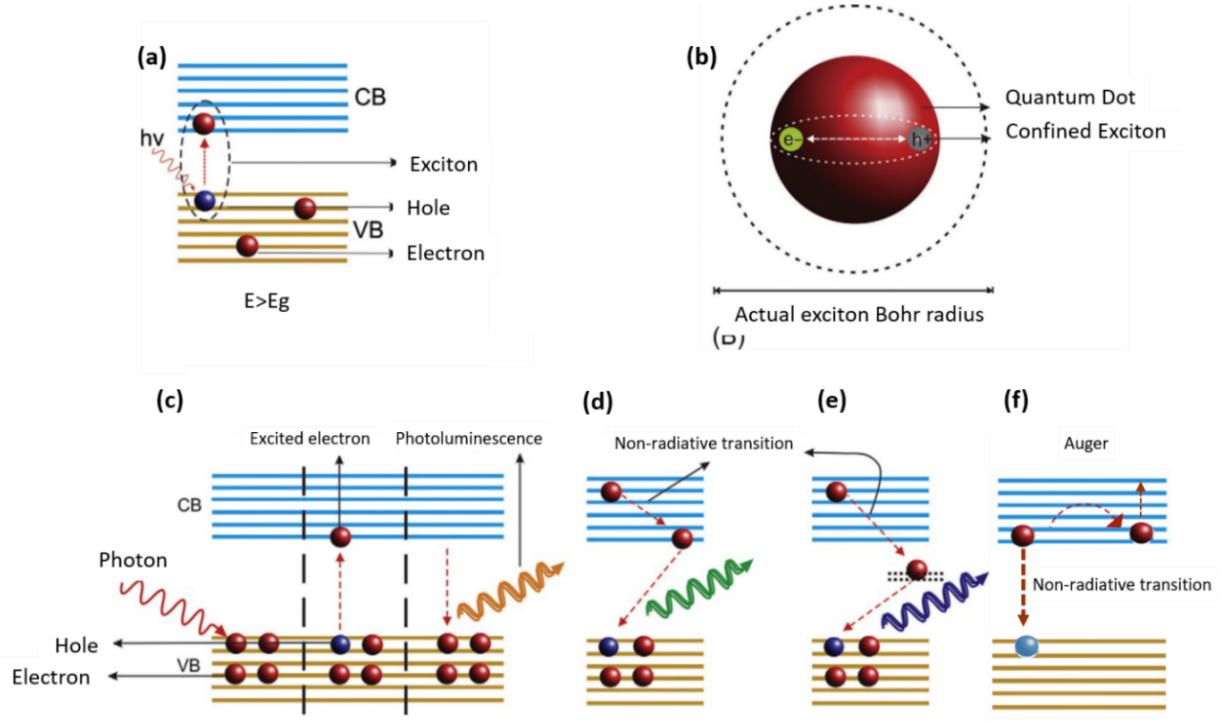

Figure 1.9. Interaction of semiconductors with photons (a) Photon absorption and exciton formation in QD energy band. (b) exciton radius vs QD size The Bohr radius is the distance in an electron-hole exciton. Every semiconductor has a characteristic exciton Bohr radius (distance electron-hole) below which the quantum confinement effect realized. This unique property causes "band" of energies to turn into discrete energy levels in QDs. Modified from Kasap et al. [30] (c)band-edge emission: an electron is excited by an electromagnetic wave, $h\nu$, from its ground state to an excited state. (d) photoluminescence with non-radiative transition at the beginning (e) non radiative recombination. (e) Auger recombination consists in a non-radiative energy transfer between two electrons in conduction band. This process is responsible for a fast decay of multiple excitons generated by impact ionization.

1.4.1 Photoluminescence: radiative relaxation process

The Photoluminescence (see Figure 1.9) is one of the most common phenomena in intrinsic semiconductor and insulator, where an electron in a phosphor is excited by absorption of an electromagnetic wave, $h\nu$, from its ground state to an excited state. Through a fast vibrational (nonradiative) process, the excited electron relaxes to its lowest energy excited vibrational state by losing energy in the form of the emission of light. The energy of the latter wavelength is given by the sum of:

$$E_{h\nu} = E_G + E_e + E_h + E_{exct} \quad , \qquad (1.15)$$

Where E_e *and* E_h are the electron and hole confinement energies and E_{exct} is the exciton bond energy.

There is a variety of aspects related to the emissions and the size and composition of QDs. The energy of the photon emitted shifts as function of size; additionally smaller QDs, for example, have larger bandgap, thus, they require more energy to excite their electrons and give, in turn, higher energy photons; similarly, larger QDs have shallow bandgaps and emit photons in red wavelengths. Therefore, the color emitted by a QDs can be determined by their size and composition. As a result of this, QDs can be precisely tuned during the synthesis to emit any color of light from the same material simply by changing the dot size.[29,31,32]

Luminescence can occur following various paths: (i) "*band edge emission"* (Figure 1.9(a)) when the electron transition involves the minimum of the conduction band to the maximum of the valence band; (ii) the relaxation may involve loses energy in the form of phonons, as shown in Figure 1.9(b); (iii) impurities can act as localized levels in between the energy gap and in this case, the electron relaxed through multiple steps, by means of a non-radiative transition from the conduction band to the impurity level, followed by a radiative transition to the valence band (see Figure 1.9(c)).

Additionally, depending on the relaxation lifetimes, it can be called fluorescence (10^{-9}-10^{-13} s) or phosphorescence (>10^{-5}). In NCs or bulk solids, the emitted photon is red shifted relative to the excitation photon energy/wavelength (i.e. Stokes shift) because of the presence of vibrational levels in the excited state as well as in the ground state.

The full width half maximum of a band edge emission peak and the optical absorption spectrum from QDs will be widely studied along this thesis since they reflect the band structure and the local environment of an optically active species. The first scientific record relative to the particle size and their optical properties relations dates back to 1926 when Jaeckel explained the red-shift of the absorption onset in glasses containing CdS particles[33]. At the present, the Absorption and Photoluminescence studies and the radiative relaxation processes of charge carrier and energy transfer process, play a prominent role in the understanding the optical properties of QDs. The presence of defects or surface trap states able to quench the radiative recombination is a crucial aspect to be considered when they are used for their radiative recombination (lasers, LED, etc.) or to extract the charge carriers as in solar cells.

1.4.2 Non radiative relaxation process

As reported above, the absorption of energy by a luminescent material may not result in emission of light since deep level traps may induce a non-radiative short time recombination (tens of pico-seconds[34]) by means of phonons. Nonradiative relaxation may be categorized as internal conversion, external conversion or Auger recombination [7,35–37]. The first kind of

conversion takes place after the QD absorbs a photon, with energy hν: the difference between hν and energy gap is converted into heat by electron-phonon scattering process and results in the Stoke shift. Also strain in a lattice can create a local potential well that can trap electrons and hole resulting in a non-radiative transition.

Surface states recombination dominates the external conversion. These defects are dominant channels for non-radiative decay since 15-30% of atoms lays at the surface of the QDs and may represent defects with their unsaturated dangling bonds. Charge carriers accumulates at the surface states and create an electric field that seep in opposite directions the electron and hole generated in this region preventing the radiative recombination[38–40]. This is known as exciton *dead-layer* effect: in QDs, whose size is bigger than Bohr radius, the electron and hole motion around their center of mass precludes the center of mass to reach the QD surface, forming a dead layer near the QD surface[41]. This concept was introduced by Pekar *et al.*[42] in 1958 stating that the exciton is totally reflected from an effective barrier located inside the QD at the distance d from the QD surface. The use and organic ligand or inorganic shell as capping agent on these defects leads to an improvement in luminescence efficiency[3.2,37]

Another form of non-radiative process is the Auger recombination mechanism in which the excess energy is transferred to another electron, called the Auger electron (see Figure 1.9), which then loses its extra energy by generating phonons. This mechanism is predominant in semiconductor NCs with high doping concentrations, and its more efficient in nano scale regime with respect to the analogous bulk material because conservation of momentum is broken and a strong spatial confinement of the carriers enhances multiple carrier Coulomb interactions [44,45],

It is now evident that non-radiative charge recombination negatively affects the performance of NC devices like LED[46], lasers[47], or solar cells under concentrated illumination[48] reducing their luminescence efficiency or their conversion energy. Because of the spatial and dielectric confinement of the QD, the Coulomb interaction energy between carriers increases and then some recombination mechanism[46,47,49], like the Auger scattering, are more prone to happen in NCs than in their bulk counterpart. Therefore, the most obvious way to reduce Auger recombination rates is to increase the size of the NCs [50–53]. Anyway, this is not a good strategy if we want to exploit the quantum confinement effects to tune the electronic properties of NCs. Recently, new approaches have been developed to suppress these unwanted processes like nano hetero structures [54,55] with designed charge carrier confinement potentials. The most commonly studied is CdSe/CdS [56]core/shell nanostructure in various shapes and size. Later it was confirmed that alloying hetero interface[57,58] creates a smooth confinement potential for charge

carriers. Additionally also the size and uniformity of assembly of hetero-NC with smooth confinement potentials is crucial to control the non-radiative recombination mechanism[51,59] since Auger recombination rate in NCs are strongly dependent on their dimensions [51].

REFERENCES

1. Miszta, K. *et al.* Selective Cation Exchange in the Core Region of Cu2-xSe/Cu2-xS Core/Shell Nanocrystals. *J. Am. Chem. Soc.* **137**, 12195–12198 (2015).

2. Hornyak, G. L., Moore, J. J., Tibbals, H. F. & Dutta, J. *Fundamentals of Nanotechnology*. *Fundamentals of Nanotechnology* (2018). doi:10.1201/9781315222561.

3. Cozzoli, P. D., Pellegrino, T. & Manna, L. Synthesis, properties and perspectives of hybrid nanocrystal structures. *Chemical Society Reviews* vol. 35 1195–1208 (2006).

4. Kwon, S. G. & Hyeon, T. Colloidal Chemical Synthesis and Formation Kinetics of Uniformly Sized Nanocrystals of Metals, Oxides, and Chalcogenides. *Acc. Chem. Res.* **41**, 1696–1709 (2008).

5. Donegá, C. D. M. Synthesis and properties of colloidal heteronanocrystals. *Chemical Society Reviews* vol. 40 1512–1546 (2011).

6. Walter, P. *et al.* Early use of PbS nanotechnology for an ancient hair dyeing formula. *Nano Lett.* **6**, 2215–2219 (2006).

7. Konstantatos, G. & Sargent, E. H. *Colloidal Quantum Dot Optoelectronics and Phtovotaics*.

8. Kulkarni, G., John Thomas, P. & Rao, C. Nanocrystals. in *Dekker Encyclopedia of Nanoscience and Nanotechnology, Second Edition - Six Volume Set (Print Version)* 2676–2696 (2008). doi:10.1201/noe0849396397.ch232.

9. Loos, M. R. *Carbon Nanotube Reinforced Composites: CNR Polymer Science and Technology*. *Carbon Nanotube Reinforced Composites: CNR Polymer Science and Technology* (2014). doi:10.1016/C2012-0-06123-6.

10. Atwater, H. A. The promise of Plasmonics. *Scientific American* vol. 296 53–56 (2007).

11. Liu, X., Atwater, M., Wang, J. & Huo, Q. Extinction coefficient of gold nanoparticles with different sizes and different capping ligands. *Colloids Surfaces B Biointerfaces* **58**, 3–7 (2007).

12. Ashby, M. F., Ferreira, P. J. & Schodek, D. L. An Evolutionary Perspective. in *Nanomaterials, Nanotechnologies and Design* 17–39 (2009). doi:10.1016/b978-0-7506-8149-0.00004-0.

13. Thompson, D. T. Michael Faraday's recognition of Ruby Gold: The birth of modern nanotechnology. *Gold Bull.* **40**, 267–269 (2008).

14. Mie, G. *Contributions to the optics of turbid media, particularly of colloidal metal solutions*. *Ann. Phys.* vol. 25 377–445 (1908).

15. Dreaden, E. C., Alkilany, A. M., Huang, X., Murphy, C. J. & El-Sayed, M. A. The golden age: Gold nanoparticles for biomedicine. *Chemical Society Reviews* vol. 41 2740–2779 (2012).

16. Gans, R. Form of ultramicroscopic particles of silver. *Ann. Phys.* **47**, 270–284 (1915).

17. Hollingsworth, J. A. *Semiconductor Nanocrystal Quantum Dots*. *Encyclopedia of Inorganic and Bioinorganic Chemistry* (2011). doi:10.1002/9781119951438.eibc0261.

18. Rao, C. N. R., Thomas, P. J. & Kulkarni, G. U. *Nanocrystals: Synthesis, properties and applications*. *Nanocrystals: Synthesis, Properties and Applications* (2007). doi:10.1007/978-3-540-68752-8.

19. Berry, C. R. Effects of crystal surface on the optical absorption edge of AgBr. *Phys. Rev.* (1967) doi:10.1103/PhysRev.153.989.

20. Berry, C. R. Structure and optical absorption of AgI microcrystals. *Phys. Rev.* (1967) doi:10.1103/PhysRev.161.848.

21. Efros, A. L. & Efros, A. L. Interband Light Absorption in Semiconductor Spheres. *Sov. Phys. Semicond.* **16**, 772–775 (1982).

22. Brus, L. E. Quantum Size Effects in the Electronic Properties of Small Semiconductor Crystallites. in 431–435 (1984). doi:10.1007/978-94-009-5237-9_33.

23. Rossetti, R., Nakahara, S. & Brus, L. E. Quantum size effects in the redox potentials, resonance Raman spectra, and electronic spectra of CdS crystallites in aqueous solution. *J. Chem. Phys.* **79**, 1086–1088 (1983).

24. Group, F. *Nanofabrication Handbook*. (2012). doi:10.1117/1.JNP.7.079897.

25. Brechignac, Houdy, L. *Nanomaterials and Nanochemistry*.

26. Prezhdo, O. V. Photoinduced dynamics in semiconductor quantum Dots: Insights from time-domain ab initio studies. *Acc. Chem. Res.* (2009) doi:10.1021/ar900157s.

27. Parak, W. J., Manna, L. & Nann, T. Fundamentals Principles of QD. **1**, 73–96 (2008).

28. Efros, A. L. Optical properties of semiconductor nanocrystals with degenerate valence band. *Superlattices Microstruct.* (1992) doi:10.1016/0749-6036(92)90244-Y.

29. Maschinen, B., Investition, A., Beschaffungen, G., Ersatzbeschaffungen, B. & Mittelherkunft, S. *Colloidal Foundation for Nanoscale*.

30. Peter Capper, Dafa Kasap, A. W. *Luminescent Materials and applications*.

31. Reiss, P., Carrière, M., Lincheneau, C., Vaure, L. & Tamang, S. Synthesis of Semiconductor Nanocrystals, Focusing on Nontoxic and Earth-Abundant Materials. *Chem. Rev.* **116**, 10731–10819 (2016).

32. Guyot-Sionnest, P. & Hines, M. A. Intraband transitions in semiconductor nanocrystals. *Appl. Phys. Lett.* (1998) doi:10.1063/1.120846.

33. Biadala, L. *et al.* Band-Edge Exciton Fine Structure and Recombination Dynamics in InP/ZnS Colloidal Nanocrystals. *ACS Nano* **10**, 3356–3364 (2016).

34. *Nonequilibrium Superconductivity, Phonons, and Kapitza Boundaries*. *Nonequilibrium Superconductivity, Phonons, and Kapitza Boundaries* (1981). doi:10.1007/978-1-4684-3935-9.

35. Guyot-Sionnest, P. Electrical transport in colloidal quantum dot films. *J. Phys. Chem. Lett.* **3**, 1169–1175 (2012).

36. Yoffe, A. D. Semiconductor quantum dots and related systems: Electronic, optical, luminescence and related properties of low dimensional systems. *Adv. Phys.* **50**, 1–208 (2001).

37. Emelie, P. HgCdTe Auger-Suppressed Infrared Detectors Under Non-Equilibrium Operation. *Thèsis* (2009).

38. Adam, S. *et al.* The effect of nanocrystal surface structure on the luminescence properties: Photoemission study of HF-etched InP nanocrystals. *J. Chem. Phys.* **123**, (2005).

39. Grandhi, G. K., Arunkumar, M. & Viswanatha, R. Understanding the Role of Surface Capping Ligands in Passivating the Quantum Dots Using Copper Dopants as Internal Sensor. *J. Phys. Chem. C* **120**, 19785–19795 (2016).

40. Wang, R. *et al.* Colloidal quantum dot ligand engineering for high performance solar cells. *Energy Environ. Sci.* **9**, 1130–1143 (2016).

41. Fonoberov, V. A. & Balandin, A. A. Radiative lifetime of excitons in ZnO nanocrystals: The dead-layer effect. *Phys. Rev. B - Condens. Matter Mater. Phys.* (2004) doi:10.1103/PhysRevB.70.195410.

42. Pekar, S. The Theory of Electromagnetic Waves in a Crystal in which Excitons Are Produced. *Sov. J. Exp. Theor. Phys.* (1958).

43. Miyata, K. *Highly Luminescent Lanthanide Complexes with Specific Coordination Structures*. (2014).

doi:10.1007/978-4-431-54944-4.

44. Kagan, C. R., Lifshitz, E., Sargent, E. H. & Talapin, D. V. Building devices from colloidal quantum dots. *Science (80-.).* **353**, (2016).

45. Chepic, D. I. *et al.* Auger ionization of semiconductor quantum drops in a glass matrix. *J. Lumin.* (1990) doi:10.1016/0022-2313(90)90007-X.

46. Bae, W. K. *et al.* Controlling the influence of Auger recombination on the performance of quantum-dot light-emitting diodes. *Nat. Commun.* (2013) doi:10.1038/ncomms3661.

47. Park, Y. S., Bae, W. K., Baker, T., Lim, J. & Klimov, V. I. Effect of Auger Recombination on Lasing in Heterostructured Quantum Dots with Engineered Core/Shell Interfaces. *Nano Lett.* (2015) doi:10.1021/acs.nanolett.5b02595.

48. Chen, D., Fang, G. & Chen, X. Silica-Coated Mn-Doped CsPb(Cl/Br)3Inorganic Perovskite Quantum Dots: Exciton-to-Mn Energy Transfer and Blue-Excitable Solid-State Lighting. *ACS Appl. Mater. Interfaces* **9**, 40477–40487 (2017).

49. Landsberg, P. T. & Beattie, A. R. Auger effect in semiconductors. *J. Phys. Chem. Solids* (1959) doi:10.1016/0022-3697(59)90276-8.

50. Klimov, V. I., Mikhailovsky, A. A., McBranch, D. W., Leatherdale, C. A. & Bawendi, M. G. Quantization of multiparticle Auger rates in semiconductor quantum dots. *Science (80-.).* (2000) doi:10.1126/science.287.5455.1011.

51. Vaxenburg, R., Rodina, A., Lifshitz, E. & Efros, A. L. Biexciton Auger Recombination in CdSe/CdS Core/Shell Semiconductor Nanocrystals. *Nano Lett.* (2016) doi:10.1021/acs.nanolett.6b00066.

52. Robel, I., Gresback, R., Kortshagen, U., Schaller, R. D. & Klimov, V. I. Universal size-dependent trend in auger recombination in direct-gap and indirect-gap semiconductor nanocrystals. *Phys. Rev. Lett.* (2009) doi:10.1103/PhysRevLett.102.177404.

53. Vaxenburg, R., Rodina, A., Shabaev, A., Lifshitz, E. & Efros, A. L. Nonradiative auger recombination in semiconductor nanocrystals. *Nano Lett.* (2015) doi:10.1021/nl504987h.

54. Qin, W., Liu, H. & Guyot-Sionnest, P. Small bright charged colloidal quantum dots. *ACS Nano* (2014) doi:10.1021/nn403893b.

55. Hollingsworth, J. A. Heterostructuring nanocrystal quantum dots toward intentional suppression of blinking and auger recombination. *Chemistry of Materials* (2013) doi:10.1021/cm304161d.

56. Rabouw, F. T. *et al.* Reduced auger recombination in single CdSe/CdS nanorods by one-dimensional electron delocalization. *Nano Lett.* (2013) doi:10.1021/nl4027567.

57. Bae, W. K. *et al.* Controlled alloying of the core-shell interface in CdSe/CdS quantum dots for suppression of auger recombination. *ACS Nano* (2013) doi:10.1021/nn4002825.

58. Nasilowski, M., Spinicelli, P., Patriarche, G. & Dubertret, B. Gradient CdSe/CdS Quantum Dots with Room Temperature Biexciton Unity Quantum Yield. *Nano Lett.* (2015) doi:10.1021/acs.nanolett.5b00838.

59. Park, Y. S. *et al.* Near-unity quantum yields of biexciton emission from CdSe/CdS nanocrystals measured using single-particle spectroscopy. *Phys. Rev. Lett.* (2011) doi:10.1103/PhysRevLett.106.187401.

Chapter 2. Colloidal Nanocrystals (NCs)

Abstract

Besides giving us new properties, creating novel nanostructures requires new understanding of the properties of their surfaces. Being small could make the surface of a nanoparticle unstable due to the high surface energy and the large surface curvature. Thus, the properties change as these particles are used. Not only could the surface structure and shape change, but the chemical nature of their surface could be altered, too. Thus, the efficiency of the use of the NCs depend on our understanding of their general properties and stability. Here we discuss the synthesis properties of individual NCs and the thermodynamic and mechanistic aspect of the cation exchange approach.

2.1 Introduction

Colloidal NCs are a specific kind of NCs that are chemically synthesized in a liquid solution containing some stabilizing organic molecules, called surfactants.[1] They are typically made of a crystalline core with the desired chemical composition and an outer layer surface shell (see Figure 2.1(a)) of tightly coordinated surfactants that provide them with solubility and, hence with colloidal stability.[2,3] Without the ligands, the particles would form bulky aggregates that flocculate or settle down in the medium.[3] Surface ligands enable the control over the stability of QDs dispersions in polar or nonpolar solvents via the steric and electrostatic mechanisms.[3,4] The oleophilic ligands comprise (see Figure2.1 (b)) a long hydrophilic hydrocarbon tail which is often around 8-18 carbons long, and a hydrophobic head like amines, carbocyclic acids, phosphines or phosphine oxides. These ligands can be replaced with smaller inorganic ligands, such as SnS_4^{4-}, or simple halide ions, like I^-.[2,5–8]All of these molecules are chemically robust and, therefore likely to be further processed after synthesis for different purposes, such as their integration with existing devices, or their incorporation into biological environments without substantial loss of the original properties.[1,4,3]

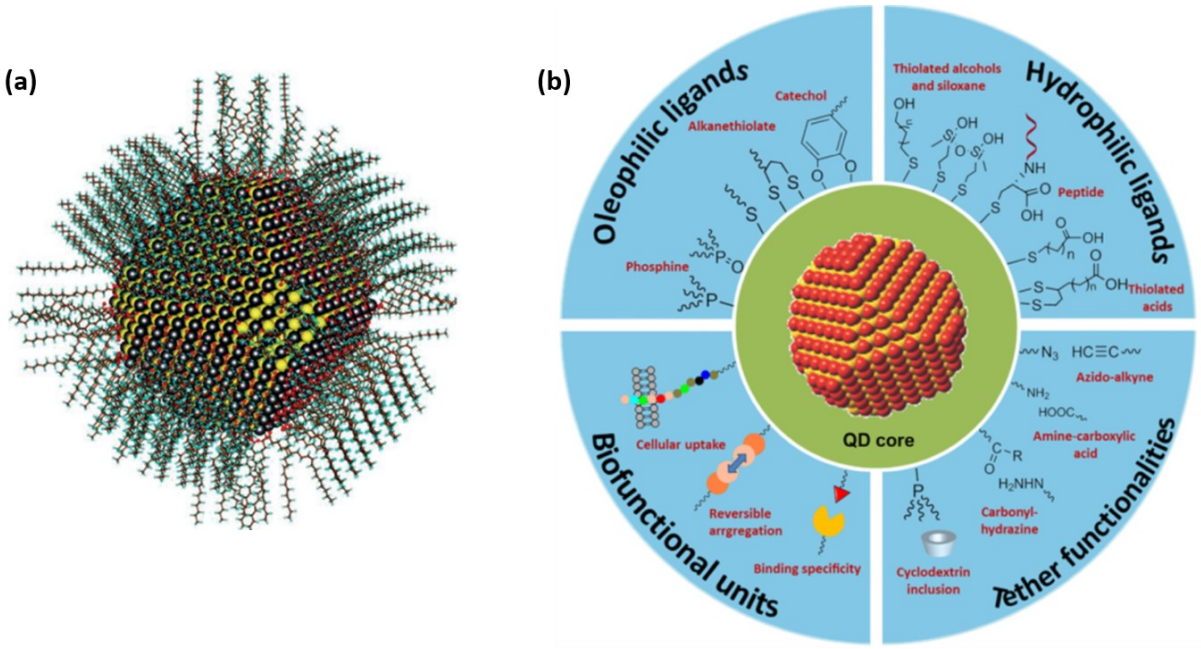

Figure 2.1. (a) computational model representation of a PbS NC covered with oleate and hydroxyl ligands. (from Zherebetskyy, D., *et al*., Ref [9] (b) capping ligands for different end applications. (from Zhou, *et al.* Ref[3])

The ligands on the NC surface are not only important for the colloidal stability and processability of NCs in apolar solvents, but also play an important role in passivating trap states. The radiative recombination, discussed in previous sections, can be quenched because atoms at the surface of a NC can act as under-coordinated atoms, and, thus, can form trap states, which lead to non-radiative recombination. These surface trap states originate from non-bonding orbitals of atoms that protrude from the NC surface, and they are also called "dangling bonds".[10] Since NCs have a very high percentage of atoms at the surface, a careful passivation of surface atoms is required.

An alternative way to passivate the dangling bonds at the NC surface is by epitaxially overgrowing the NC with a shell made of second semiconductor. The selection of the shell is done in function of the band alignments of the bulk materials. Three configurations can be distinguished: type-I, type-II and reverse type-I. In type-I the shell material is larger than that of the core, so the photoexcited excitons are confined in the core. This configuration is used to passivate the surface of the core with a resulting improved photoluminescence. In reverse type-I alignment, the bandgap of the shell material is smaller than that of the core and, depending on the shell's thickness, the holes and electrons are partially or completely confined in the shell. In these systems, the emission wavelength can be tuned controlling the shell's thickness. Finally, in type-II heterostructures, the valence band offset or the conduction band inset of the shell is located in the bandgap of the core. Upon excitation of the NC the electron-hole couple

is spatially separated in different regions of the composite structure. Therefore, this type of core shell NCs is often limited to down-conversion applications.

These so-called core@shell NCs are among the brightest emitting NCs, and they also have the advantage of being chemically shielded, this makes them less susceptible to being oxidized.[1,10]

2.2 Synthetic methods for semiconductor NCs Quantum Dots Synthesis

There is a huge set of methods for producing nano-size particles and crystals. All these approaches have the specific goal of ensuring optimal control of the chemical composition and size of nanomaterials. Obviously, as already explained, the physical properties of NCs depend on the size of the NC. A narrow size distribution is essential to establish well defined properties of the samples. The top-down approaches for the development of engineered nanomaterials include macroscopic solids fragmentation and structuring, both mechanically (e.g. ball milling) or chemically (lithography, exfoliation, etching, etc.). The bottom-up assembly starts with molecules, atoms and ions and proceeds via gas-phase, liquid-phase chemical reactions, aggregation, and crystallization.[11,12,13, 14] However, liquid-phase synthesis in aqueous or non-aqueous solvents, turned out to be particularly convenient and successful. Surfactant-assisted, colloidal synthesis in organic solvents earned the highest appreciation and will be discussed here in detail.

This kind of synthesis is usually performed in a round bottom flask that is connected to a Schlenk line.[15] Here, precursors can be purged from air and moisture by purging them under vacuum at 100°C. The final reaction often is performed under nitrogen (or argon) flow. These precautions are often necessary, as most NCs are air and moisture sensitive. The first step of the colloidal synthesis is known as “precursor formation” and involves the preparation of metal and nonmetal-ligand complexes,[16] starting from metal salts (such as metal acetates, halides or oxides) and common non-metal precursors (like tellurium) which are complexed with organic ligands (such as oleylamine (OLAM), oleic acid (OA) or trioctylphosphine (TOP) at elevated temperatures (100-300°C). The formed complexes are sometimes also referred to as “monomers”.[16] Although the examples of precursors that are mentioned above are the most common ones that are used in this process, other non-metal precursors, like dodecanthiol, do not require any complexation and can be used directly without any complexation.[16–18]

The second step is the nucleation step, in which the non-metal and metal monomers are combined and decomposed into clusters, followed by the formation of nuclei. Here, the clusters are small (often only a few monomers big), and the crystals and nuclei are defined as the

smallest size cluster needed for the growth of NCs, as will be discussed later. The nucleation step is usually performed by using the "hot-injection method", which was first described in 1993.[16,17] In this hot-injection method, one precursor solution (often the non-metal precursor) is injected into a hot-solution (100-300 °C) that contains the second precursor (often the metal precursor). This method allows for the best size and shape control of the NCs. Moreover, it is the best method to obtain (nearly) monodisperse NCs, but it often lacks in terms of reproducibility and scalability. Also, this method allows for the separation of metal (cation) and non-metal (anion) precursors, allowing for the synthesis of highly complex alloyed or hereto NCs.[16,17] Alternatively, a quick and simple heating-up synthesis can be employed. In this method, all precursors, ligands and solvents are mixed in one solution and quickly heated up, followed by cooling down. This technique is often simply called the "heating-up method", and results in having less control over the size of the NCs compared to the hot-injection method. Furthermore, the heating-up synthesis is limited with regard to composition tunability, as highly complex multinary systems often cause the nucleation of separate phases, since different precursors have different reaction temperatures. On the other hand, the heating-up method is more reproducible and is easier to scale up, making it a more robust synthesis approach for industrial syntheses of NCs.

In the third step, the nuclei, which are often only a few nm big, become vital meaning that they cannot dissolve anymore, and they start to form small NCs. These nuclei are the building blocks for the growth of larger NCs. The formation of vital nuclei is one of the most important steps in the synthesis of NCs, and it strongly influences the size and monodispersity of the final NCs. The way in which the nuclei grow into larger NCs, reflexes in how size and shape of the final NCs can be obtained.

To stop the NCs from growing, the dispersion is cooled down to room temperature, sometimes quickly with an ice bath or by the addition of cold solvents, or sometimes slowly by simply removing the heating source. After cooling, the NCs still need to be removed from the growth solution, which is the final step of the synthesis. This has to be done as residual precursors or ligands can cause the NCs to keep growing or reshape over time. This process, called "Oswald ripening",[17] results in an increase in the size-distribution of the NCs. Solvents with a high boiling point such as these are detrimental to the conductivity of NC films and therefore need to be removed. To remove the NCs from their growth solution, the NC dispersions are added with an "anti-solvent". This anti-solvent (often isopropanol,methanol or methylacetate) results in the precipitation of the NCs, which allows them to be separated by centrifugation (300-12000 rpm, 5-30 min). The precipitated NCs, which are still covered with an apolar ligand

shell, are redispersed in an apolar solvent with a low boiling point. The use of solvents with a low boiling point (like toluene, hexane, or chloroform) allows for a quick evaporation of the solvent. This washing steps is often necessary for NC-based devices, as the ligand drastically lower the conductivity of NC films.

2.2.1 Growth of colloidal NCs

A big challenge in the synthesis of colloidal NC is the control over the size distribution. To understand how to tune the size of growing NCs we have to have clear the mechanism of the formation of colloidal NCs from monomers in solution. There are three stages: (i) induction (pre-nucleation),(ii) nucleation, and (iii)growth.[16] The nucleation phase (phase II) is the period in which the nuclei form so-called critical nuclei and start to became large enough to not dissolve. Finally, the growth stage (phase III) marks the period in which the critical nuclei grow into larger NCs. This overall growth scheme is shown in Figure (a). The concentration of monomers (or the "saturation level") plays a key role into how they are being consumed for the formation of nuclei and NCs. The monomer concentration can be divided into three important categories.[16] The "critical saturation concentration"(C_{min}) is the minimum concentration that is needed for the formation of nuclei, and is the concentration when the solubility of the monomers reaches its limit. When a "supersaturation concentration" (C_{max}) is obtained, the solution becomes thermodynamically unstable, and results in the rapid formation of nuclei. This occurs when the concentration of monomers becomes higher than their solubility limit. Finally, the lowest concentration needed for the consumption of monomers is called the "minimal saturation" (C_m). At this saturation level, the monomers' concentration is too low for the formation of nuclei, as it is thermodynamically too costly, but does allow for the growth of existing nuclei or NCs. Thus, for a narrow size distribution of the final NCs, it is important that the three phases are well separated. This is possibly by quickly reaching a supersaturated solution, which allows for a rapid burst of nuclei, followed by a rapid drop in the monomer concentration, blocking the formation of new nuclei, but promoting the growth of nuclei that had already formed. To reach a fast supersaturation, one can quickly heat up a concentrated precursor solution (as with the heating-up synthesis described in the previous section) or suddenly increases the precursor concentration (by injecting one precursor into the other). Similarly, one can quickly lower the temperature, resulting in a rapid decrease in the solubility of the monomers. Both the rapid increases of the precursor concentration and the drop in temperature can be obtained by the hot-injection synthesis. The injection of a cold concentrated precursor solution at a high temperature results in an almost instant supersaturated

solution, which is further promoted by the sudden drop in the reaction temperature. In order to obtain a rapid supersaturation, the concentrated precursor solution can be quickly heated (as with the heating synthesis) or the precursor concentration can be suddenly increased (by injecting one precursor into the other). Similarly, the temperature can be rapidly lowered, resulting in a rapid decrease in the solubility of the monomers. Both the rapid increase of the precursor concentration and the decrease in temperature can be accomplished by hot-injection synthesis. The injection of a cold concentrated precursor solution at a high temperature results in an almost instant supersaturated solution, which is further promoted by the sudden drop in the reaction temperature.[16] Thus, using the hot-injection method, the monomer consumption rate exceeds the monomer production rate, resulting in a rapid drop in the monomers' saturation level, below the C_{min} but above the C_m. This promotes growth, resulting in monodisperse NCs. To explain the formation of colloidal NCs from solution, La Mer adopted the "classic nucleation theory" which explains how the thermodynamics of the system tend to minimize the Gibbs‡ free energy during the formation of "bulk" and interfaces, which lowers the overall entropy of the system.[16] In the case of a perfect spherical particle, the overall Gibbs free energy, is described by Eq.2.1 [16]:

$$\Delta G = \Delta G_v + \Delta G_s = \frac{4\pi}{3} r^3 \rho \Delta\mu + 4\pi r^2 \gamma \qquad (2.1)$$

Where r is the radius of the particle, ρ is the density of the particle, $\Delta\mu$ is the chemical potential difference between the monomers and the nuclei, and γ is the surface area energy. The Gibbs free energy in Eq.(2.1) consists of two terms a term for the formation of bulk, the Gibbs free bulk energy (ΔG_v); and a term for the loss of energy due to the formation of a surface (Gibbs free surface energy, ΔG_s). As shown in Figure (b) Gibbs free energy is positive with very small particle sizes, as it is mainly dominated by the small nuclei's very large surface areas. When the size of a NC crosses the so called "critical size", which is indicated as r^* in Figure (b), the Gibbs bulk free energy gets big enough to overcome the Gibbs free surface energy and allow the systems to lower its overalls Gibbs free energy leading to the growth of the crystal itself. The concentration of monomers plays a key role in the synthesis: the higher is the concentration of monomer the lower is the critical size of the NCs. [2]The critical radius explains the "Oswald ripening" phenomenon happening after prolonged reaction times.[2] When NCs are left in their reaction solutions for a long time, resulting in a very low monomer saturation, or are kept at a low temperature, the r_c will become very large. This large critical radius will promote the dissolution of the smallest NCs, which encourages the growth of larger ones, resulting in an

increase in the size distribution. Thus, it is important to separate the NCs from their growth solutions before the saturation drops too low and the NCs start to grow.

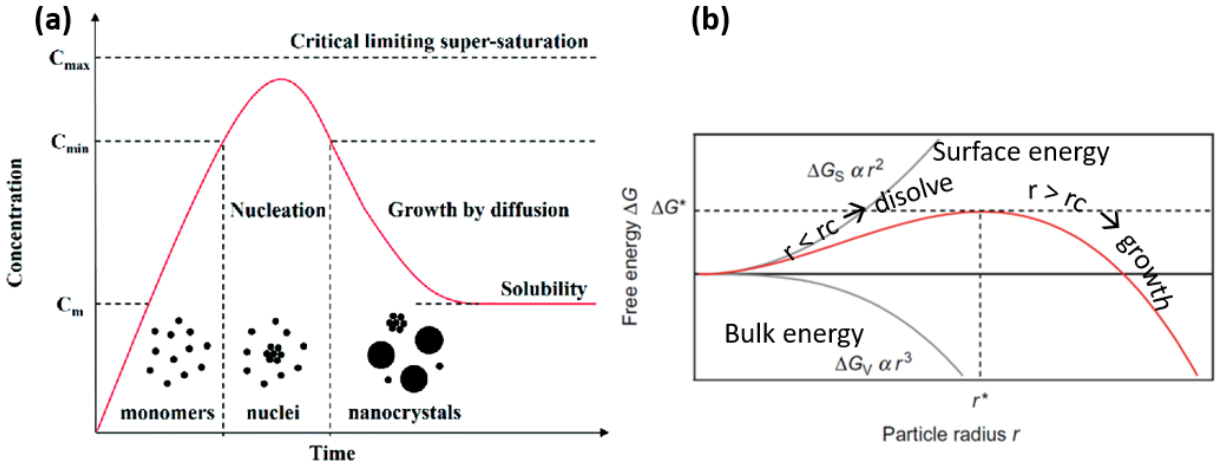

Figure 2.2. (a)Schematic illustration for general formation of colloidal nanocrystals from dissolved monomers. In zone I the monomers concentration is below the nucleation threshold and no NCs are formed. In zone II, the nucleation takes place until monomers' concentration drops below the critical value of nucleation. The growth of NCs usually starts within this nucleation phase. In zone III, the nucleation is completely substituted by the growth of NCs. This Figure is reproduced from Ref.[17] (b) Gibbs free energy for the formation of NCs from monomers, indicating both the Gibbs surface free energy and the Gibbs bulk free energy. From Ref.[16]

The rate of the Oswald ripping strongly depends on the rate of precursor consumption as well as the r_c, which both strongly depend on the reactivation of the precursors, as well as on the activation energy that is needed to form the NCs.[16] A common wise method to avoid the Oswald ripening problem is to use multiple injections of precursors. During the growth of the NCs the concentration lowers, and the addition of new precursors can change suddenly the critical size promoting the growth of smaller NCs. Another interesting way to get kinetic control over the production of NC is to separate the nucleation event from the growth step. This can be achieved when the nucleation occurs on a short time scale and the growth can proceed over the rest of the synthetic time. For this purpose, precursors are rapidly injected into the reaction flask at high temperature in order to induce a so called "nucleation burst". A fast nucleation burst can rapidly consume the precursors shifting the concentration of monomers below the nucleation threshold. The remaining monomers in solution will only add to the existing nuclei. As mentioned in the above paragraph, the hot-injection method has several limitations, such as the scalability of the reaction. Moreover, it needs highly reactive precursors which are available for many materials and, finally, extremely vigorous reactions at high temperature can become very dangerous.

2.2.2 Cation exchange

A typical problem associated with the colloidal synthesis NCs is the difficulty in producing particles with the same size but different compositions. Even though the size can often be tightly controlled for an individual colloidal system, it is challenging to fine-tune the size so that a very close match will be achieved for colloidal NCs of different compositions.[19–21] Cation exchange reactions are very attractive for this purpose because the morphology of the starting materials can be preserved during the exchange process.[21] It is generally assumed that during such an exchange, the anionic framework of the crystal is conserved, while the cations, due to their relatively smaller size and higher mobility, undergo replacement.[22] It has been also shown that cation exchange reactions are possible in nanocrystalline samples because the effective reaction barrier is much lower than in larger systems thanks to an enhanced surface access and lower activation barriers to diffusing ions[21,22] The cation exchange reactions are often carried out in solutions containing the respective salt precursors. In these reactions, a large difference in solubility provides the driving force for the ion replacement. [22]Generally, the starting material present in a solution containing an appropriate precursor will spontaneously undergo cation exchange to yield the product with a lower solubility. On the other hand, when the solubility of the desired product is higher than the solubility of the precursor material, new strategies are needed. An extra molecule/ligand can be added to the solution to modify the equilibrium. The new added ligand can bind to NCs' cations forming intermediate complexes to facilitate the cation exchange by allowing the association of the cations in solution with the anion sublattice.[20–23] The interesting fact is that in cation exchange reactions the shape is completely preserved while the composition is completely modified leading to totally different semiconductor material. This observation suggests that cation exchange is a valid alternative route toward the synthesis of nanocrystals with complex compositions that can be very difficult to synthesize by colloidal routes.

While a cation exchange reaction is remarkably simple to execute, the outcome of the reaction and the structure of the product obtained are dictated by delicate thermodynamic and kinetic factors.[21] Thus, to design the exchange reaction, an understanding of the thermodynamics and kinetics of the process is necessary.

2.2.2.1Thermodynamics in cation exchange

The synthetic efficiency of a cation exchange reaction is determined by its thermodynamic driving force and activation barriers.[24] Consider, for example, an arbitrary ion exchange

reaction between an ionic AX (where X is an anion) NC exposed to a solution of B^+ cations to give a BX structure can be written as:[21,22]

$$AX(s) + B^+(sol) \leftrightarrow BX(s) + A^+(sol) \quad (2.2)$$

Where A and B represent divalent metal ions. This exchange reaction can be divided into four different steps,[22] each requiring the knowledge of the energies involved:

$$AX \rightarrow A + X \quad \textit{dissociation} \quad (2.3)$$

$$B^+ \rightarrow B \quad \textit{desolvation} \quad (2.4)$$

$$B + X \rightarrow BX \quad \textit{association} \quad (2.5)$$

$$A^+ \rightarrow A \quad \textit{solvation} \quad (2.6)$$

The association and dissociation processes can be defined in terms of lattice and surface energy of the AX and BX crystals. The lattice enthalpy to isolate the ions of a crystal at absolute zero temperature is defined by:

$$\Delta H_{latt} = \frac{NAz^+z^-e^2}{r^+ + r^-}(1 - \frac{1}{n}) \quad (2.7)$$

Where N is the Avogadro's number, A is the Madelung constant, $z^+$and $z^-$are ionic charges of the cation and the anion, $r^+$and $r^-$are ionic radii of the cation and the anion, and *n* is the Born exponent (that take into account the ionic repulsion). The Madelung constant is intimately related with the spatial position of the ions and, thus, dependent on the crystal structure of the material. It follows that, different allotrope of a given material can have significantly different lattice energy.[22] Unfortunately, it is not always easy to find the tabulated ΔH_{latt} values of many of metal chalcogenides NCs, especially when they have allotropes. This is particularly difficult when considering that, the CE reactions can lead to the formation of metastable crystal structures that cannot be predicted a priori. In these cases, if the structure of the materials is known, it is possible to make some qualitative conclusion about lattice energies following Eq. 2.7. [22] In particular, since ΔH_{latt} strongly depends on the distance between cations and anions (r), then for a given a certain cation M^+ and by increasing the size of the A^- anion (while keeping the ionic charges and the crystal structure fixed) a decrease in ΔH_{latt} is expected.

Therefore, in general, the ΔH_{latt} of metal chalcogenides decreases in absolute value as the ionic radius of the chalcogen increases: ΔH_{latt} (M_xS_y)> ΔH_{latt} (M_xSe_y)> ΔH_{latt} (M_xTe_y) [22]

acid	η	base	η
Cu^+	6.28	$C_6H_5NH_2$	4.4
Pd^{2+}	6.75	C_6H_5SH	4.6
Ag^+	6.96	C_6H_5OH	4.8
Fe^{2+}	7.24	C_5H_5N	5
Hg^{2+}	7.7	CH_3COCH_3	5.6
Sn^{2+}	7.94	CH_3CHO	5.7
Pt^{2+}	8	DMF	5.8
Co^{2+}	8.22	$(CH_3)_3P$	5.9
Cu^{2+}	8.27	PH_3	6
Au^{3+}	8.4	$(CH_3)_2S$	6
Pb^{2+}	8.46	CH_2O	6.2
Co^{3+}	8.9	$HCONH_2$	6.2
Mn^{2+}	9.02	$(CH_3)_3N$	6.3
Ge^{2+}	9.15	HCO_2CH_3	6.4
Cd^{2+}	10.29	CH_3CN	7.5
Zn^{2+}	10.88	CH_3Cl	7.5
Fe^{3+}	12.08	$(CH_3)_2O$	8
In^{3+}	13	NH_3	8.2
Ga^{3+}	17	CH_3F	9.4
Al^{3+}	45.77	H_2O	9.5

Figure 2.3. Experimental absolute hardness, η, of a typical cations and ligands or bases. From ref [72]

An alternative way to estimate qualitatively the stability of the compounds involved in a cation exchange reaction is to consider the bond dissociation energy (BDE),[22] which is defined as the standard enthalpy for the homolysis of the bond, as following:

$$A - X \rightarrow A\cdot + \cdot X \qquad (2.8)$$

The tabulated energy is calculated for diatomic molecules and are independent from the crystal structure, thus they must be taken with care.

Considering the surface energy, it is barely predictable since it depends on different variables, primarily on the kind of surfactants stabilizing the particles and, on the chemistry and structure of the different facets of the NCs.

The control of the energies involved in the solvation and desolvation energies is essential to trigger the CE. A precise knowledge of the affinity of the exchanging cations is necessary to enhance the extraction of the outgoing cations and the introduction of the guest ones. For this, suitable solvents and ligands are needed. A qualitative choice can be done accordingly to the "Hard and Soft Acid and Bases" (HSAB) theory, [22,25,26] which assumes hard acids bind preferentially with hard basis forming ionic complex, while soft acids prefer to from covalent complexes binding to soft bases (see Figure 2.3). The absolute hardness, η, can be imaged as

the resistance towards deformation of the electronic cloud of a certain atom. Soft bases are characterized by a donor atom of high polarizability and low electronegativity that is easily to oxidize; hard bases have a donor atom of low polarizability and high electronegativity that is hard to oxidize. On the other hand, in soft acids the acceptor atom is of low positive charge and large size, while in hard acids the acceptor atom is of high positive charge and small size.
In this work, we applied this knowledge in the case of CdTe NCs , InP and $CuInS_2$ NCs.
In the case of a CE in polar solvents, such as methanol, ethanol or water, one can also evaluate the solubility product constants (K_{SP}) [22] defined as:

$$K_{SP} = [A^+][X^-] \tag{2.9}$$

Which is the equilibrium constant for the reaction:

$$AX\ (solid)\ \leftrightarrow\ A^+\ (liq) + X^-\ (liq) \tag{2.10}$$

In alternative, considering the variation of the formation energy (ΔG_f^0) of the species involved:

$$G_{reaction} = \Delta G^0_{f\ A+,liq} + \Delta G^0_{f\ X-,liq} - \Delta G^0_{f\ AX,solid} \tag{2.11}$$

the solubility product constant can be calculated with the equation:

$$\ln K_{SP} = -\left(\frac{\Delta G^0}{RT}\right) \tag{2.12}$$

For a CE reaction, the formation of the new crystal phase BX is favored if its Ksp is lower with respect to the Ksp of the starting AX compound.
Concerning the mechanism and the kinetics of CE reactions, one aspect to be considered is the mechanism of the diffusion of the guest cations inside the host crystal lattice, which can occur both via interstitial or vacancies sites.[22] Depending on their diffusivity, guest cations can either probe the whole host lattice to reach the energetically favored sites for the nucleation of the new phase or only access the entry points on the surface of the NC. Concerning partial CE, the outcome of such reaction depends on the miscibility of the new phase with the starting one: if the two phases are miscible, the result is an alloy or, with a very low amount of substituted cations, a doped NC. On the contrary, in case of immiscible phases, the outcome is a heterostructure composed of two or more distinguishable domains, which can be arranged with various architecture, such as core@shell (or core@graded-shell) heterostructures even with elaborated architectures (i.e., quantum wells, multiple-cores@shell).

REFERENCES

1. Bera, D., Qian, L., Tseng, T. K. & Holloway, P. H. Quantum dots and their multimodal applications: A review. *Materials (Basel).* **3**, 2260–2345 (2010).

2. Chang, J. & Waclawik, E. R. Colloidal semiconductor nanocrystals: Controlled synthesis and surface chemistry in organic media. *RSC Adv.* **4**, 23505–23527 (2014).

3. Zhou, J., Liu, Y., Tang, J. & Tang, W. Surface ligands engineering of semiconductor quantum dots for chemosensory and biological applications. *Mater. Today* **20**, 360–376 (2017).

4. Burda, C., Chen, X., Narayanan, R. & El-Sayed, M. A. *Chemistry and properties of nanocrystals of different shapes*. *Chemical Reviews* vol. 105 (2005).

5. Zhang, H. *et al.* Surfactant ligand removal and rational fabrication of inorganically connected quantum dots. *Nano Lett.* **11**, 5356–5361 (2011).

6. Anderson, N. C., Hendricks, M. P., Choi, J. J. & Owen, J. S. Ligand exchange and the stoichiometry of metal chalcogenide nanocrystals: Spectroscopic observation of facile metal-carboxylate displacement and binding. *J. Am. Chem. Soc.* **135**, 18536–18548 (2013).

7. Owen, J. S., Park, J., Trudeau, P. E. & Alivisatos, A. P. Reaction chemistry and ligand exchange at cadmium-selenide nanocrystal surfaces. *J. Am. Chem. Soc.* **130**, 12279–12281 (2008).

8. Hassinen, A. *et al.* Short-chain alcohols strip X-type ligands and quench the luminescence of PbSe and CdSe quantum Dots, acetonitrile does not. *J. Am. Chem. Soc.* **134**, 20705–20712 (2012).

9. Zherebetskyy, D. *et al.* Hydroxylation of the surface of PbS nanocrystals passivated with oleic acid. *Science (80-.).* (2014) doi:10.1126/science.1252727.

10. Reiss, P., Protière, M. & Li, L. Core/shell semiconductor nanocrystals. *Small* **5**, 154–168 (2009).

11. Yoffe, A. D. Semiconductor quantum dots and related systems: Electronic, optical, luminescence and related properties of low dimensional systems. *Adv. Phys.* **50**, 1–208 (2001).

12. Yumoto, J. *et al.* Optical nonlinearity of CdSe microcrystallites in a sputtered SiO 2 film. *Appl. Phys. Lett.* **57**, 2393–2395 (1990).

13. Borsella, E. *et al.* MoS2 nanoparticles produced by laser induced synthesis from gaseous precursors. *J. Mater. Sci. Lett.* **20**, 187–191 (2001).

14. Wang, X., Zhuang, J., Peng, Q. & Li, Y. A general strategy for nanocrystal synthesis. *Nature* **437**, 121–124 (2005).

15. Group, F. *Nanofabrication Handbook*. (2012). doi:10.1117/1.JNP.7.079897.

16. Maschinen, B., Investition, A., Beschaffungen, G., Ersatzbeschaffungen, B. & Mittelherkunft, S. *Colloidal Foundation for Nanoscale*.

17. Hollingsworth, J. A. *Semiconductor Nanocrystal Quantum Dots*. *Encyclopedia of Inorganic and Bioinorganic Chemistry* (2011). doi:10.1002/9781119951438.eibc0261.

18. Reiss, P., Carrière, M., Lincheneau, C., Vaure, L. & Tamang, S. Synthesis of Semiconductor Nanocrystals, Focusing on Nontoxic and Earth-Abundant Materials. *Chem. Rev.* **116**, 10731–10819 (2016).

19. Justo, Y. *et al.* Less is more. Cation exchange and the chemistry of the nanocrystal surface. *ACS Nano* **8**, 7948–7957 (2014).

20. Son, D. H. Cation Exchange Reactions in Ionic Nanocrystals. *Science (80-.).* **306**, 1009–1012 (2004).

21. Rivest, J. B. & Jain, P. K. Cation exchange on the nanoscale: An emerging technique for new material synthesis, device fabrication, and chemical sensing. *Chemical Society Reviews* vol. 42 89–96

(2013).

22. De Trizio, L. & Manna, L. Forging colloidal nanostructures via cation exchange reactions. *Chem. Rev.* **116**, 10852–10887 (2016).

23. Beberwyck, B. J., Surendranath, Y. & Alivisatos, A. P. Cation exchange: A versatile tool for nanomaterials synthesis. *J. Phys. Chem. C* **117**, 19759–19770 (2013).

24. Wark, S. E., Hsia, C. H. & Dong, H. S. Effects of ion solvation and volume change of reaction on the equilibrium and morphology in cation-exchange reaction of nanocrystals. *J. Am. Chem. Soc.* **130**, 9550–9555 (2008).

25. Taniguchi, S., Green, M. & Lim, T. The room-temperature synthesis of anisotropic CdHgTe quantum dot alloys: A 'molecular welding' effect. *J. Am. Chem. Soc.* **133**, 3328–3331 (2011).

26. Nag, A. *et al.* Metal-free inorganic ligands for colloidal nanocrystals: S2-, HS-, Se2-, HSe-, Te2-, HTe -, TeS32-, OH-, and NH 2- as surface ligands. *J. Am. Chem. Soc.* **133**, 10612–10620 (2011).

Chapter 3. Characterization Techniques

3.1 Elemental Analysis by Inductively Couple Plasma (ICP)

The first step in determining the chemical composition of the NCs is a detailed elemental analysis and among several opportunities we used Inductively Couple Plasma Optical Emission Spectroscopy (ICP-OES) to determine the mean composition of NCs. In a volumetric flask, each sample was dissolved in aqua regia (HCl /HNO_3, 3:1 (v/v), high purity grade) and left overnight at room temperature, to completely digest the NCs. Afterward, Mill-Q grade water (18.3 MΩ cm) was added to the sample. The solution was then filtered using a Polytetrafluoroethylene (PTFE) Membrane Filter, with 0.45 μm pore size. All chemical analyses performed by ICP-OES were affected by a systematic error of about 5-10%. The sample is ionized with inductively coupled plasma and the polychromatic radiation coming from individual wavelength of each excited ions in the plasma is measured to obtain information about the sample. The intensity of these emissions is proportional to the concentration of the corresponding element[1], but before is necessary to separate the outcoming radiation into individual wavelength without the interference from emission at other wavelength and this is done by means of the monochromator, which is used to measure light at one wavelength at a time, or a polychromator, which is used to measure light at several different wavelengths at once. Then a photosensitive detector such as a photo-multiplier tube (PMT) or advanced detector technique as a charge-injection device (CID) or a charge-coupled device (CCD) can be used.[1,2] A representation of the layout of a typical ICP-OES instrument is shown in Figure 3.1

3.2 X-ray Diffraction (XRD) analysis

X-ray diffraction is a powerful tool to determine the crystal structure of the synthesized NCs.[3,4] The crystal structure is based on diffraction phenomena caused by the interaction of matter with X-rays and essentially occurs by means of two processes[5]: (i) photons of the incident beam are deflected without a loss of energy (the scattered radiation with exactly the same wavelength as the incident radiation) or with a small loss of energy (Compton radiation, with wavelength slightly greater than the wavelength of the incident radiation); (ii) the photon can be absorbed by the atoms and will increase its temperature in what is known as photoelectric effect in which an inner-shell electron of the target is removed and emitting a fluorescent radiation when it relaxes to its minimal state energy. In this study, we were not interested in wave propagation

processes, but only in diffraction patterns produced by the interaction between waves and matter.

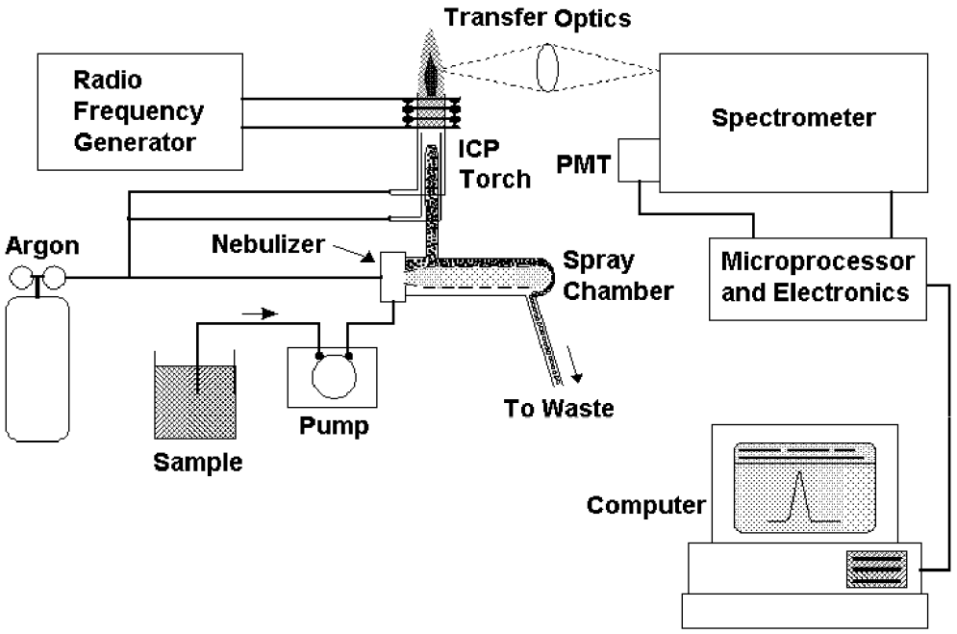

Figure 3.1. Major components and layout of a typical ICP-OES instrument. from Boss et al. 1 The sample is transported into the instrument as a stream of liquid sample. Inside the instrument, the liquid is nebulized and then transported to the plasma where it is desolvated, vaporized, atomized and ionized by the plasma. The excited atoms and ions emit their characteristic radiation which is collected by a device that sorts the radiation by wavelength. The radiation is detected and turned into electronic signals that are converted into concentration information for the analyst

The diffraction pattern is by the electromagnetic radiation interaction with crystal periodic structure whose repeating distances must be the same wavelength of the radiation.[4] Defining for a crystal structure a repeating unit cell represented by three vectors $\vec{a}, \vec{b}, \vec{c}$, and a family of lattice planes with three integers *h,k,l* (Miller indices), it is possible to define the lattice vector :

$$\overrightarrow{v_{h,k,l}} = h\,\vec{a_i} + k\,\vec{b_i} + l\,\vec{c_i} \qquad (3.1)$$

Where $\vec{a_i}, \vec{b_i}, \vec{c_i}$ are the reciprocal vectors of the unit cell.

Considering an incident X-ray beam on parallel planar lattice planes (hkl) separated by an interplanar spacing $d_{hkl,}$ two parallel incident rays form an angle θ with them. A reflected maximum intensity results from the waves that are in phase, and this is verified if the difference in path length is an integer number of the incoming wavelength, λ. The relationship describing this interaction was formulated in 1912 by W.L. Bragg in what is know as Bragg's Law (see Figure 3.1)

$$2\, d_{hkl} \sin\theta = n\lambda \qquad (3.2)$$

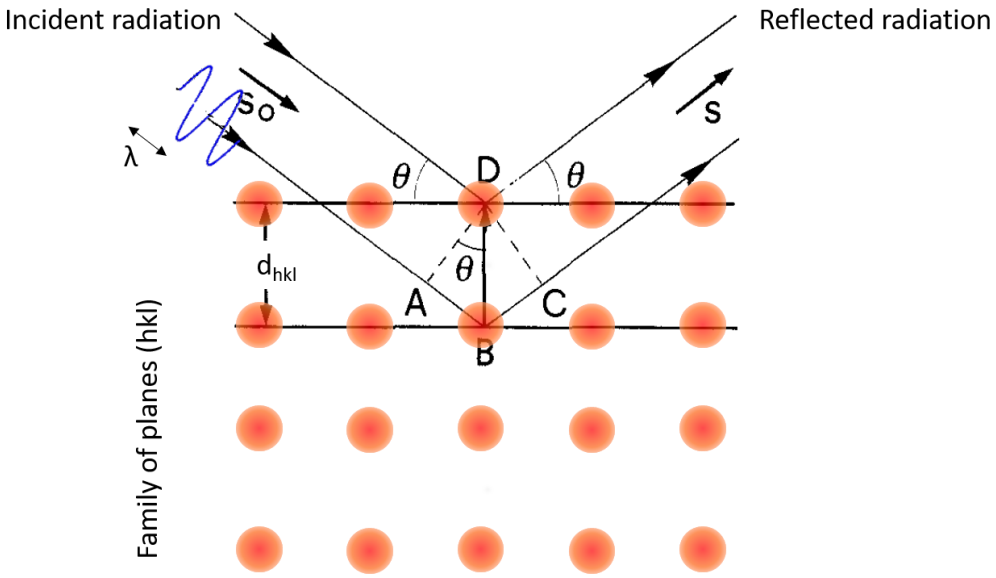

Figure 3.2. Schematic representation of Bragg's law. Reflection of X-rays from two lattice planes belonging to the family (h,k,l) with interplanar spacing d. If the path difference between the scattered waves in D and in B is equal to AB + BC =2 dhkl sin θ and it is an integer multiple of λ, then the two waves combine themselves with the maximum positive interference.

Since the intensities of the reflections depend on the kind of atom and their location in the unit cell, only planes with high electron intensity will reflect strongly and each reflection is fully defined when d-spacing, intensity and indexes h,k,l are defined. In this way it is possible to identify univocally a specific crystal structure from a diffraction pattern.

Lattice strain can shift the diffraction peak position. Thus, it is possible to calculate the d-spacing change resulting from the variation of lattice constants coming from a strain. Furthermore, the diffraction peaks can show a broadening, instead of a single shift, increasing with sinθ when an inhomogeneous strain vary from one NC to another one. Another kind of broadening effect takes place when the dimensions of the crystals shrink from bulk material to nano size regime, and in this case, it is independent from θ. Thus, it is possible to estimate the NCs size, D using the Scherrer's formula:

$$D = \frac{k\lambda}{B\cos\theta_B} \qquad (3.3)$$

Where B is the full width half maximum (FWHM) of the diffraction peak at angle θ_B, k is the Scherrer's constant.

In this study, X-ray diffraction analysis were performed on a PANalytical Empyrean X-ray diffractometer equipped with a 1.8 kW CuKα ceramic X-ray tube and PIXcel^{3D} 2x2 area detector, operating at 45 kV and 40 mA. Specimens for the XRD measurements were prepared in a glove box by dropping a concentrated NCs solution onto a quartz zero-diffraction single crystal substrate. The diffraction patterns were collected in air at room temperature using ParallelBeam (PB) geometry and symmetric reflection mode. XRD data analysis was carried out using HighScore 4.1 software from PANalytical. High temperature X-ray diffraction analysis (HTXRD) from room temperature to 350 °C, under inert atmos-phere (N2), was performed using a Rigaku Smartlab sys-tem equipped with a 9 kW Cu Kα rotating anode (oper-ating at 40 kV and 150 mA) and an Anton Paar DHS 900 domed hot stage. Samples for the measurements were prepared by dropcasting a concentrated NC solution onto a silicon wafer under N2 filled glovebox.

3.3 Transmission Electron Microscopy (TEM) analysis

The main reason for the use of the electron microscope resides in the superior resolution it allows due to the very small wavelength of the electrons that, depending on the accelerating voltage V (100-1500kV), varies in the range of 4-0.3 pm, many order of magnitude smaller than the visible light wavelength (400-700 nm). The limit of the resolution is not inherent in the instrument but often depends on the electron densities of the material analyzed and their thermal stability. Crystals with elements high atomic numbers give a higher electron scattering and so a better contrast.

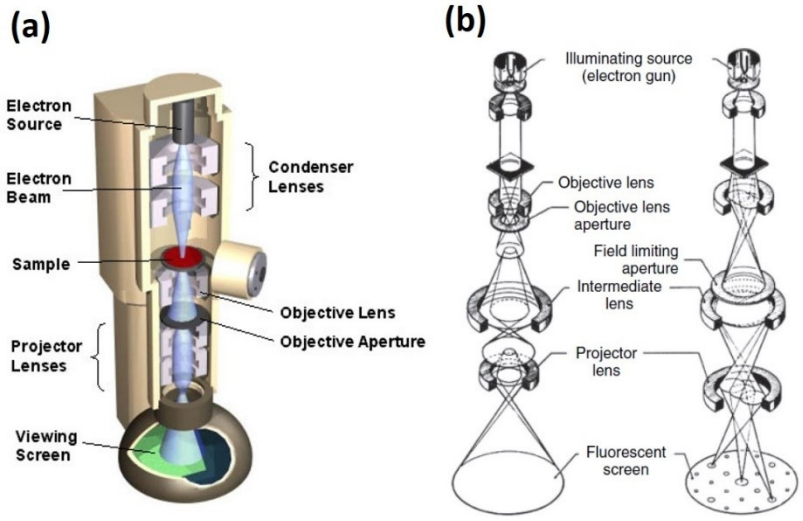

Figure 3.3. (a)Transmitted electron Microscope (b) Scheme of lens assembly and ray path diagram forming the image (left) or the diffraction pattern (right). Adapted from Lamberti *et al.*[6]

Low-resolution TEM (100 kV) allows a statistical description of the size and shape of NCs. High resolution TEM reveals the crystal structure, defect nature and distribution and chemical information from nanometric regions of the sample with atomic resolution.

In this study the samples were prepared by dropping dilute suspensions of nanocrystals (NCs) onto carbon coated aluminum grids. High-resolution TEM (HRTEM) imaging and energy-dispersive X-ray spectroscopy (EDS) analyses, the latter combined with high-angle annular dark field (HAADF)-scanning TEM (STEM) imaging, were carried out with a JEOL JEM-2200FS microscope equipped with a Schottky emitter working at an accelerating voltage of 200 kV, a CEOS spherical aberration corrector for the objective lens and a Bruker Quantax 400 system with a 60 mm2 XFlash 6T silicon drift detector (SDD).

Energy dispersive X-ray (EDX)

The energy-dispersive X-ray spectroscopy (EDX) is used for chemical analysis of sample. The NCs are irradiated with a high energy beam of electrons. The electrons in the inner shells of the atoms can be excited producing, in the relaxation to the ground level, X-ray emission with. The X-rays emitted
from a specimen can be detected and measured by an energy-dispersive spectrometer connected to the TEM. As the energy of the X-rays are characteristic of the difference energy between the two shells and of the atomic structure of the emitting elements, elemental composition of the specimen can be measured. Thus, the chemical analysis and mapping of the NCs, especially for medium-heavy and heavy elements is achieved with this technique.
The EDS spectra were quantified using the Cliff-Lorimer method for the Cu Ka, Se Ko, S Ka, Ag La, Cd Lo, Hg Lo peaks, and the reported STEM-EDS maps are obtained by integrating the intensities over the same peaks, except for Cd maps, where the LB peak was used. In case of EDS maps on partially Ag+-exchanged core/shell CdSe/CdS NRs, the Ag La and Cd LB peaks were integrated over a narrow range (55% or the peak area) due to partial superimposition of the respective peaks in the L series. High resolution (HR) TEM and Selected Area Electron Diffraction (SAED) analyses were performed on a JEOL JEM-2200FS microscope equipped with a Schottky emit-ter operated at 200 kV, a CEOS spherical aberration cor-rector of the objective lens, and an in-column energy filter (Omega-type).

3.4 Scanning Electron Microscopy (SEM) analyses and Energy Dispersive X-ray spectroscopy (EDS) characterization.

The samples were prepared by spin coating dilute solutions of NCs onto silicon wafers. Low-resolution SEM measurements were performed on a JEOL-JSM-6490LA scanning electron microscope operating at an acceleration voltage of 10 kV and while high-resolution SEM images were acquired in a JEOL JSM-7500FA. The EDS characterization was performed in a JEOL-JSM-6490LA microscope using 10 kV.

3.5 UV-vis Optical absorption and photoluminescence measurements in solution

Photoluminescence spectroscopy is a non-contact, non-destructive method for probing the electronic structure of materials. It is a powerful tool to investigate the energy levels within the bandgap, electronic structure, optical and photochemical properties of semiconductor materials. When light is directed onto a sample, it is absorbed, and the process called photoexcitation occurs. The photo-excitation results in the excitation of electrons to a higher permissible electronic state. The excited electrons release energy as it relaxes and returns to a lower energy level. The energy of the emitted light relates to the difference in energy levels between the two electron states involved in the transition between the excited state and the equilibrium state. The radiative emission of light or luminescence through this process is photoluminescence.

The relationship of the frequency of the absorbed radiation to the energy gap (*ΔE*) in UV spectroscopy is given by Planck's law:

$$\Delta E = h\nu = \frac{hc}{\lambda} \qquad (3.4)$$

Where h is the Planck's constant, c is the speed of light, λ is the wavelength of the radiation that is being absorbed and ν is $\frac{c}{\lambda}$.

The intensity and spectral content of this photoluminescence is a direct measure of various important material properties, i.e. surface state density from intensity variations and the width of the spectrum and being the surface states linked to interruption of the periodic arrangement of the atoms , it can give an idea about the occurrence of impurities on the surface. In order to determine an exact excitation wavelength in PL measurement it is desirable to measure the excitation spectrum, and, in the case of the absorption spectrum, the optimal wavelength corresponds to maximum of absorption.

In this study the UV-Visible absorption spectra were recorded using a Varian Cary 5000 UV-Vis-NIR spectrophotometer (Agilent Technologies). The steady state PL spectra were collected on an Edinburgh Instruments FLS920 spectrofluorometer by exciting the samples with a Xenon lamp at 450 nm. NC samples were dispersed in toluene and measured in quartz cuvettes with a path length of 1 cm A dispersion of NCs was diluted or in tetrachloroethylene (TCE) to ensure no interference from the solvent. In NIR extinction measurements was prepared inside a nitrogen filled glovebox.

3.6 UV-vis Photoluminescence measurements in film

The UV-Vis-NIR absorption spectra of the NCs in films on glass substrates were acquired using a Varian Cary 5000 UV-Vis-NIR spectrophotometer (Agilent Technol-ogies). For Raman and PL spectra, a Renishaw inVia was used, equipped with a 50× (0.75 N.A.) objective with an excitation wavelength of 532 nm. For PL spectra of films on glass, time exposure and laser power were kept at 10s and < 0.5 mW, respectively, to avoid the damage of the samples during the measurement. The Raman spectra were acquired from NC films deposited onto SiO2/Si substrates with power < 0.1 mW

3.7 Photoconductivity and Device fabrication

A good understanding of charge carrier transport and electrical conduction is essential for selecting or developing electronic materials for device applications: they are necessary tools for the optimization of the growth procedures of NCs on large scale. Currently, electrical characterization includes a very large number of techniques which investigate the effects related with surface or the interface of the NCs because these zones play a major role the in the electrical and optical behavior. [6–9] The current-voltage method allows for investigating the charge transport and getting and indirect information of the defects on the material. The simplest test uses a constant monochromatic light source generate equal excess densities of free electrons, n, and holes, p, $\Delta n = \Delta p$, that lead to a change in the conductivity by:

$$\Delta\sigma = \sigma_{ph} = q(\mu_n \Delta n + \mu_p \Delta p) \qquad (3.5)$$

where q is the electronic charge and μ_n and μ_p are the electron and hole mobilities, respectively. σ_{ph} is termed the steady-state photoconductivity. The basic experimental arrangement is illustrated in Figure 3.4, where a light source (typically quartz, tungsten, xenon lamp) is dispersed by a monochromator and focuse onto the sample and then, when a potential

difference V is applied, a photocurrent Iph is recorded. The corresponding photoconductivity σph=Iph/(AF), where F=V/L is the applied electric field. The incident light is modulated by a mechanical chopper, and the modulation frequency and phase are used as a reference for a lock-in amplifier of chopping. This allows to measure very weak photocurrents .Typically, for thin film than bulk samples, coplanar electrodes contacts (gold in Figure 3.4) are prepared by evaporation through a shadow mask onto the film surface.

When the light is turned on, the photocarrier density evolves with time, through trapping, emission and recombination[10]. This may be highly complex depending on the material properties and its configuration. When the light is turned off the generation of the photocarrier is stopped, but the recombination kinetics are not immediately altered: because of the presence of traps, carriers may be trapped and emitted many times before they recombine[9]. Consequently, the initial photocurrent decay is not instantaneous, and it may assume exponential-like tail accordingly to strong or weak re-trapping conditions, governed by the relative probabilities of free carrier capture by traps and recombination centers.

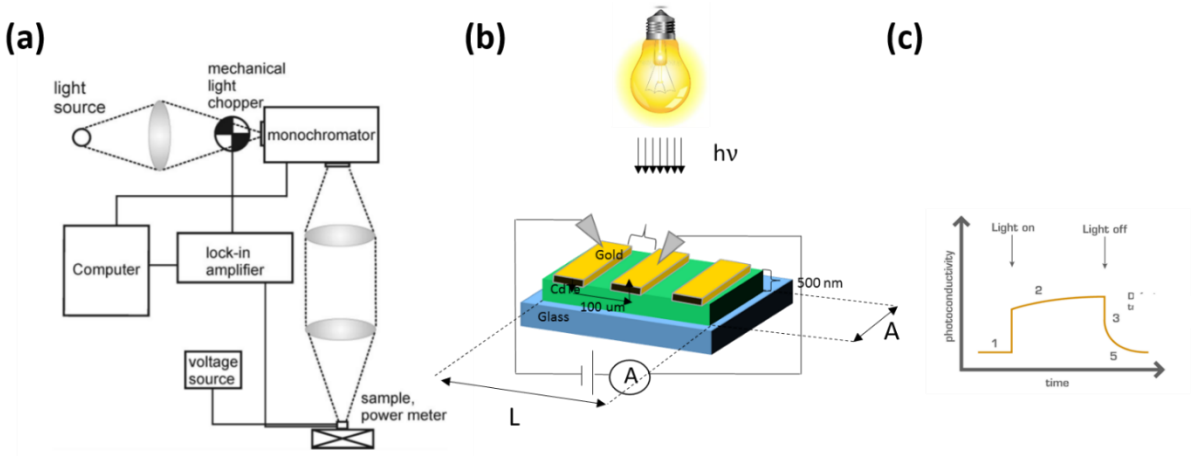

Figure 3.4. Schematic of device based on CdTe NCs for photoconductivity test. (a) experimental setup for photoconductivity measurements (from Talapin*et al.*, 2010 [11])(b) configuration of the photoconductive measurement where L and A are the length and the cross-sectional area of the sample (c) spectral photoconductivity curve time development response measured under light monochromatic illumination.

Thus, current-voltage studies, that are widely used in the study of bulk can give detailed insight of the electrical behavior also of NCs devices.

We used this technique in the study of CdTe NCs deposited on glass substrate as thin film. The glass substrates were cleaned in an ultrasonic bath, first with acetone, then by isopropanol (8 min each step), and finally dried with a N_2 flow. A subsequent N_2 plasma treatment was carried out. Metal deposition (Au, 80 nm) was made by e-beam evaporation (Kenosistec® e-beam

evaporator) with a shadow masks to define 1 mm x 1mm pads separated by ca. 100 µm. The sample was kept at 20°C during the metal deposition to avoid any additional annealing effects. Electrical characterization was performed at room temperature under air in a probe station from Janis® Research meter in a two-probe configuration. The measurement procedure was controlled by a PC using LabView®. Illumination was provided through an optical window using laser diodes coupled into a fiber and focused on the sample in a spot size of approximately 1 mm, aligned on the devices with micrometer-controlled stages. As light sources, mounted light emitting diodes (LEDs) from ThorLabs with nominal emission wavelength at 455 nm (M455L4-royal blue), 530 nm (M505L4-cyan) and 625 nm (M625L4-red) were used. A mechanical shutter was used to block the light passing through the window for dark measurements. Before measuring the photo response, current-voltage (I-V) characterization in the dark was performed. The photoresponsivity was assessed for photoexcitation intensities ranging from 3 to 2000 mW cm^{-2} according with the light source and both using a continuous modulated light with a Keithley 2600 SMU.

3.8 Fourier Transform Infrared (FTIR) spectroscopy.

Photon energies associated with the infrared (IR) region of the spectrum are in the order of 8-40 kJ/mole (2-10 kcal/mole)[12] and it is not enough to break a covalent bond, but it is the right amount of energy to stretch or bend covalent bonds of organic groups, in fact infrared spectroscopy has been called as *vibrational spectroscopy*.[12] There are two kind of molecular vibrations: (i) stretching in which the distance between two atoms increases and decreases in a rhythmic manner, but they remain aligned along the bond axis and (ii)bending in which the positions of atoms change relative to the bond axis. For molecules composed by many atoms there are numerous fundamental vibrations (see Figure 3.5) Due to the combinations of this vibrations, molecules experience a variety of motions that are characteristic of their component atoms. Thus, organic compounds absorb infrared radiation which corresponds to the energy of these vibrations' characteristics of their structure.

The exact frequency at which a given vibration occurs is determined by the strength of the bonds involved and the mass of the component atoms. The general region of the IR spectrum where the vibrational bands of the organic group are observed is from 4000 to 500 cm^{-1} range

as shown in Figure 3.5.

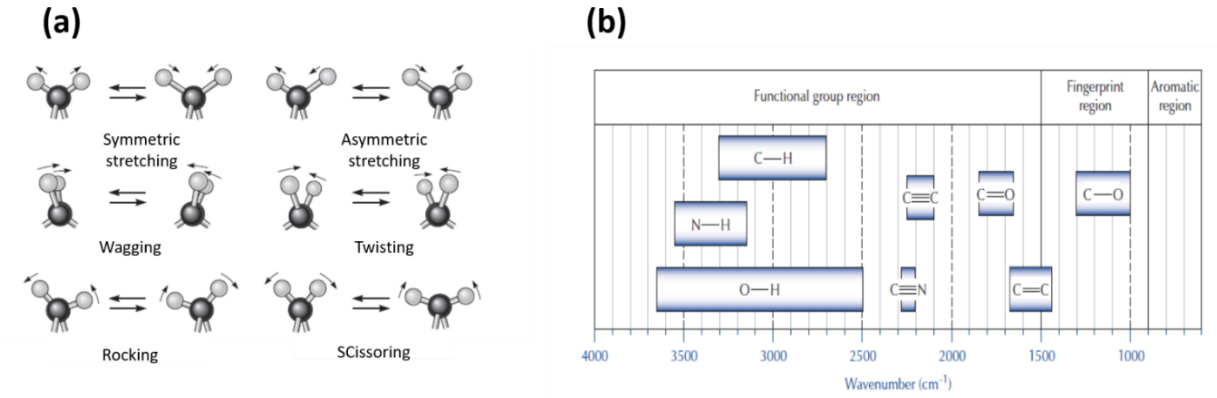

Figure 3.5. (a) typical vibrational modes of methylene group CH2 (b)Typical regions where specific bonds are found in IR window. Specific funcittonal groups present on the surfactants used in colloidal synthesis are easily identifiable withIR spectroscopy. Adapted from Hickinbottom *et al.* [12]

We adopted Fourier Transformed Infrared Spectroscopy to identify the surfactants bonded to the surface of CdTe NCs. In particular CdTe films were scratched, weighted and mixed with KBr powder in a proportion of NCs:KBr= 0.5 mg: 50 mg (1% w/w) and ground with a pestle in an agate mortar. The mixture was put in a die and pressed for 3 min with 3 Tons producing 12 mm diameter pellets which were analyzed by a Equinox 70 FT-IR, Bruker Vertex® FTIR spectrometer. All spectra were recorded in the range from 3800 to 600 cm^{-1} with a resolution of 4 cm^{-1}, accumulating 128 scans. A KBr pellet was used as blank (or reference).

3.9 X-ray Photoelectron Spectroscopy (XPS) characterization.

X-ray Photoelectron Spectroscopy (XPS) is a surface analysis accomplished by irradiating a sample with monoenergetic soft x-rays. Generally, Mg Kα (1253.6 eV) or Al Kα (1486.6 eV) x-rays are used to interact with atoms, causing electrons to be emitted by the photoelectric effect with a kinetic energy equal to:

$$KE = h\nu - BE - \phi_s \qquad (3.6)$$

Where h ν is the energy of the photon, BE is the binding energy of the atomic orbital from which the electron originates, i.e. 1s,2s,2p,3s specific for every element,, and ϕ_s is the spectrometer work function.

Figure 3.6 show the most commonly configuration used which consists of a set of concentric hemispherical deflection electrode and adjustable slits to regulate both source size and angular acceptance [13]. Beyond measuring photoelectron energies, a critical importance is given to each peak intensity or feature. Then it is possible to evaluate the kinetic energy and number of electrons that escape from the surface (1 to 10 nm) of the NCs and the chemical composition in a qualitative and quantitative way.

In this study we performed XPS measurements by a Kratos Axix Ultra DLD spectrometer, using a monochromatic Al Kα source (15kV, 20mA). The photoelectrons were detected at a take-off angle of $\phi = 0°$ with respect to the surface normal. The pressure in the analysis chamber was maintained below 7×10^{-9} Torr for data acquisition. The data was converted to VAMAS format and processed using CasaXPS software, version 2.3.17. The binding energy (BE) scale was internally referenced to C1s peak (BE for C-C = 284.8 eV).

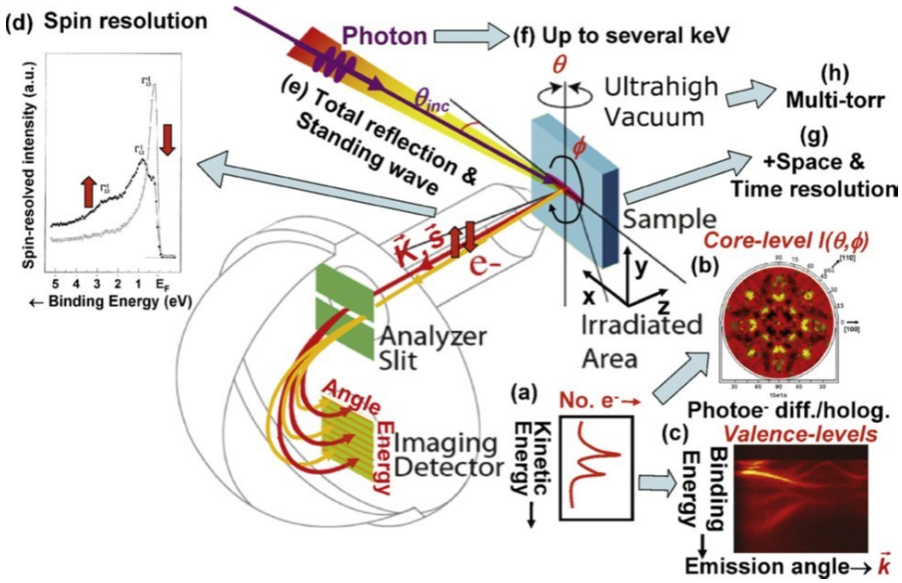

Figure 3.6. Illustration of typical X-ray photoelectron spectroscopy experiments and various type of measurements : (a)energy distribution curves (b) core-level photoelectron diffraction for angle-resolved photoemission (ARPES)(c) valence-band mapping or binding energy vs $\vec{k}$ plots (d) spin-resolved spectra (e) total reflection and/or a standing wave in the sample after having excited with incident X-rays (f) using much higher photon energies than have been typical in the past, (g) taking advantage of space and/or time resolution, and (h) surrounding the sample with high ambient sample pressures of several torr (from Fadley *et al.*[14]).

REFERENCES

1. Boss CB, Fredeen KJ. Concepts, Instrumentation and Techniques in Atomic Absorption Spectrophotometry. *North*. 1997.

2. Dean J. *Practical Inductively Coupled Plasma Spectroscopy*.; 316AD.

3. Guo T. Physical, chemical and biological enhancement in X-ray nanochemistry. *Phys Chem Chem Phys*. 2019. doi:10.1039/c9cp03024g

4. Guo J. *X-Rays in Nanoscience: Spectroscopy, Spectromicroscopy, and Scattering Techniques*.; 2010. doi:10.1002/9783527632282

5. Dünkel L. Fundamentals of Crystallography. *Zeitschrift für Phys Chemie*. 1997;198(Part_1_2):273-274. doi:10.1524/zpch.1997.198.part_1_2.273

6. Lamberti C. *Characterization of Semiconductor Heterostructures and Nanostructures*.; 316AD.

7. Kasap S, Koughia C, Ruda HE. Electrical conduction in metals and semiconductors. In: *Springer Handbooks*. ; 2017. doi:10.1007/978-3-319-48933-9_2

8. Polman A, Knight M, Garnett EC, Ehrler B, Sinke WC. Photovoltaic materials: Present efficiencies and future challenges. *Science (80-)*. 2016;352(6283). doi:10.1126/science.aad4424

9. Kasap S, Koughia C, Ruda H, Johanson R. Electrical Conduction in Metals and Semiconductors. In: *Springer Handbook of Electronic and Photonic Materials*. ; 2006. doi:10.1007/978-0-387-29185-7_2

10. Guyot-Sionnest P. Electrical transport in colloidal quantum dot films. *J Phys Chem Lett*. 2012;3(9):1169-1175. doi:10.1021/jz300048y

11. Talapin D V., Lee JS, Kovalenko M V., Shevchenko E V. Prospects of colloidal nanocrystals for electronic and optoelectronic applications. *Chem Rev*. 2010;110(1):389-458. doi:10.1021/cr900137k

12. HICKINBOTTOM WJ. *Technique in Organic Chemistry*. Vol 180.; 1957. doi:10.1038/180567a0

13. Briggs, D.Wanger, C. D., Riggs, W. M., Davis, L. E., Moulder, J. F., Muilenberg GE. Handbook of X-ray Photoelectron Spectroscopy: a reference book of standard data for use in x-ray photoelectron spectroscopy. *Perkin-Elmer Corp*. 1979.

14. Fadley CS. X-ray photoelectron spectroscopy: Progress and perspectives. *J Electron Spectros Relat Phenomena*. 2010. doi:10.1016/j.elspec.2010.01.006

Chapter 4. Metastable CdTe@HgTe core@shell Nanostructures Obtained by Partial Cation Exchange.

Irene Rosina, Beatriz Martin-Garcia, Davide Spirito, Zhiya Dang, Graziella Gariano, Sergio Marras, Mirko Prato, Roman Krahne, Luca De Trizio and Liberato Manna. Metastable CdTe@HgTe core@shell Nanostructures Obtained by Partial Cation Exchange Evolve into Sintered CdTe films Upon Annealing, Chem. Mater. **2020**, 32, 7, pp 2978–2985.

Abstract

Partial Hg^{2+} → Cd^{2+} cation exchange (CE) reactions were exploited to transform colloidal CdTe nanocrystals (NCs, 4-6 nm in size) into CdTe@HgTe core@shell nanostructures. This was achieved by working under a slow CE rate, which limited the exchange to the surface of the CdTe NCs. In such nanostructures, when annealed at mild temperatures (as low as 200°C), the HgTe shell sublimated or melted and the NCs sintered together, with the concomitant desorption of their surface ligands. At the end of this process, the annealed samples consisted of ligand-free CdTe sintered films containing an amount of Hg^{2+} that was much lower than that of the starting CdTe@HgTe NCs. This procedure was then used to fabricate a proof of concept CdTe-based photodetector exhibiting a photoresponse up to 0.5 A/W and a detectivity of ca. 9·108 Jones under blue light illumination. Considering the high temperatures (above 350°C) and post process ligand stripping steps that are currently used in the preparation of CdTe thin films employed in photovoltaic technology, our strategy, if finely optimized, may find application in the fabrication of future photo-conductive devices.

4.1 Introduction

As discussed in previous chapters, , different types of nanostructures can be accessed by means of CE,depending both on the miscibility of the reactant and of the product materials, and on the kinetics of the CE reaction: i.e. alloy NCs, doped systems, dimers (also termed as “Janus-like”), and core@shell (or core@graded-shell) heterostructures, the latter even with elaborate architectures (quantum wells, multiple-cores@shell, *etc.*).[2,9-10] CE reactions, especially if performed at low temperatures, can even lead to metastable nanostructures (*i.e.* kinetically accessed).[2] These structures, in turn, can be transformed to more stable ones if subjected to either e-beam irradiation or annealing.[2, 10-16] For example, different groups have demonstrated that core@shell structures prepared by partial CE reaction (*i.e.*, Cu_2Te@PbTe, Cu_2Te@SnTe, PbSe@CdSe *etc.*) transform, upon heating, to more thermodynamically stable configurations, such as the dimer structures in which the interface energy between the two materials is

minimized.[10, 14]

Among the different CE reactions involving metal chalcogenide NCs, the CdTe → HgTe transformation is of particular interest as it leads to NCs having a bandgap ranging from 1.6 eV (bulk CdTe) to ~0 eV (bulk HgTe), and, thus, of relevance for IR sensing, IR detection/imaging and photovoltaics.[17-21] CdTe and HgTe are completely miscible materials, as both have a zincblende crystal structure, with lattice parameters being 6.48 Å and 6.46 Å, respectively, hence with a lattice mismatch of only 0.3%. Alloy $Cd_{1-x}Hg_xTe$ NCs, prepared from CdTe NCs by partial exchange of Cd^{2+} with Hg^{2+} ions, have a photoluminescence (PL) emission that can be tuned from ~500 to ~1100nm.[18-20, 22-26] Such alloy NCs form when the partial CE reaction is performed under thermodynamic control, that is, by assuring a fast CE rate or a long reaction time.[18, 22] This can be achieved by employing highly reactive Hg precursors,[23] alkylamines (which preferentially bind Cd^{2+} cations and favor their extraction from the NCs)[19, 23, 27] and by working at high temperatures (*i.e.* 150°C).[27] On the other hand, at a low rate of partial CE, the product consists of CdTe@HgTe core@thin-shell NCs. Experimentally, this has been realized by working at room temperature (RT), using polar solvents and slow reacting Hg precursors (*i.e.* $Hg(ClO_4)_2$ or $HgCl_2$), and by avoiding ligands that favor the extraction of Cd^{2+} ions.[20, 23, 26, 28-29] The formation of such heterostructures was explained by considering that the CdTe → HgTe exchange occurs through a fast surface exchange, followed by a much slower interdiffusion of the Hg^{2+} ions into the core of the NCs.[20, 22, 24, 26, 28] This phenomenon is particularly evident when executing the reaction on CdTe nanoplatelets, in which the exchange with Hg^{2+} ions was found to be self-limited to the first surface monolayer: this led to the formation of CdTe@HgTe core@shell architectures when working with nanoplatelets that were more than three monolayers thick.[29-31]

While strategies to prepare such CdTe@HgTe NCs and their related optical properties have been investigated in detail,[23] not much is known about their thermal stability. To delve into this topic, in this work we have focused our attention on the products of the partial CE between CdTe NCs (4-6 nm in size) and Hg^{2+} cations performed at a slow rate and their structural and morphological evolution under annealing. A short summary of the experiments is described here. Three samples containing 10%, 30% or 40% of Hg (atomic percentage with respect to Cd) were prepared by adding sub-stoichiometric amounts of a slowly reacting Hg^{2+} precursor (*i.e.* $HgCl_2$)[29] dissolved in methanol to a dispersion of CdTe NCs in toluene at RT. The exchange under such conditions occurred preferentially at the surface of the CdTe NCs, yielding CdTe@HgTe core@shell NCs. Such nanostructures were found to be thermally unstable, as

they underwent the following transformations when annealed at mild temperatures (as low as 200°C): the HgTe external layer sublimated (or melted) and the residual cores sintered together, with the concomitant removal of the native surface ligands (i.e. the ligands used for their synthesis and bound to their surface, see Scheme 1). The final products of the annealing process consisted of ligand-free CdTe sintered films containing only a minor residual amount of Hg^{2+} if compared to that of the starting CdTe@HgTe NCs. Noticeably, the CdTe@HgTe sample that initially contained 10% of Hg^{2+} were transformed into sintered CdTe NCs containing only traces of Hg^{2+} (less than 1%).

.

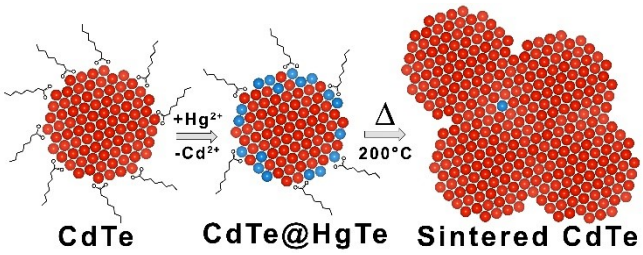

Scheme 4.1. Cation Exchange reaction between CdTe NCs and Hg^{2+} cations, yielding CdTe@HgTe NCs. The latter evolve into sintered CdTe films upon mild annealing at 200°C.

CdTe is a material of great relevance in thin-film photovoltaics technology,[32-33] and strategies are being developed in many groups to lower the costs of film fabrication, for example by solution approaches based on colloidal NC inks. However, to produce bulk-like films from such inks, the deposited NC films need to be annealed at temperatures above 350°C in order to sinter the NCs together and to remove the ligands.[34-39] By leveraging on our $Cd^{2+} \rightarrow Hg^{2+}$ exchange protocol, we could prepare CdTe sintered films using much milder annealing conditions (200°C). These films exhibited a photoresponse up to 0.5 A/W and a detectivity of ca. $9 \cdot 10^8$ Jones, in line with CdTe NC film systems reported in the literature,[40-43] highlighting the potential use of our strategy in the fabrication of future CdTe-based optoelectronic devices.

4.2 **Experimental part**

- **Preparation of the Te stock solution.** A Te precursor stock solution (10% Te by weight, 0.7 M) was prepared in a three-neck flask by dissolving 1.1 g of Te powder (8.6 mmol) in 12 mL (9.9 g) of TOP under inert atmosphere. The solution was heated up to 250°C until the Te powder was fully dissolved. After cooling it down to room temperature, its color turned to straw yellow. The solution was further degassed under

vacuum for 30 min.

- **Synthesis of CdTe Nanocrystals**. The synthesis was adapted from the work of Zhang *et al.*.[34] In brief, CdO 7.5 mmol (960 mg), OA 30 mmol (9.5 3mL) and ODE 10 mL were loaded in a 50 mL flask and degassed at 110 °C for 1 h. Subsequently, the mixture was heated up to 300 °C under Ar in order to get an optically clear solution (indicating the formation of cadmium oleate complexes). This was followed by a further degassing step under vacuum at 110°C to remove the water generated by the reaction. At this point, the flask was heated up to 280°C, followed by the quick injection of TOP-Te (2.86 mL) diluted with 1 mL of ODE. After 10 s from the injection, the heating mantle was removed, and the flask was quickly cooled to room temperature. The resulting NCs were collected by twofold precipitation with anhydrous ethanol from their colloidal solutions in anhydrous toluene followed by dissolution in toluene. The final purified NCs were redispersed in toluene at a concentration of 0.2 M in Cd.

- **Partial CdTe → HgTe cation exchange reaction.** The CE reactions were performed by following the procedure reported by Miszta *et al.*.[44] In detail, a dispersion of CdTe NCs in toluene ([Cd] = 5 mM) was mixed with a solution of $HgCl_2$ in methanol (0.1 M) at room temperature under nitrogen and stirred for 1 min. The reaction was quenched by adding 10 mL of toluene. The NC product was cleaned twice by dispersion in toluene and precipitation by the addition of ethanol. If necessary, in the first cleaning step oleic acid (50 µL) was added to increase the colloidal stability of the resulting NCs. The precipitation was achieved by a mild centrifugation (3000 rpm, 5 min). Different Hg/Cd feeding molar ratios were tested, ranging from 0.1 to 0.4.

4.3 **Results and Discussion**

Spherical CdTe NCs, with a mean diameter of 4.5 ± 1 nm, were synthesized following the procedure reported by Zhang *et al.*[32] (see Figure 4.2). The elemental analysis, conducted *via* ICP-OES, revealed that the composition of the NCs was nearly stoichiometric (i.e. CdTe), and the XRD characterization indicated the presence of a mixture of both CdTe wurtzite (WZ) and zincblende (ZB) structures (ICSD numbers 620518 and 43712, respectively) (Figure 4.1, blue pattern and Table 1). These NCs were used in partial CE reactions with Hg^{2+} cations in order to study the corresponding products and their evolution under annealing. The CdTe NCs were exposed to different Hg/Cd feed molar ratios, ranging from 0.1 (10%) to 0.4 (40%) employing a slowly reacting Hg precursor (*i.e.* $HgCl_2$)[29] dissolved in methanol, with the aim to lower the

CE reaction rate and to limit the exchange to the surface of the NCs. For the same reason, and to avoid any possible reduction of Hg^{2+} to metallic Hg,[24, 45] we did not use any extra ligands, like alkylamines, which are commonly used for this specific type of CE.[19, 29-31] Our CE reaction was, thus, driven only by the higher solubility of CdTe with respect to that of HgTe in polar solvents ($K_{SP}(HgTe) < K_{SP}(CdTe)$).[2, 18, 20, 26, 28]

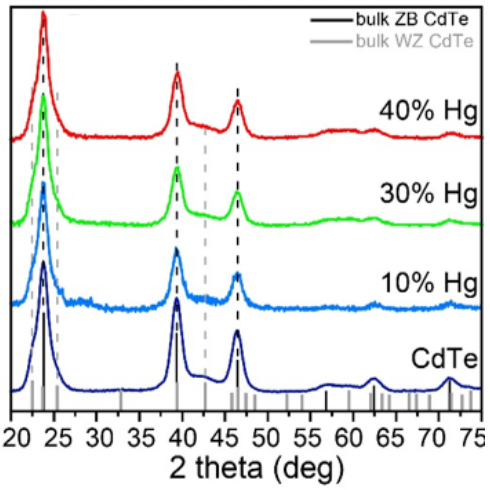

Figure 4.1. XRD patterns of CdTe and CdTe-Hg samples together with the bulk reflections of WZ (ICSD numbers 620518) and ZB (ICSD number 43712) CdTe structures.

The products of these partial CE reactions, which will be named CdTe-Hg 10%, 30% and 40%, were NCs retaining the size and shape of parental CdTe NCs, as revealed by TEM (Figure 4.2).

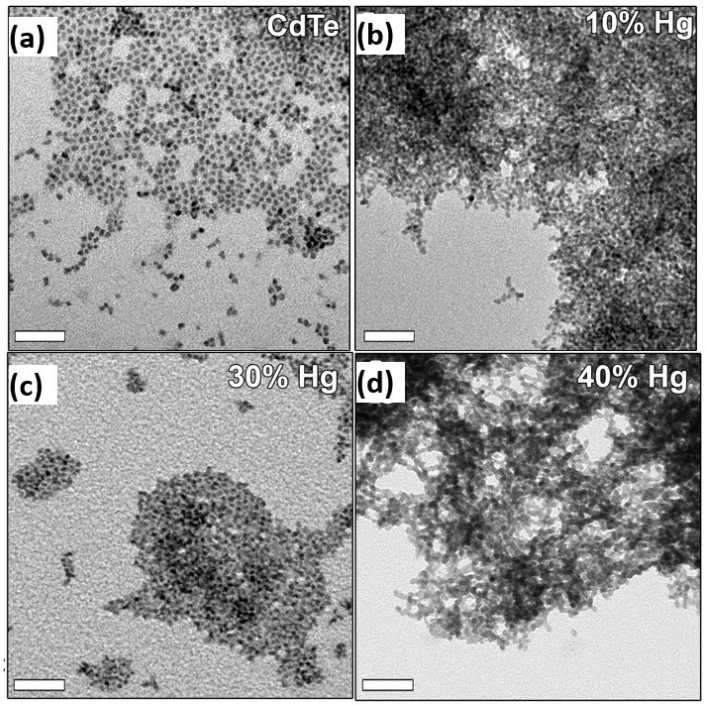

Figure 4.2. TEM images of (a) CdTe and (b) CdTe-Hg 10% NCs. (c) CdTe-Hg 30% and (d) CdTe-Hg 40%. The scalebars are 50nm.

The ICP elemental analysis indicated that the extent of the Cd-for-Hg substitution was essentially in line with the Hg/Cd feed molar ratios employed (Table 4.1).

	Pre Annealing		Post Annealing	
Hg/Cd feed ratio	Stoichiometry[a]	Size (nm)[b]	Stoichiometry[a]	Size (nm)[b]
/	CdTe	4.2	CdTe	5.6
10%	$Cd_{0.9}Hg_{0.1}Te$	6.2	$Cd_{0.9}Hg_{0.01}Te$	19.6
30%	$Cd_{0.7}Hg_{0.3}Te$	5.8	$Cd_{0.9}Hg_{0.1}Te$	15.5
40%	$Cd_{0.6}Hg_{0.35}Te$	6.2	$Cd_{0.9}Hg_{0.3}Te$	15.2

[a]Measured via ICP-OES. [b]Calculated via the Scherrer formula

Table 4.1. Composition and size of starting CdTe NCs and CdTe-Hg NCs before and after the annealing treatment at 200°C.

The XPS measurements further confirmed the results of the ICP elemental analysis, additionally evidencing that Hg was present only in the +2 oxidation state (Hg $4f_{7/2}$ peak position at 100.6 eV), thus excluding the possible presence of metallic Hg (Figure 4.3). According to XRD analyses, the CE reaction did not induce any phase transition in the NCs, since the same ratio

of ZB to WZ phases as in the initial CdTe NCs was found in the products (see Figure 4.1a).

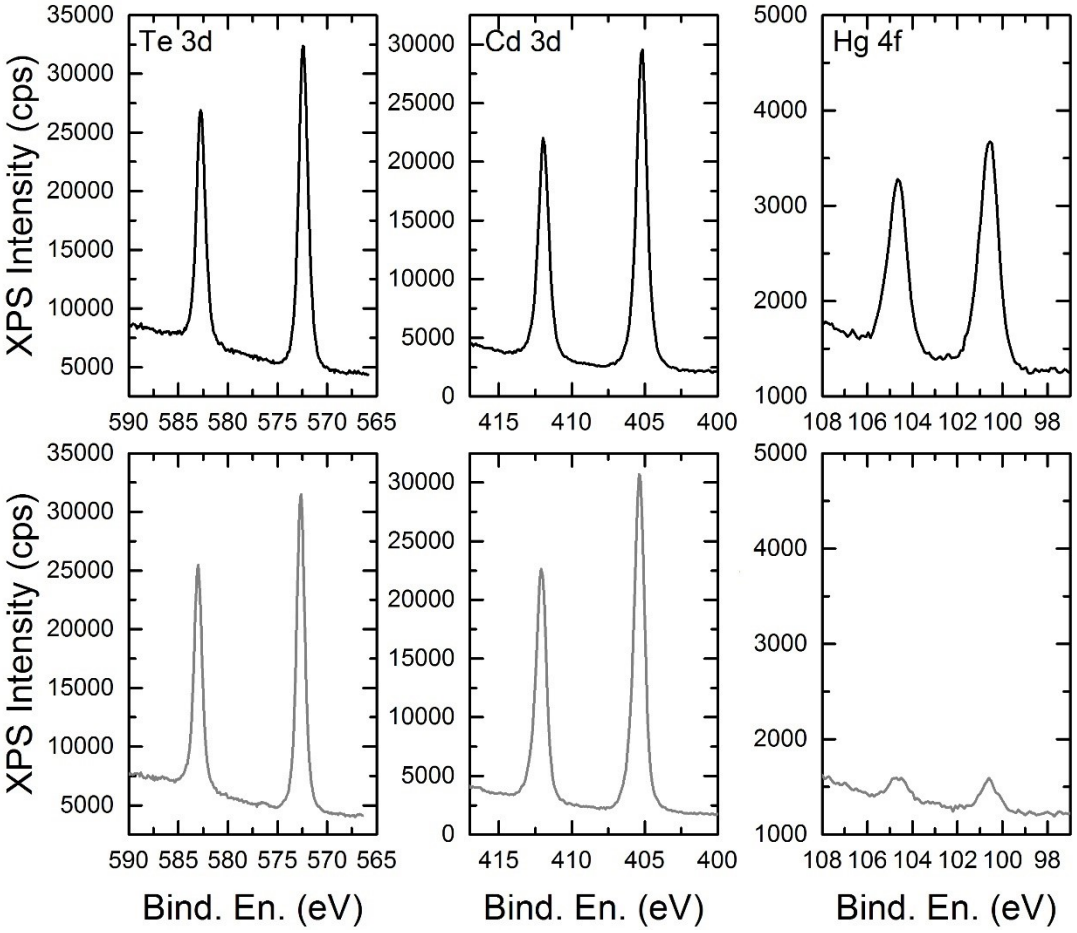

Figure 4.3. XPS spectra of CdTe-Hg 10% NCs before (upper panels) and after annealing (lower panels). Peak positions: Te $3d_{5/2}$ at (572.5 ± 0.2) eV, Cd $3d_{5/2}$ at (405.3 ± 0.2) eV and Hg $4f_{7/2}$ at (100.6 ± 0.2) eV, indicating the presence of Te^{2-}, Cd^{2+} and Hg^{2+} in the sample [NIST X-ray Photoelectron Spectroscopy Database, Version 4.1 (National Institute of Standards and Technology, Gaithersburg, 2012); http://srdata.nist.gov/xps/]. Relative atomic ratios were determined using the integrated area under Cd 3d, Te 3d and Hg 4f principal peaks.

As can be seen from Figure 4.4, the starting CdTe NCs were characterized by an excitonic peak at 631 nm and a photoluminescence (PL) peak at 674 nm with a full width at half maximum (FWHM) of 40 nm. The absorption and PL emission of CdTe-Hg NCs systematically red-

shifted with the increase of Hg in the NCs, while retaining the same linewidth.

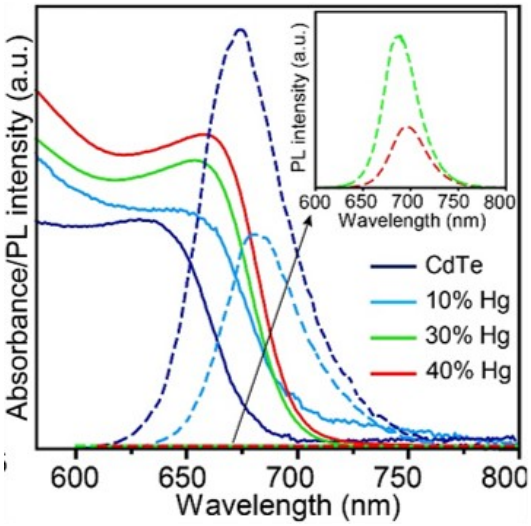

Figure 4.4. Absorption and PL spectra of CdTe NCs before and after partial cation exchange with Hg (λ_{ex} = 450 nm). The inset shows a magnification of the PL spectra of CdTe-Hg 30 and 40% samples.

Such a small red-shift in both PL and absorbance indicated that partial CE did not lead to the formation of alloy NCs (i.e. $Cd_{1-x}Hg_xTe$), whose PL emission would have been expected at much longer wavelengths (*i.e.* 720 nm for $Cd_{0.9}Hg_{0.1}Te$ and 820 nm for $Cd_{0.7}Hg_{0.3}Te$ NCs of 4 nm).[19, 23] Instead, the products of the reaction were CdTe@HgTe core@shell NCs, similarly to what was shown by Smith *et al.*[22] Also, the more $HgCl_2$ was added to the reaction (hence more Hg was incorporated in the NCs) the more the PL intensity of the samples dropped. Compared to the starting CdTe NCs, the PL intensity of the CdTe-Hg 10% NCs sample was reduced by ~50%. In the CdTe-Hg 30% and 40% samples the PL was almost quenched (Figure 4.4). This observation is consistent with the hypothesis of a shell growth (over that of an alloy formation): as revealed by Smith *et al.* the growth of a HgTe shell over a CdTe core leads to the spatial separation of photogenerated carriers and to a lowering of the oscillator strength of the 1st exciton peak.[22] Therefore, a thicker HgTe shell would result in a more efficient quenching of the PL from the CdTe core.

We studied the stability of these NCs by drop-casting them onto a Si substrate and by exposing the resulting film to a thermal treatment (under N_2) from room temperature (RT) to 200°C, while monitoring their structural and compositional evolution. The XRD patterns acquired after the thermal treatment evidenced that all the CdTe-Hg samples underwent sintering upon heating

and that the ZB was preferentially stabilized over the WZ phase (Figure 4.5).

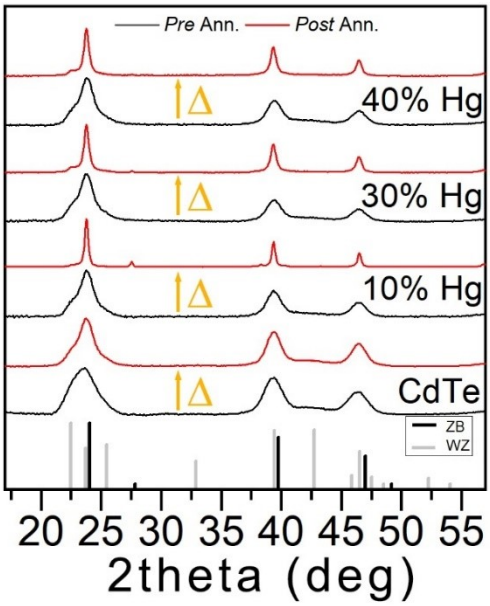

Figure 4.5. XRD patterns of CdTe and CdTe-Hg NC samples subjected to a thermal treatment under N_2 from RT (black curves) to 200°C (red curves). The bulk reflections of WZ and ZB CdTe structures are reported by means of gray and black bars, respectively.

In details, the size of the crystallites of the CdTe-Hg samples, calculated by employing the Scherrer formula, increased from 4-6 nm to 15-20 nm (Table 1 and Figure 4.5). In addition, the corresponding ICP elemental analyses revealed that such sintering was accompanied by a loss of Hg (see Table 1). In this regard, among the three CdTe-Hg samples, the CdTe-Hg 10% one exhibited the largest extent of sintering (from 6.2 to 19.6 nm) and the lowest Hg content at the end of the process (less than 1%, see Table 1).

Motivated by these findings, we investigated more closely the effects of the thermal treatment

on CdTe-Hg 10% NCs by extending the heating range from RT to 350°C (see Figure 4.6).

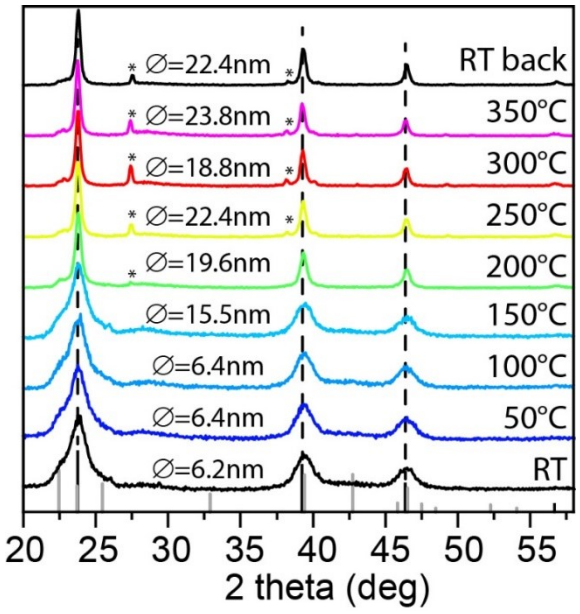

Figure 4.6. XRD patterns of CdTe-Hg 10% NCs subjected to a thermal treatment under N_2 from RT to 350°C and then back to RT (RT-back). The bulk reflections of WZ and ZB CdTe structures are reported by means of gray and black bars, respectively. The metallic Te peaks are marked with asterisks. The diameter of the crystallites reported above each curve was calculated with the Scherrer formula.

The XRD patterns, acquired during such experiments, highlighted that most of the sintering occurred already at 200°C, with not much additional evolution when going from 200°C to 350°C, since in that temperature range the mean grain size increased only from 19.6 to 22.4 nm (Figure 4.6). It was additionally observed that, in the 250-350°C range, the sintering process was accompanied by the formation of metallic Te (Figure 4.6). At the same time, the ICP analysis revealed that the amount of Hg decreased from 1% at 200°C to below the detection limit at 350°C. Overall, these results were quite remarkable, considering that, to sinter a film of colloidal CdTe NCs, one would typically require annealing temperatures above 350°C.[32-39, 46-48] Indeed, as a control, we observed that a non-exchanged CdTe NC sample annealed at 200°C did not undergo any appreciable sintering (Table 1 and Figure 4.5).

In order to better understand the thermal evolution of our CdTe-Hg 10% NCs we carried out additional characterizations via HRTEM, STEM-EDS and XPS analyses. The starting CdTe-Hg 10% NCs were characterized by a mixture of WZ and ZB structures (see Figure 4.7a) and a

Hg content of 10% (see Figure 4.8a), confirming our XRD and elemental analyses.

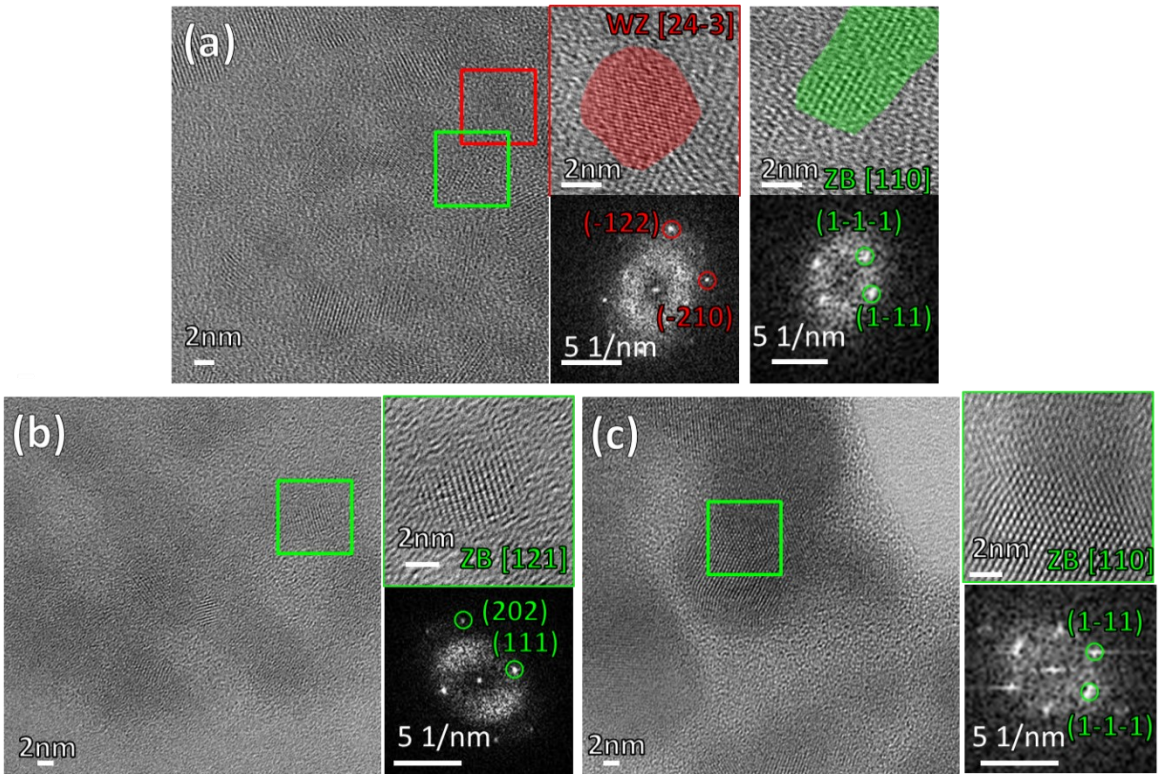

Figure 4.7. HRTEM images of CdTe-Hg 10% NCs before (a) and after annealing at 200°C (b,c) with the corresponding FFT.

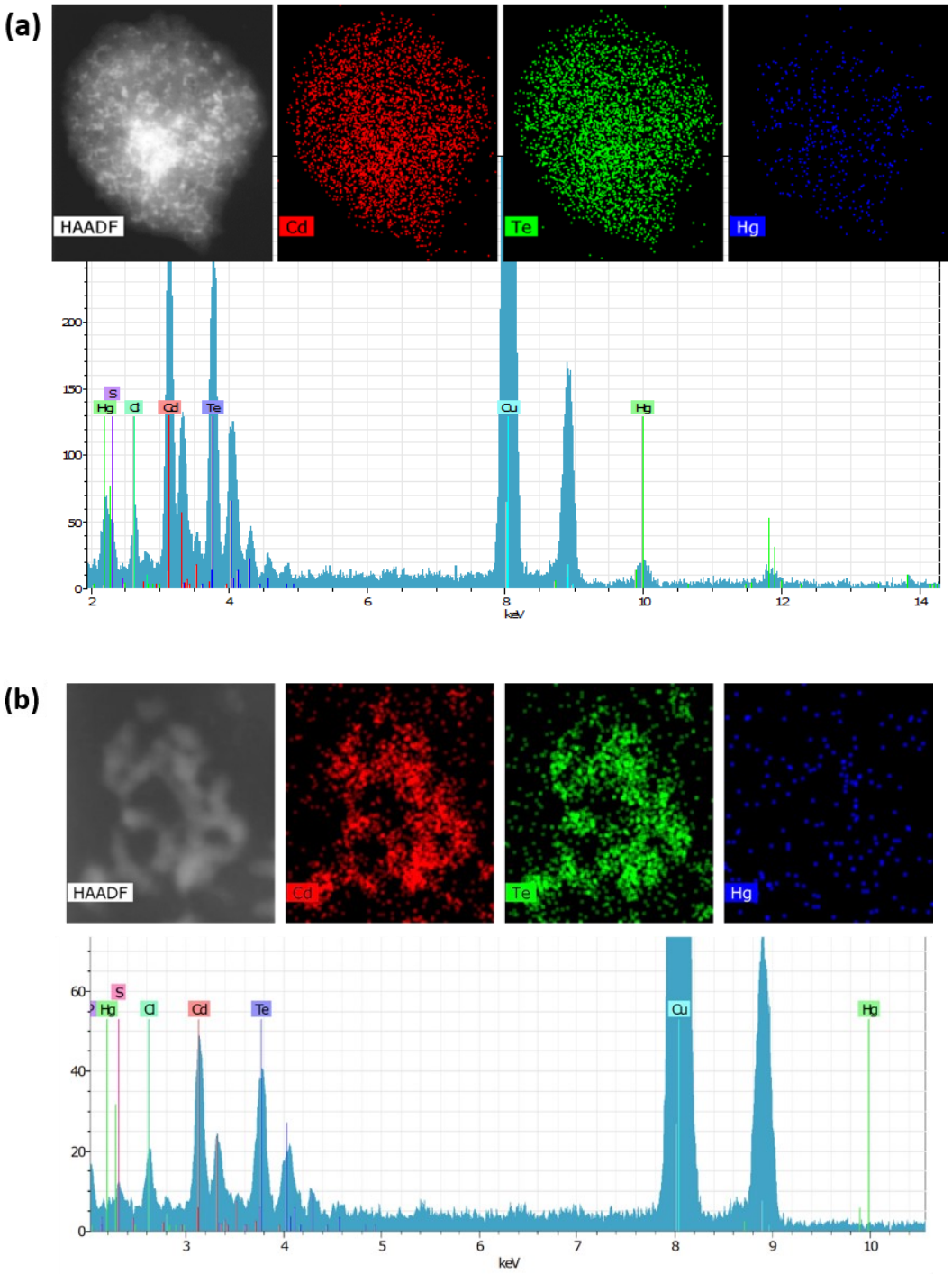

Figure 4.8. STEM-EDX mapping of CdTe@HgTe 10% NCs (top panels) with the corresponding measured spectrum (bottom panel). The composition of the NC ensemble was measured to be $CdHg_{0.1}Te$.

The same NCs were annealed at 200°C under N_2 directly onto the carbon support of the TEM grid, and were then re-examined under the TEM (see the details in the Experimental Section): the resulting NCs had fused together, forming a continuous network (Figure 4.9a). Such network was composed of NCs exhibiting fringes compatible with the CdTe ZB structure, in

agreement with the XRD analyses, with no presence of Hg (i.e. the amount of Hg was below the detection limit of our EDS setup, see Figure 4.9, Figure 4.7 b,c and 4.8b).

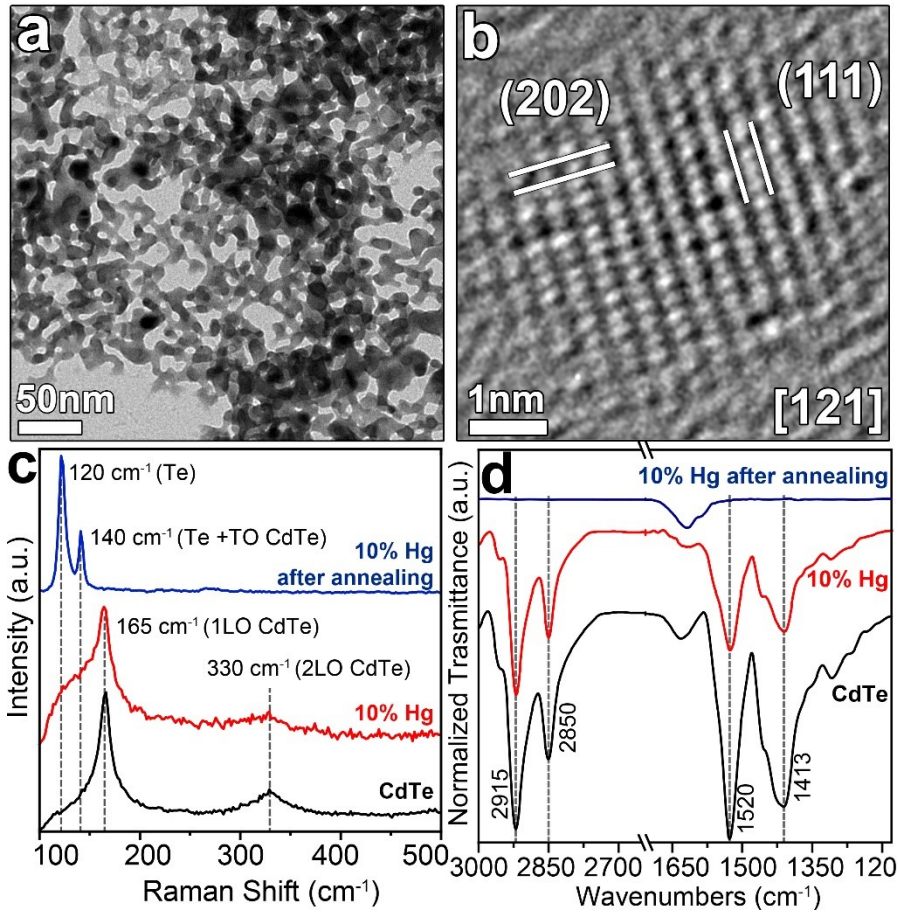

Figure 4.9. (a) TEM and (b) HRTEM images of CdTe-Hg10% NCs after annealing at 200°C for 40s. (b) The lattice fringes of the NCs could be indexed with the ZB CdTe structure. (c) Raman and (d) FTIR spectra of CdTe NCs (black curves), and CdTe-Hg10% NCs before (red curves) and after (blue curves) the annealing. In the Raman spectra, the modes corresponding to CdTe and metallic Te are pointed out to indicate the material evolution after the cation exchange and subsequent sintering at 200°C. In the FTIR spectra the bands related to the carboxylic group (COO^-) and the CH_2 stretching of the OA are indicated. These bands disappeared upon annealing (200°C) indicating the absence of ligands at the end of the thermal treatment.

The XPS analysis of the annealed CdTe-Hg 10% sample indicated the presence of Te, Cd and Hg in -2, +2 and +2 oxidation states, respectively, with the amount of Hg being around 1% (Figure 4.3).

The Raman spectrum of the starting CdTe NCs deposited on silicon substrates (see material chapter 3 for further details) was characterized by bands at 166 and 329 cm^{-1} which correspond to the longitudinal optical (LO) and 2LO CdTe modes (Figure 4.9c).[23, 49] After the exchange with Hg^{2+} cations, a new broad band at lower wavenumbers to LO-CdTe phonon modes (*i.e.* about at 138 cm^{-1}) appeared and was assigned to HgTe modes.[23, 50] After annealing at 200°C,

the modes at 166 and 329 cm^{-1} disappeared and two peaks emerged at 120 and 141 cm^{-1}, which were attributed to the formation of metallic Te, in agreement with what emerged from the XRD analysis (see SI for reference Raman spectra of Te, Figure 4.10 and Figure 4.6).[51]

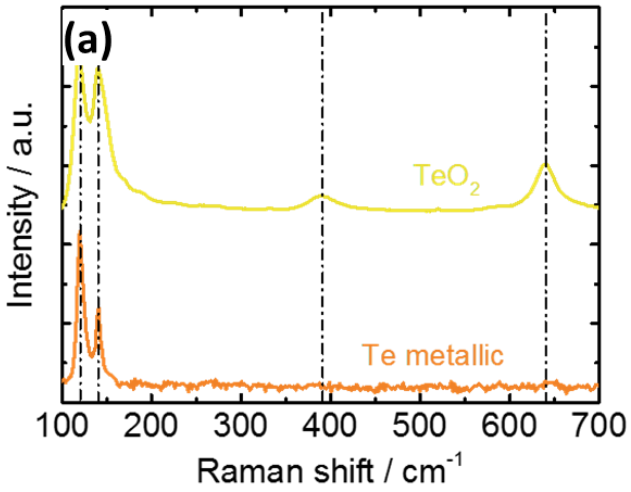

Figure 4.10. Raman spectra of metallic Te characterized by two peaks at 120 and 140 cm^{-1} and TeO_2 with additional peaks at 390 and 640 cm^{-1}.

To analyze the effect of thermal treatment on the organic ligands that coated the surface of the NCs, we performed FTIR analyses on both the unexchanged OA-capped CdTe NCs and the CdTe-Hg 10% NCs before and after the annealing at 200°C. Both samples were characterized by FTIR peaks at ~1520 cm^{-1} and 1413 cm^{-1} which could be ascribed to the asymmetric and the symmetric stretching modes of the COO^- group, and 2915 and 2850 cm^{-1} corresponding to the CH_2 stretching of the OA. All these bands disappeared in the final annealed sample, indicating the absence of ligands in this sample (see Figure 4.9d).[34] The broad band peaked at 1600 cm^{-1} characterizing all the samples was due the residual water inside the KBr matrix employed in FTIR analyses.

According to the experiments, the following picture can be drawn: upon heating at 200°C or above, the starting CdTe-Hg NCs, instead of simply evolving into alloy $Cd_{1-x}Hg_xTe$ NCs, underwent a substantial loss of Hg and Te (most likely by sublimation or melting of the HgTe superficial domain(s))[21] with the concomitant loss of surfactants and sintering of the NCs. In details, when the amount of Hg inside the CdTe-Hg NCs was sufficiently low (i.e.10%), and the annealing temperature was as low as 200 °C, the final sintered film had essentially a CdTe composition, or, in other words, nearly all the initial Hg was expelled. On the other hand, when the amount of Hg inside the starting CdTe-Hg NCs was higher (above 30%), the film after

annealing had a $Cd_{1-x}Hg_xTe$ composition. In this case, not all the HgTe had been able to sublimate or melt and part of the Hg had diffused into the film forming, most likely, an alloy. In all the cases, part of the extracted Te recrystallized in the form of metallic Te.

Prompted by these results, we decided to exploit our strategy to fabricate and test a proof of concept CdTe thin-film based photodetector device (see Chapter 3 for details on device fabrication). Initially, we employed an ink of CdTe-Hg 10% NCs, however, with this material we did not obtain homogeneous CdTe films (see Figure 4.11a-b).

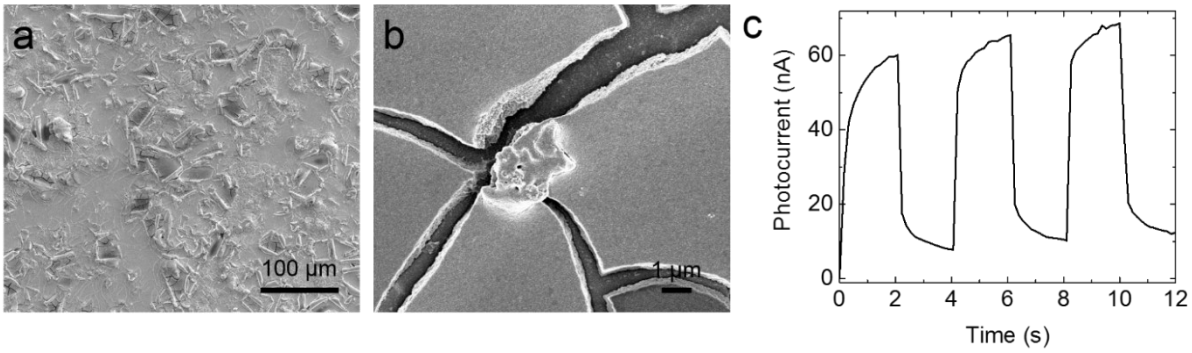

Figure 4.11. (a, b) Representative SEM images of a CdTe film obtained by spin coating CdTe-Hg 10% NCs and by annealing at 200°C. (c) Time trace of the photocurrent while the light was switched on and off, at room temperature in air under white light (LED ILH-ON09-VA, 90 mW/cm^2).

We attribute this to the fact that, after the CE, the resulting CdTe-Hg NCs lost colloidal stability forming NCs dispersions that were cloudy (due to the presence of aggregates). Indeed, the responsivity (R) of the device prepared with the sintered CdTe-Hg 10% NCs reached only ca. $7x10^{-4}$ A/W under white light (see Figure 4.11c). In order to improve the quality of the films, we also devised a different strategy, consisting of first depositing CdTe NCs to form homogeneous films, followed by CE directly on the films. In detail, we prepared 3-layer sintered films by first spin coating the CdTe NCs, and then by dipping the resulting film into a solution of Hg^{2+} cations in methanol (achieving the desired extent of the Cd→Hg CE, that is 10% of Hg) and, eventually, by annealing the exchanged film at 200°C for 40 s. This process

was repeated three times (see Scheme 4.2).

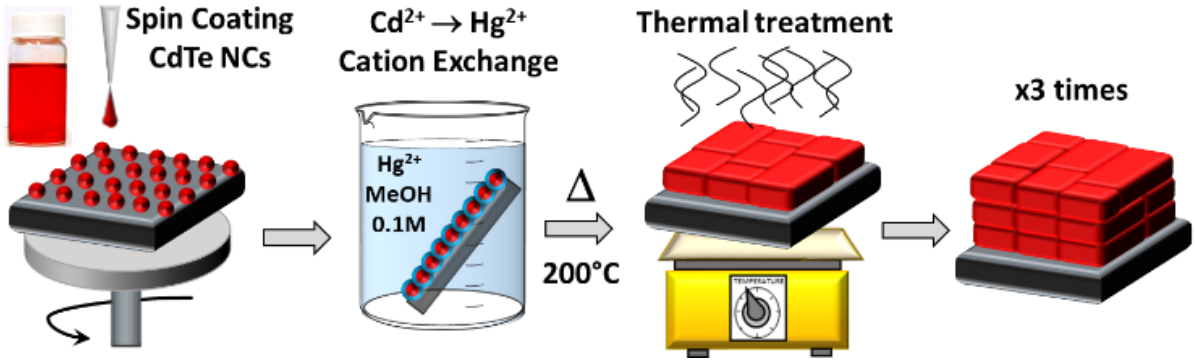

Scheme 4.2. Sintered CdTe thin film preparation starting from CdTe NCs.

The morphology and composition of each CdTe layer and of the final layer stack was characterized by high-resolution scanning electron microscopy (HRSEM) analysis, which confirmed our previous results: upon annealing at 200°C the NCs film, initially composed of 4.2 nm NCs (Figure 4.12a), underwent sintering with the formation of large grains, in this case having a mean size of hundreds of nm (Figure 4.12b). At the same time, the amount of Hg inside

the film, measured by SEM-EDS, dropped from to 10% to 1%.

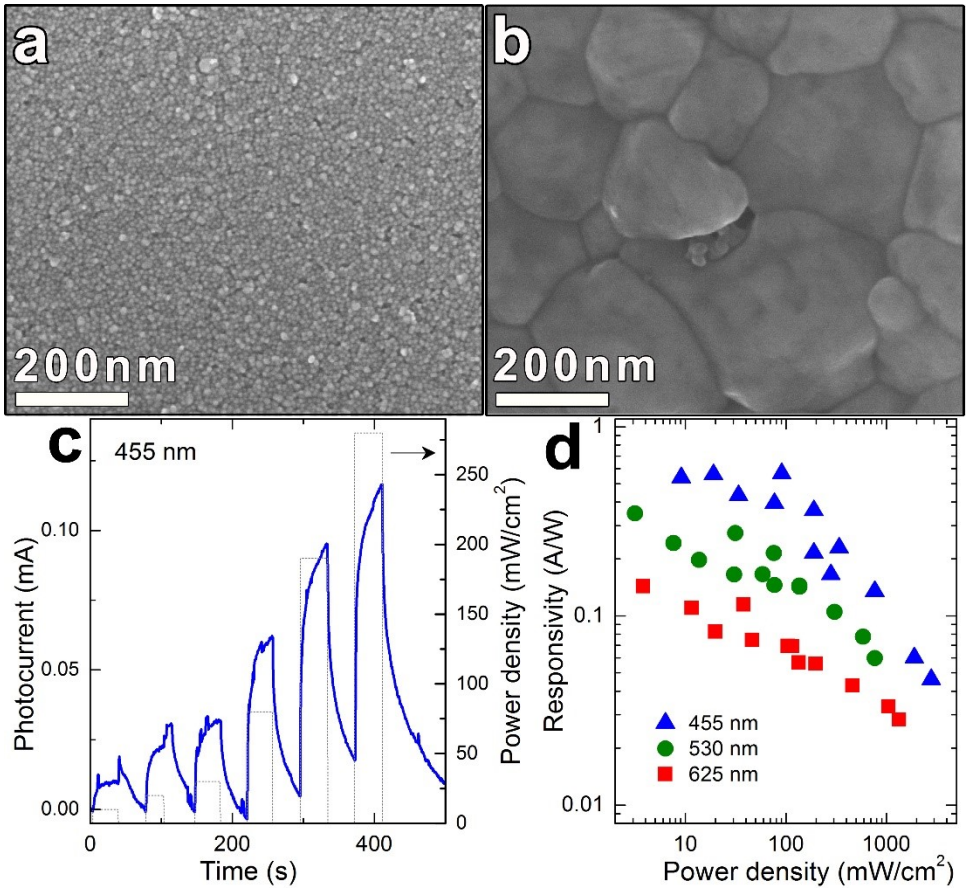

Figure 4.12 HRSEM images of a CdTe layer film before (a) and after sintering (b). (c) Time trace of the photocurrent (dark current at *t*=0 s, left y-axis) while the light was switched on and off, at room temperature in air under 455 nm excitation at different power density (right y-axis). (d) Responsivity as a function of power density at different photoexcitation wavelength: 455 nm (blue), 530 nm (green) and 625 nm (red). The on/off signal was let to stabilize for 20 s for this evaluation.

Under visible light in the blue (455 nm), green (530 nm) and red (625 nm), the device obtained with this strategy showed a slow photoresponse (Figure 4.12c). Blue light illumination yielded the maximum responsivity (0.5 A/W), with a detectivity of ca 9×10^8 Jones, while red light led to the lowest responsivity (0.1 A/W) in agreement with the absorption spectrum of the material. The photocurrent had a sublinear dependence on light power (P, $I_{pc} \sim P^{0.8}$); therefore, the responsivity (I_{pc}/P) was decreasing with P, as shown in Figure 4.12d. This was attributed to the presence of trap states in the material.[52] Although the performance achieved by our system (R = 0.5 A/W and D = $9\cdot10^8$ Jones) was still far from the best values found in the literature for

optimized systems, such as CdTe NCs-P3HT-PCBM (R = 50 A/W and D = $5 \cdot 10^{12}$ Jones)[40] or chlorine treated CdTe NCs (R = $4 \cdot 10^{9}$ A/W and D = $5 \cdot 10^{17}$ Jones),[42] it outperformed that of several other systems, such as the thiol-capped CdTe NCs prepared by electrostatic self-assembly (R= 0.18 A/W)[41] or the iodine-passivated $CdSe_xTe_{1-x}$ NCs (R= 0.053 A/W and D = $8 \cdot 10^{13}$ Jones).[43]

4.4 **Conclusions**

We synthesized CdTe NCs which were subjected to partial CE with Hg^{2+} cations. This was performed by working at room temperature and by employing $HgCl_2$, a slowly reacting Hg^{2+} precursor, dissolved in methanol. We varied the Hg/Cd feed ratio to prepare three different samples containing 10%, 30% or 40% of Hg, respectively. The products of the exchange, CdTe@HgTe core@shell NCs, when annealed at temperatures as low as 200°C were observed to evolve in the following way: the superficial HgTe melted or sublimated leading to the sintering of residual CdTe cores and to the concomitant removal of the native surface ligands. The Hg content in the resulting sintered CdTe NC films was found to be much lower than that in the starting CdTe@HgTe NCs, while a minor fraction the extracted Te recrystallized in the form of metallic Te. Given the low sintering temperature, we tested this approach to fabricate proof-of-concept photodetectors based on CdTe thin films which exhibited a photoresponse up to 0.5 A/W and a detectivity of ca. $9 \cdot 10^{8}$ Jones under blue light. Considering the high temperatures (above 350°C) and post process ligand stripping steps that are currently used in the preparation of CdTe thin films employed in PV technology, our novel strategy, if further engineered, can represent an alternative method towards the preparation of CdTe thin films at low temperatures starting from NCs inks, for application in photoconductive devices.

REFERENCES

(1) Wang, H.; Butler, D. J.; Straus, D. B.; Oh, N.; Wu, F.; Guo, J.; Xue, K.; Lee, J. D.; Murray, C. B.; Kagan, C. R., Air-Stable CuInSe2 Nanocrystal Transistors and Circuits Via Post-Deposition Cation Exchange. ACS Nano 2019.

(2) De Trizio, L.; Manna, L., Forging Colloidal Nanostructures Via Cation Exchange Reactions. Chem. Rev. 2016, 116, 10852-10887.

(3) Shamsi, J.; Urban, A. S.; Imran, M.; De Trizio, L.; Manna, L., Metal Halide Perovskite Nanocrystals: Synthesis, Post-Synthesis Modifications, and Their Optical Properties. Chem. Rev. 2019.

(4) Rivest, J. B.; Jain, P. K., Cation Exchange on the Nanoscale: An Emerging Technique for New Material Synthesis, Device Fabrication, and Chemical Sensing. Chem. Soc. Rev. 2013, 42, 89-96.

(5) Son, D. H.; Hughes, S. M.; Yin, Y.; Alivisatos, A. P., Cation Exchange Reactions in Ionic Nanocrystals. Science 2004, 306, 1009-1012.

(6) Moon, G. D.; Ko, S.; Min, Y.; Zeng, J.; Xia, Y.; Jeong, U., Chemical Transformations of Nanostructured Materials. Nano Today 2011, 6, 186-203.

(7) Fayette, M.; Robinson, R. D., Chemical Transformations of Nanomaterials for Energy Applications. J. Mater. Chem. A 2014, 2, 5965-5965.

(8) Gupta, S.; Kershaw, S. V.; Rogach, A. L., 25th Anniversary Article: Ion Exchange in Colloidal Nanocrystals. Adv. Mater. 2013, 25, 6923-6944.

(9) van der Stam, W.; Geuchies, J. J.; Altantzis, T.; van den Bos, K. H. W.; Meeldijk, J. D.; Van Aert, S.; Bals, S.; Vanmaekelbergh, D.; de Mello Donega, C., Highly Emissive Di-valent-Ion-Doped Colloidal CsPb1–XMxBr3 Perovskite Nanocrystals through Cation Exchange. J. Am. Chem. Soc. 2017, 139, 4087-4097.

(10) Tu, R.; Xie, Y.; Bertoni, G.; Lak, A.; Gaspari, R.; Rapallo, A.; Cavalli, A.; Trizio, L. D.; Manna, L., Influence of the Ion Coordination Number on Cation Exchange Reactions with Cop-per Telluride Nanocrystals. J. Am. Chem. Soc. 2016, 138, 7082-7090.

(11) Li, H.; Zanella, M.; Genovese, A.; Povia, M.; Falqui, A.; Giannini, C.; Manna, L., Sequential Cation Exchange in Nanocrystals: Preservation of Crystal Phase and Formation of Metastable Phases. Nano Lett. 2011, 11, 4964-4970.

(12) De Trizio, L.; Gaspari, R.; Bertoni, G.; Kriegel, I.; Moretti, L.; Scotognella, F.; Maserati, L.; Zhang, Y.; Messina, G. C.; Prato, M.; Marras, S.; Cavalli, A.; Manna, L., Cu3-XP Nano-crystals as a Material Platform for near-Infrared Plasmonics and Cation Exchange Reactions. Chem. Mater. 2015, 27, 1120-1128.

(13) Powell, A. E.; Hodges, J. M.; Schaak, R. E., Preserving Both Anion and Cation Sublattice Features During a Nanocrystal Cation-Exchange Reaction: Synthesis of Metastable Wurtzite-Type Cos and Mns. J. Am. Chem. Soc. 2016, 138, 471-474.

(14) Grodzińska, D.; Pietra, F.; van Huis, M. A.; Vanmaekelbergh, D.; de Mello Donegá, C., Thermally Induced Atomic Reconstruction of PbSe/CdSe Core/Shell Quantum Dots into PbSe/CdSe Bi-Hemisphere Hetero-Nanocrystals. J. Mater. Chem. 2011, 21, 11556-11565.

(15) Wang, X.; Liu, X.; Zhu, D.; Swihart, M. T., Controllable Conversion of Plasmonic Cu2−XS Nanoparticles to Au2s by Cation Exchange and Electron Beam Induced Transformation of Cu2−XS–Au2S Core/Shell Nanostructures. Nanoscale 2014, 6, 8852-8857.

(16) Gariano, G.; Lesnyak, V.; Brescia, R.; Bertoni, G.; Dang, Z.; Gaspari, R.; De Trizio, L.; Manna, L., Role of the Crys-tal Structure in Cation Exchange Reactions Involving Colloidal Cu2Se Nanocrystals. J. Am. Chem. Soc. 2017, 139, 9583-9590.

(17) Balcerak, R.; Gibson, J. F.; Gutierrez, W. A.; Pollard, J. H., Evolution of a New Semiconductor Product: Mercury Cadmium Telluride Focal Plane Arrays. SPIE: 1987; Vol. 26, p 191-200, 10.

(18) Yang, J.; Zhou, Y.; Zheng, S.; Liu, X.; Qiu, X.; Tang, Z.; Song, R.; He, Y.; Ahn, C. W.; Kim, J. W., Self-Reorganization of CdTe Nanoparticles into near-Infrared Hg1−XCdxTe Nanowire Networks. Chem. Mater. 2009, 21, 3177-3182.

(19) Smith, A. M.; Nie, S., Bright and Compact Alloyed Quantum Dots with Broadly Tunable near-Infrared Absorption and Fluorescence Spectra through Mercury Cation Exchange. J. Am. Chem. Soc. 2011, 133, 24-26.

(20) Rogach, A. L.; Harrison, M. T.; Kershaw, S. V.; Kor-nowski, A.; Burt, M. G.; Eychmüller, A.; Weller, H., Colloidally Prepared CdHgTe and HgTe Quantum Dots with Strong near-Infrared Luminescence. Phys. Status Solidi B 2001, 224, 153-158.

(21) Shen, G.; Guyot-Sionnest, P., HgTe/CdTe and HgSe/CdX (X = S, Se, and Te) Core/Shell Mid-Infrared Quantum Dots. Chem. Mater. 2019, 31, 286-293.

(22) Wang, H.; Lou, S.; Tang, Z.; Xu, W.; Shang, H.; Shen, H.; Li, L. S., Thiolate-Assisted Cation Exchange Reaction for the Synthesis of near-Infrared Photoluminescent HgxCd1−XTe Nano-crystals. Dalton Trans. 2012, 41, 12726-12732.

(23) Smith, A. M.; Lane, L. A.; Nie, S., Mapping the Spatial Distribution of Charge Carriers in Quantum-Confined Hetero-structures. Nat. Commun. 2014, 5, 4506.

(24) Gupta, S.; Zhovtiuk, O.; Vaneski, A.; Lin, Y.-C.; Chou, W.-C.; Kershaw, S. V.; Rogach, A. L., CdxHg(1−X)Te Alloy Colloi-dal Quantum Dots: Tuning Optical Properties from the Visible to near-Infrared by Ion Exchange. Part. Part. Syst. Charact. 2013, 30, 346-354.

(25) Szofran, F. R.; Lehoczky, S. L., The Pseudobinary HgTe-CdTe Phase Diagram. J. Electron. Mater. 1981, 10, 1131-1150.

(26) Kershaw, S. V.; Burt, M.; Harrison, M.; Rogach, A.; Weller, H.; Eychmüller, A., Colloidal CdTe/HgTe Quantum Dots with High Photoluminescence Quantum Efficiency at Room Temperature. Appl. Phys. Lett. 1999, 75, 1694-1696.

(27) Choi, D.; Yoon, B.; Kim, D.-K.; Baik, H.; Choi, J.-H.; Jeong, K. S., Major Electronic Transition Shift from Bandgap to Localized Surface Plasmon Resonance in CdxHg1–XSe Alloy Nanocrystals. Chem. Mater. 2017, 29, 8548-8554.

(28) Harrison, M. T.; Kershaw, S. V.; Burt, M. G.; Eychmüller, A.; Weller, H.; Rogach, A. L., Wet Chemical Synthesis and Spectroscopic Study of CdHgTe Nanocrystals with Strong near-Infrared Luminescence. J. Mater. Sci. Eng. B 2000, 69-70, 355-360.

(29) Izquierdo, E.; Robin, A.; Keuleyan, S.; Lequeux, N.; Lhuillier, E.; Ithurria, S., Strongly Confined HgTe 2d Nanoplate-lets as Narrow near-Infrared Emitters. J. Am. Chem. Soc. 2016, 138, 10496-10501.

(30) Gréboval, C.; Izquierdo, E.; Livache, C.; Martinez, B.; Dufour, M.; Goubet, N.; Moghaddam, N.; Qu, J.; Chu, A.; Ra-made, J.; Aubin, H.; Cruguel, H.; Silly, M.; Lhuillier, E.; Ithurria, S., Impact of Dimensionality and Confinement on the Electronic Properties of Mercury Chalcogenide Nanocrystals. Nanoscale 2019.

(31) Izquierdo, E.; Dufour, M.; Chu, A.; Livache, C.; Mar-tinez, B.; Amelot, D.; Patriarche, G.; Lequeux, N.; Lhuillier, E.; Ithurria, S., Coupled HgSe Colloidal Quantum Wells through a Tunable Barrier: A Strategy to Uncouple Optical and Transport Band Gap. Chem. Mater. 2018, 30, 4065-4072.

(32) Clayton, A. J.; Barrioz, V., Chapter 5 Thin Film Cadmium Telluride Solar Cells. In Materials Challenges: Inorganic Photovoltaic Solar Energy, The Royal Society of Chemistry: 2015; pp 135-159.

(33) Polman, A.; Knight, M.; Garnett, E. C.; Ehrler, B.; Sinke, W. C., Photovoltaic Materials: Present Efficiencies and Future Challenges. Science 2016, 352.

(34) Zhang, H.; Kurley, J. M.; Russell, J. C.; Jang, J.; Talapin, D. V., Solution-Processed, Ultrathin Solar Cells from CdCl3–-Capped CdTe Nanocrystals: The Multiple Roles of CdCl3– Ligands. J. Am. Chem. Soc. 2016, 138, 7464-7467.

(35) Crisp, R. W.; Panthani, M. G.; Rance, W. L.; Duenow, J. N.; Parilla, P. A.; Callahan, R.; Dabney, M. S.; Berry, J. J.; Ta-lapin, D. V.; Luther, J. M., Nanocrystal Grain Growth and Device Architectures for High-Efficiency CdTe Ink-Based Photovoltaics. ACS Nano 2014, 8, 9063-9072.

(36) Kagan, C. R.; Lifshitz, E.; Sargent, E. H.; Talapin, D. V., Building Devices from Colloidal Quantum Dots. Science 2016, 353.

(37) MacDonald, B. I.; Martucci, A.; Rubanov, S.; Watkins, S. E.; Mulvaney, P.; Jasieniak, J. J., Layer-by-Layer Assembly of Sintered CdSexTe1–X Nanocrystal Solar Cells. ACS Nano 2012, 6, 5995-6004.

(38) Townsend, T. K.; Heuer, W. B.; Foos, E. E.; Kowalski, E.; Yoon, W.; Tischler, J. G., Safer Salts for CdTe Nanocrystal Solution Processed Solar Cells: The Dual Roles of Ligand Exchange and Grain Growth. J. Mater. Chem. A 2015, 3, 13057-13065.

(39) Panthani, M. G.; Kurley, J. M.; Crisp, R. W.; Dietz, T. C.; Ezzyat, T.; Luther, J. M.; Talapin, D. V., High Efficiency Solution Processed Sintered CdTe Nanocrystal Solar Cells: The Role of Interfaces. Nano Lett. 2014, 14, 670-675.

(40) Chen, H.-Y.; Lo, M. K. F.; Yang, G.; Monbouquette, H. G.; Yang, Y., Nanoparticle-Assisted High Photoconductive Gain in Composites of Polymer and Fullerene. Nat. Nanotechnol. 2008, 3, 543-547.

(41) Tu, C.-C.; Lin, L. Y., High Efficiency Photodetectors Fabricated by Electrostatic Layer-by-Layer Self-Assembly of CdTe Quantum Dots. Appl. Phys. Lett. 2008, 93, 163107.

(42) Zhang, Y.; Hellebusch, D. J.; Bronstein, N. D.; Ko, C.; Ogletree, D. F.; Salmeron, M.; Alivisatos, A. P., Ultrasensitive Photodetectors Exploiting Electrostatic Trapping and Percolation Transport. Nat. Commun. 2016, 7, 11924.

(43) Shen, T.; Li, B.; Zheng, K.; Pullerits, T.; Cao, G.; Tian, J., Surface Engineering of Quantum Dots for Remarkably High Detectivity Photodetectors. J. Phys. Chem. Lett. 2018, 9, 3285-3294.

(44) Miszta, K.; Gariano, G.; Brescia, R.; Marras, S.; De Donato, F.; Ghosh, S.; De Trizio, L.; Manna, L., Selective Cation Exchange in the Core Region of Cu2–XSe/Cu2–XS Core/Shell Nanocrystals. J. Am. Chem. Soc. 2015, 137, 12195-12198.

(45) Taniguchi, S.; Green, M.; Lim, T., The Room-Temperature Synthesis of Anisotropic CdHgTe Quantum Dot Alloys: A “Molecular Welding” Effect. J. Am. Chem. Soc. 2011, 133, 3328-3331.

(46) Ringel, S. A.; Smith, A. W.; MacDougal, M. H.; Rohatgi, A., The Effects of CdCl2 on the Electronic Properties of Molecular-Beam Epitaxially Grown CdTe/CdS Heterojunction Solar Cells. J. Appl. Phys. 1991, 70, 881-889.

(47) Major, J. D.; Treharne, R. E.; Phillips, L. J.; Durose, K., A Low-Cost Non-Toxic Post-Growth Activation Step for CdTe Solar Cells. Nature 2014, 511, 334.

(48) Maniscalco, B.; Abbas, A.; Bowers, J. W.; Kaminski, P. M.; Bass, K.; West, G.; Walls, J. M., The Activation of Thin Film CdTe Solar Cells Using Alternative Chlorine Containing Compounds. Thin Solid Films 2015, 582, 115-119.

(49) Dharmadasa, I. M.; Echendu, O. K.; Fauzi, F.; Abdul-Manaf, N. A.; Olusola, O. I.; Salim, H. I.; Madugu, M. L.; Ojo, A. A., Improvement of Composition of CdTe Thin Films During Heat Treatment in the Presence of CdCl2. J. Mater. Sci.: Mater. Electron. 2017, 28, 2343-2352.

(50) Atzmüller, R.; Rösch, M.; Schaack, G.; Becker, C. R., Quantum Confinement Effects above the Fundamental Band Gap in HgTe/Hg0.3Cd0.7Te Heterostructures Studied by Resonant Raman Scattering near the E1 Edge. Phys. Rev. B 1996, 54, 16907-16918.

(51) Ren, A.; Liu, C.; Gao, W.; Wang, F.; Liu, Y.; Wu, L.; Wang, W.; Li, W.; Zhang, J.; Feng, L., Characterization and An-nealing of CdTe Thin Film Prepared by Vapor Transport Deposition. Chalcogenide Lett. 2015, 12, 555-567.

(52) Taylor, G. W.; Simmons, J. G., Photoconductivity Characteristics of Defect Insulators. J. Phys. C: Solid State Phys. 1975, 8, 3360-3370.

Chapter 5: In(Zn,Yb)P Near Infra-Red Luminescent quantum dots

Abstract

The main aim of this work was to develop a synthesis method to incorporate lanthanide ions into InP quantum dots and to demonstrate energy transfer from the InP host to the lanthanide dopant. For this purpose, the Yb^{3+}ions were chosen because of its luminescent efficiency is close to 100%. Recently, rare earth ions doped materials, have attracted a great interest for photovoltaic applications to improve solar cell efficiency which is limited by the mismatch between the incident solar spectrum and the spectral response of the solar cells. These latter cannot convert all the high energy wavelength photons in the UV window. This limit can be overcome by a quantum cutting, or down converting, elements like a lanthanide able to convert one photon of high energy into photons of lower energy. Before to investigate the doping technique, the synthesis of the InP NCs was analyzed and optimized.

The incorporation of the lanthanide ion is investigated by changing the Yb:In molar and by employing a hot- injection method to synthetized InP and In(Zn)P colloidal semiconductors. To incorporate the Yb^{3+} dopant ions, the role of the length of the ligand used during the doping was also explored. As an alternative doping method, a one pot synthesis route to dope InP or In(Zn)P NCs was utilized.

After the study of the doping process, the possibility of growing ZnS monolayers around the NCs and the existence of the dopant emission was finally investigated.

5.1 Indium Phosphide: tunable, bright, and narrow band luminescence

In the previous sections, partial cation exchange studies related to the II-VI semiconductor NCs have been reported. Nonetheless, as discussed in the toxicity section Paragraph, the composition of new generations of NCs is moving toward In, as a result of the covalent nature of its crystal lattice [1, 2] or Cu/In rather than Cd. This chapter is therefore intended to illustrate the effects of the cation exchange for NIR emission on InP template. Bulk InP has a wide direct Band Gap of 1.35 eV (918nm) and a widespread emission tunable from green to NIR with increasing particle size. Moreover, type III-V semiconductors exhibit superior electronic and optoelectronic properties in comparison to other semiconductors. In contrast, studies of colloidal III-V semiconductor NCs are less advanced in comparison to II-VI because their synthetic chemistry is challenging. The reasons are directly associated to their (more) covalent character, compared to II-VI. The chemistry involves the use of precursors of higher reactivity and higher reaction

temperatures than in the case of metal chalcogenide NCs. These constraints typically make it difficult to create conditions for reaction that yield monodispersal NCs which would lead to a narrow emission profile and increase the color purity. A robust control of the particle size must be achieved. The recent mechanistic studies have shown that organometallic phosphorous precursor reactivity is the main reason of the problems found in the size distribution of InP NCs. Numerous methodologies have been attempted to enhance these aspects. In this thesis, we report the effect of the variation of molar concentration in reaction mixture, the use of two different phosphorous precursors, and alloyed In_xZn_yP NCs. The current main drawback of as-synthetized InP nanocrystals is related to the low photoluminescence QYs of less than 1% that is due to a limited control of the synthesis routes. However, it can be largely boosted with the growth of an overcoating shell material with a higher band gap which helps in passivating the surface defects characterizing the InP NCs surface and providing an effective method for improving the QYs. [3,4,5]

Thus, we developed a shell coating method to obtain InP@ZnS core@shell NCs with high QY studying different sulphur source precursors.

5.2 Lanthanides

Trivalent lanthanides, Ln^{3+}, are ions with a partially filled f-orbital. Together with chemically similar elements, scandium and yttrium are referred to as rare earth elements [6].

It is important to emphasize that the PL is environmentally stable since the 4f orbitals are well shielded from the surroundings by the outer filled $5s^2$ and $5p^6$ closed shells[7,8]. The occupation of the f-shell changes but, as mentioned, the f-electrons do not interact (significantly) with the other ions and do not form bonds, thus the series of lanthanides is chemically very similar. The most noticeable chemical difference between the lanthanides is the decrease ionic radius over the series. This is known as the lanthanide contraction and is explained by the increase in nuclear charge. The 5s and 5p electrons are poorly shielded by the 4f electrons, so with increasing nuclear charge the extension 5s and 5p orbitals decreases [9].

Although Ln^{3+} are chemically very similar, they are largely studied because of their unique f-f transitions that are independent from the host materials (as opposed to d-d transitions in transition metals). For a Ln^{3+} ion with configuration [Xe] $4f^n$, there are $\binom{14}{n}$ different electron distributions over the 4f shell. [10] [11] [12]

This means multiple energy levels within the shell, as reported in the diagram in Fig.5.1, published the group of Dieke based on their spectroscopic and theoretical works [8]. The different energy levels in the Dieke's diagram are denoted by two quantum numbers S and L while a spectroscopic level is additionally characterized by a third quantum number, J and a partial energy level diagram is given. The value for J in the ground state is L - S for $n < 7$ and L + S for $n \geq 7$.

As a consequence, the f-f transition produces fine line emission bands with a very small Stokes shift. This also has the effect that crystal field splitting (indicated in the Dieke diagram by the width of a state) is minimal.

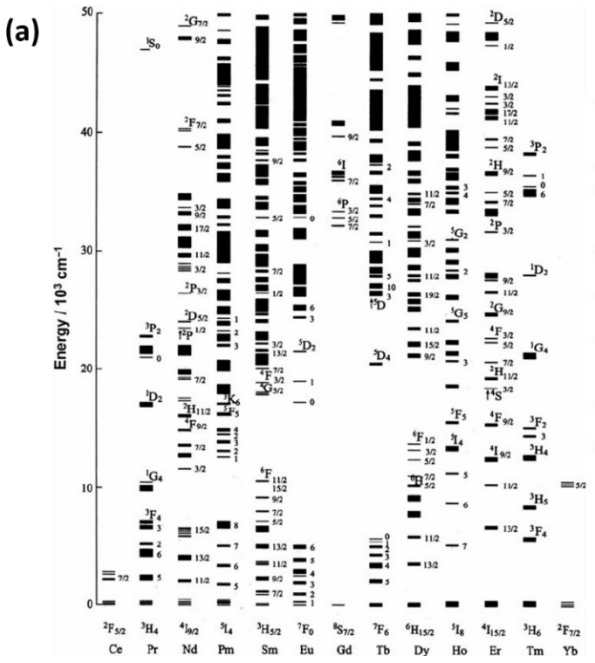

(b)

Symmetry	Site symmetry	integer J								
		0	1	2	3	4	5	6	7	8
Cubic	T, T_d, T_h, O, O_h	1	1	2	3	4	4	6	6	7
Hexagonal	C_{3h}, D_{3h}, C_6, C_{6h}, C_{6v}, D_6, D_{6h}	1	2	3	5	6	7	9	10	11
Trigonal	C_3, S_6 C_{3v}, D_3, D_{3d}									
Tetragonal	C_4, S_4, C_{4h}, C_{4v}, D_4, D_{2d}, D_{4h}	1	2	4	5	7	8	10	11	13
Low	C_1, C_s, C_2, C_{2h}, C_{2v}, D_2, D_{2h}	1	3	5	7	9	11	13	15	17
Symmetry	Site symmetry	half-integer J								
		1/2	3/2	5/2	7/2	9/2	11/2	13/2	15/2	17/2
Cubic	T, T_d, T_h, O, O_h	1	1	2	3	3	4	5	6	6
All others[a]	see above	1	2	3	4	5	6	7	8	9

[a] All sublevels are doubly degenerate (Kramer's doublets)

Figure 5.1 (a) The 4f energy levels of the lanthanide series. The broadening of a level indicates its crystal field splitting. Reproduces form ref.16. (b) Number of ligand-field sublevels versus site symmetry and the value of the J quantum number

In the case of Yb $^{3+}$, with an electronic configuration [Xe] 4f ^{13} , the distribution of its 13 electrons over the seven 4f sub-orbitals and applying the Hund's ruels yiels the maximum S of 1/2 (7 × 1/2 + 6 × -1/2) and the maximum L of +3 (2 × 3 + 2 × 2 + 2 × 1 + 2 × 0 - 2 × 1 - 2 × 2 - 3), corresponding with F. Since 13 > 7, J = L + S = 7/2. The ground state term symbol then becomes $^2F_{7/2}$ while the first excited state corresponds with a change in angular momentum and is $^2F_{5/2}$ (see

2) resulting in very sharp photoluminescence (PL) emission[13].

The parity selection rule implies that the 4f-4f forbidden are forbidden resulting in materials with a low molar excitation coefficient absorbing light weakly. As a result of the forbidden parity, the f-f transition usually has long excited state lifetime, on millisecond-order basis.

In the next paragraph, we report some aspects of the peculiarity connected to energy transfer in lanthanides lying behind the choice of InP as host semiconductor (SC).

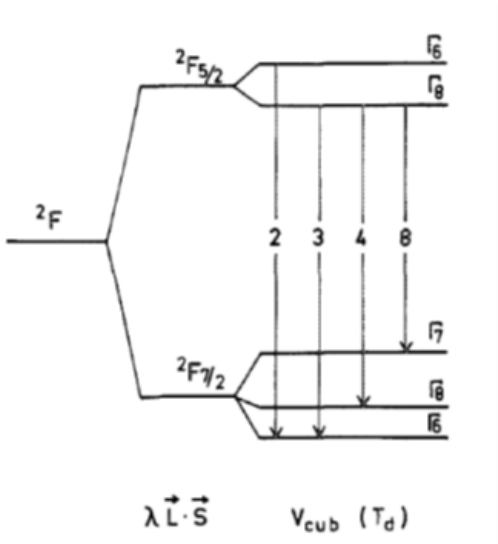

Figure 5.2 Energy-level scheme for Yb3+. λ L ⃗S ⃗ is the spin-orbit splitting energy for the free ion in the order of 10000 cm-1 (1.24eV). The free ion spin orbit states 2F5/2 - 2F7/2 are additionally split by the cubic crystalline field (Td), into crystal field states Γ6, Γ8 (J=5/2) and Γ6, Γ7, Γ8 (J=7/2). Since the 4f electrons are screened by the outer 5s2 5p6 orbitals, they are weakly affected by the crystalline environment, and the crystal splitting of the spin-orbit levels is small in contrast to the spin-orbit splitting.[4]

5.2.1 Energy transfer from host semiconductor to Yb $^{3+}$

In order to observe Yb^{3+} dopant emission upon excitation of its quantum dot host, energy transfer from quantum dot in its excited state to the dopant have to occur.

The simplest energy transfer mechanism is a single step process where the excited QD directly transfer its energy to the Yb^{3+} ion. However, the energy difference between the host QD's band gap (the emission energy of the InP NCs) and the Yb^{3+}'s excitation energy (the difference between the $^2F_{5/2}$ excited state and the $^2F_{7/2}$ ground state) is on the order of 7000 cm^{-1}. Thus, this energy transfer would require phonon assistance. However, the lattice vibration energy of the InP quantum dot host material is approximatively 300 cm^{-1} [14]. This is below the required energy for the sensitization the Yb^{3+} ion. Therefore, a direct energy transfer assisted by phonons is unlikely.

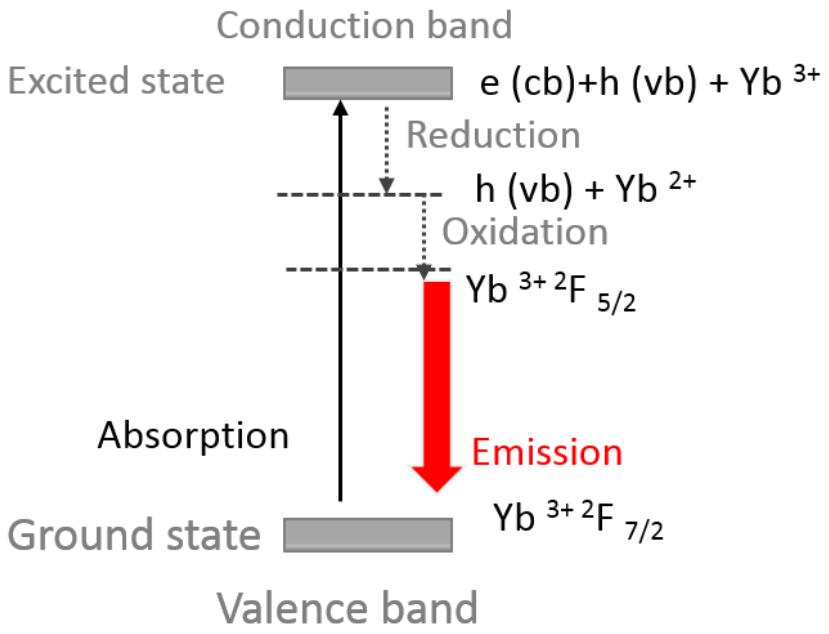

Figure 5.3 Sketch representing the proposed two step energy transfer mechanism from Eiler and De Mello Donega. The Yb ion is reduced by the electron from the conduction band of the excited NCs and subsequently oxidized by the hole in the valence band. The Yb 3+ ion is left excited in 2F 5/2 state from which it can return to the 2F7/2 ground state giving rise to the characteristic Yb 3+ emissions at 985 and 1030 nm.

An alternative mechanism, proposed by De Mello Donega's group[15], involves a two-step energy transfer process in which the first part of the energy is transferred to Yb^{3+} from one electron in conduction band of the excited host NCs. The second energy transfer step consists in capturing the hole left in the valence band and reducing the ion to Yb^{3+} in $^2F_{5/2}$ excited state. A schematic representation of this energy transfer mechanism is shown in Figure 5.3[11].

5.2.2 Energy transfer via co-doping for Down-conversion

An additional option to achieve an energy transfer from host InP to the guest Yb^{3+} pass through a co-doping method which is also a two-steps energy transfer mechanism (schematic representation is reported in Figure 5.). Basically, the energy transfer from one rare earth, as Eu^{3+}, to Yb is a cooperative process in which the excited electron from the $^5D_0$ level of Eu^{3+} relaxes to $^2F_{5/2}$ levels of two Yb^{3+} ions.

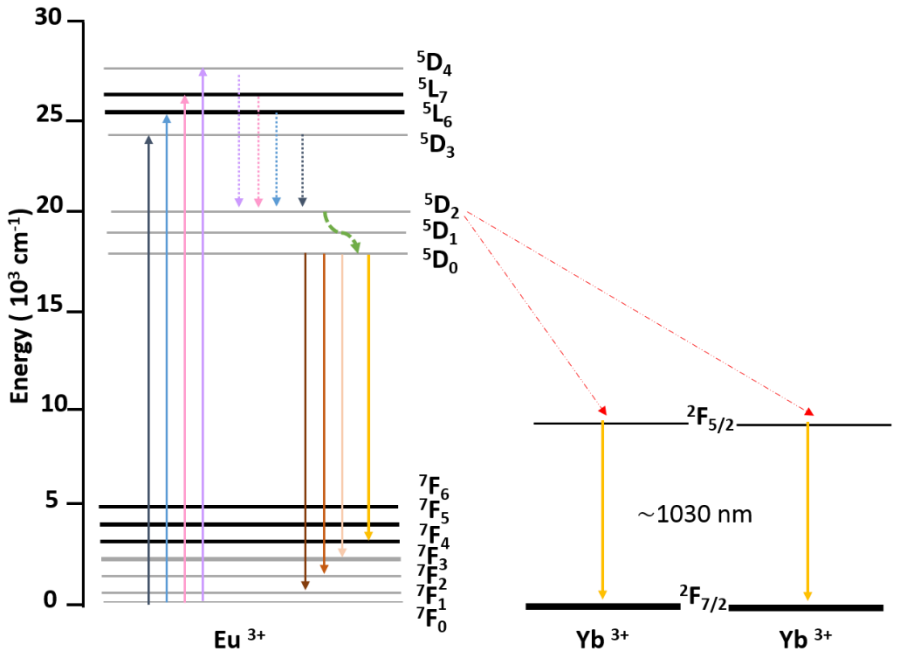

Figure 5.4. Schematic the energy level diagram of Eu^{3+} /Yb^{3+} co-doped NCs illustrating the energy transfer mechanism from $^5D_0$ level of Eu^{3+} to $^2F_{5/2}$ levels of Yb^{3+}. The solid arrows denote the excitation and the emission processes. The dashed and dotted arrows represent non- radiative transition or energy transfer.

A similar mechanism has been recently studied in Tb^{3+}-Yb^{3+} couple [16]to boost the efficiency of the spectral conversion of the solar spectrum. In principle, over 60% of the energy losses in a solar cell are due to the spectral mismatch: low energy photons are no absorbed (transmission losses) and absorption of high-energy photons is followed by a rapid relaxation of hot charge carriers to the band edges of the semiconductor (thermalization losses).[17] Lanthanide ions are suitable candidates for efficient spectral conversion. During the last decade the research focused on the up-conversion with lanthanides. While the down conversion consists in one photon at high energy that excites two lanthanides ion with a consequent generation of two lower energy photons. Compared to up-conversion studies, the down-conversion is still limited.

In this chapter, we discuss the use of InP as host material in NCs synthesis. Its bandgap is wide enough to allow a good energy transfer probability from the host SC to the RE ions so enabling light emission in the NIR window.[18]

5.3 Experimental Methods

In order to achieve the Yb-doping of InP, different synthetic routes have been followed, and all of them were carried out under Argon using Schlenk line setup.

5.3.1 InP synthesis via Hot Injection

The hot-injection method for the preparation of InP NCs is adapted from the method developed by Xie and Woo-Seuk Song at el.[5] It consists of injecting Phosphorous precursor in the hot reaction mixture, containing the Indium and Zinc precursors and coordinating ligands, as Oleylamine (OAm), in a non-coordinating solvent, as Octadecene (ODE). This entails the thermal decomposition of the precursors that react to form a monomer followed by the nucleation and growth of the QDs.

Different phosphorous sources were studied. The phosphorous precursor was prepared by mixing:

-tris(diethylamino)phosphine TDEP with 1 ml of ODE. •Different P: In feeding molar ratio were studied. The aminophosphines are excellent precursors for synthesizing InP NCs, but they are not the most obvious. In TDEP, the phosphorus atom has an oxidation state of +3, rendering a reaction with an In(III) precursor such as indium chloride or indium acetate not direct. Aminophosphines require some intermediate reduction steps to form InP. Tessier *et al.* [19]proposed a transamination mechanism that explains the P oxidation state conversion. In order to lead the full conversion of P+3 to -3,the ratio between the aminophosphines and the P source has to be>3.5. Thus, we used 0.06 mmol of TDEP. Moreover 0.2 mmol of tris(trimethylsilyl)phosphine $P(TMS)_3$ and 1 ml of ODE were used. Everything was mixed in a glovebox under a nitrogen atmosphere.

- **InP NCs**. In a typical synthesis, the indium precursor was prepared by mixing 0.23 mmol of indium (III) chloride $InCl_3$ and 1.1 mmol of zinc chloride $ZnCl_2$, 7.5 mmol of OAm and 2.5 mmol ODE. The mixture was degassed for 1h at 120°C under vacuum and then quickly heated at 180°C under Ar flow. Once 180°C is reached, the phosphorous precursor was rapidly injected to the above mixture, and the growth of the InP core QDs proceeded for 30 min and quenched with compressed air and diluted in toluene. During the reaction, aliquots were taken at different reaction times and collected in toluene to follow the growth of the NCs by absorption spectroscopy. The final product of the synthesis was purified by 3 cycles of

precipitation with a non-solvent mixture, and by centrifugation for 10 min at 3200 rpm. The purifies InP NCs were dispersed in a small amount of toluene and stored in glovebox.

Although Zn reduces the size dispersion and facilitate the subsequent shell growth, its concentration was studied in order to understand its influence of the Yb dopant incorporation.

Moreover, ytterbium oleate and ytterbium myristate was studied as ytterbium precursors for the doping of InP with Yb^{3+} ions:

-the ytterbium oleate $Yb(OA)_3$ stock solution proceeded as follow: in a flask 4 mmol Yb(Ac)3·(H2O)4 was weighted and 12 mL oleic acid and 10 mL ODE were mixed. The mixture was brought under vacuum using a Schlenk-line and heated to 80°C while stirring. After 30 minutes, the temperature was raised to 150 ◦C and the reaction was performed for 2 hours before cooling to room temperature. 2 mL ODE was added to decrease the viscosity yielding a 0.2 M $Yb(OA)_3$ solution.

-the ytterbium myristate stock solution: a similar procedure was used replacing the myrisitc acid to oleic acid

- **Yb incorporation by cation exchange reaction on InP NCs.**

We adopted two approaches for the Yb^{3+} incorporation in the InP NCs system: a partial cation exchange on InP core and the diffusion growth mechanism. The first approach was carried on after the InP growth: the temperature was raised at 230°C and then the Yb precursor in 0.5 ml of ODE corresponding with a varying Yb:In ratio (from 0.1 to 0.3) was added in a slow dropwise way.

- **Yb incorporation by diffusion growth in one pot synthesis of InP:Yb NCs.**

Indium and ytterbium precursors were put in the same flask all at once from the beginning varying the Yb:In molar ratio from 0.1 to 0.3. The reaction mixture was degassed for 1 h and then the temperature was raised at 180°C for the phosphorous injection.

- **ZnS shell growth**

ZnS shells were grown on doped InP NCs according to a procedure reported by Song et al. [5]. In particular, the InP doped NCs as synthetized were heated to 200 ◦C while stirring and a mixture of 0.01 mmol Zinc stearate and 0.05 mmol of sulfur dispersed in TOP (2M) diluted in 0.5 ml of ODE were added slowly drop by drop in the flask. The temperature was kept for 300 minutes to allow the growth of the shell before cooling the mixture to room temperature. After

cooling, the particles were sedimented by addition of toluene and ethanol, centrifuged, and redispersed in toluene.

- **Di(trimethylsylil)sulfide, D(TMS)S.**

An alternative path to grow ZnS on doped InP NCs, a more reactive S precursor in combination with shorter reaction time was used. The doped InP mixture was heated at 200°C and a 0.1M D(TMS)S was substituted to TOP-S. The reaction was kept 30 minutes before cooling down and washed with ethanol and redispersed in toluene.

5.4 Results and discussion

5.4.1 Structural and optical characterization

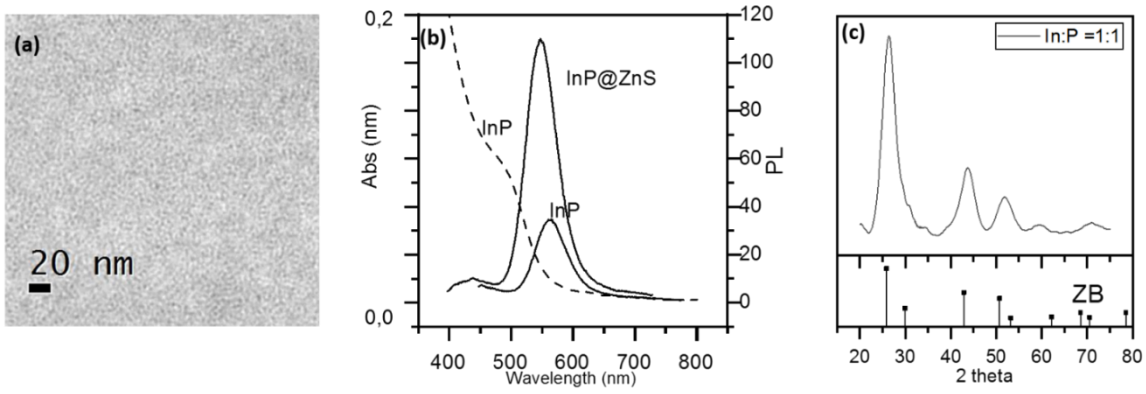

Figure 5.5 (a) typical TEM image of an InP Ncs sample of a size ranging from 2 to 5 nm. (b) absorption spectrum (dotted line) of a bare InP NCs in toluene. The first exciton peak corresponding to $S_h \rightarrow S_e$ transition is identified around 500 nm. The two continuous line correspond to the PL emission spectra of zinc-less InP NCs (less intense peak) and of InP coated by ZnS shell (more intense peak),respectively. The increased intensity indicates the surface passivation. (c) x-ray diffraction pattern of zinc blend InP as synthetized. ICSD reference code: 640192.

As first step InP NCs were synthetized. As detailed described in the method section, initially Zinc was used to facilitate the further growth of ZnS shell. Finally, we decided to avoid it be caused it can inhibit the incorporation of Yb^{3+} in a competitive way. Regarding the P precursors, the most optimized is the $(TMS)_3P$ and phosphines which give the best results in terms of size dispersion. Unfortunately, they are expensive, pyrophilic with the air and produce phosphine that is a very toxic gas. A few years ago, Song et al.[20] used an aminophosphine as precursor, being much cheaper and acting both as solvent and as ligand. Moreover, it has been

proven that it plays a double role not only as P precursor, but also as reducing agent in presence of a primary ammine: P starts with an oxidation state of +3 and finish with an oxidation state of -3 through a transamination reaction with Oleylamine.[21]. For these reasons, we based our study on the latter P precursor. Figure 5.5 shows a typical TEM image of InP NCs with a diameter ranging from 2-5 nm. The elemental analysis, conducted via ICP-OES, revealed that the composition of the NCs was nearly stoichiometric (i.e. InP) and the XRD characterization indicated the presence of a ZB InP structure (ICSD number 640192). The contrast between the NCs and the background is very low, and this is typical of these kinds of systems due to the high amount of electrons transmitted by InP. The bare InP presents a shoulder in the absorption spectra corresponding to the first exciton peak of the $S_h \rightarrow S_e$ transition at 500 nm. Using this absorption wavelength, the average size of the InP NCs can be derived using an empirical formula derived by the group of Xie *et al*. [22] [23], which gives an InP average size of 4 nm.

$$D = -3.7707 * 10^{-12}\,\lambda^5 + 1.0262 * 10^{-8}\,\lambda^4 - 1.0781 * 10^{-5}\,\lambda^3 + 5.4550 * 10^{-3}\,\lambda^2 - 1.3122\,\lambda + 119.9$$

The bare InP display a very low emission upon excitation at 400 nm. This is due to dangling bond of the unbound phosphor atoms on the surface of the InP acting as trap states which capture the excited electron promoted by the absorbed light causing it to decay non-radiatively via multiple trap states.

These problems may be overcome by the growth of a ZnS type I shell. The shell is growth as described in the method section. The shelled InP were measured by emission spectroscopy measurement and a comparison before and after shell growth is showed in Figure 5.6 upon and excitation at 400 nm. The increasing of the intensity of the emission peaks denotes that the ZnS shell passivate the dangling bonds, decrease the number of trap states in the band gap and increase the probability of radiative decay. Upon the shell growth, a small blue shift can be observed. A possible explanation for this shift is the effective decrease in InP core size by a Zn to In substitution

5.4.2 Incorporation of Yb in InP by Partial Cation exchange

The synthetized InP NCs were used as cores in doping experiments. InP were exposed to different Yb^{3+}/ In^{3+} feed molar ratios, ranging from 0.1 (10%) to 0.3 (30%) employing $Yb(OA)_3$ solution as Yb precursors, dissolved in ODE. The incorporation of the dopant was performed

for 30 minutes before quenching the reaction. ICP, absorption, emission spectroscopy and XRD were performed on the obtained products. The ICP elemental analysis indicated that the extent of the substitution In^{3+} by Yb $^{3+}$ was not in line with the Yb $^{3+}$/In^{3+} feed molar ratio employed (see table in Figure *5*.5.6). Accordingly, to XRD analyses, an increase in the Yb $^{3+}$ content inside the NCs does not affect the crystal structure and no side phases are detected. Representative absorption spectra obtained from bare InP NCs (black) and doped InP are compared in Figure *5*.5.6 and it reveals a re-shift and a less defined shoulder. These features may be due to a leakage of the exciton wave-function as a decreased quantum confinement. This is probably due to a deposition of the dopant on the outer layer of the InP, causing a decreasing of the confinement of the wave-function.

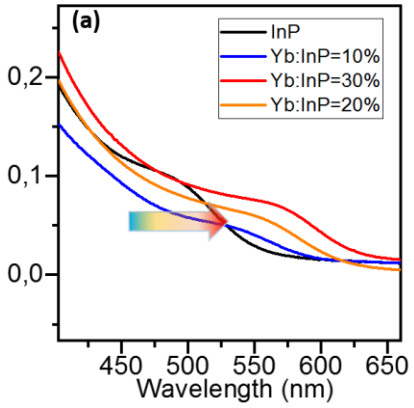

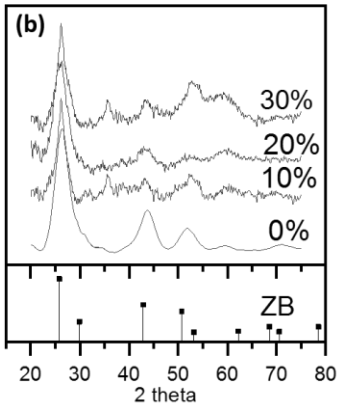

(c)

sample	First exc. Peak λ (nm)	Yb:In mol. ratio introd. (%)	Final Yb:In mol.ratio (%)
InP	495	///	
Yb:InP=10%	510	10	2.1
Yb:InP=20%	527	20	3.8
Yb:InP=30%	550	30	4.7

Figure 5.6. **(a)** Comparative absorption spectra of bare InP NCs (black) and InP doped with Yb $^{3+}$ in increasing amounts. Respectively curves correspond to: **(b)** x-ray diffraction pattern of zinc blend InP as synthetized. ICSD reference code: 640192. (c) ICP-OES elemental analysis on doped InP with various feed molar ratios.

Photoluminescence (PL) measurements at room temperature were performed with a wavelength of excitation of 355 nm. PL did not show any Yb^{3+} typical emission lines in the region of interest between 950 and 1050 nm, where the $^2F_{5/2} \rightarrow {}^2F_{7/2}$ transition is expected to correspond as predicted by the Dieke diagram (Fig. 5.1). The spectrum displays only noise. This suggests that no energy transfer from dot to dopant occurs and that no Yb^{3+} ions adhere to the InP core. Moreover, this suggests that it might depends on other competitive relaxation pathways, like the possible formation of trap-states caused by the dopant ions (Yb^{3+} ions) coupled to vibrations of the ligands and molecules in the solutions (resulting in a multi-phonon relaxation). This could be possible if the Yb^{3+} ions reside only at the surface of the InP NCs, instead of being incorporated in the crystal lattice. To investigate whether the incorporation of the Yb^{3+} could

be improve, a series of experiments was performed varying the Yb^{3+} precursor, its feed molar ratio with respect to In^{3+}, and the way it is introduced in the reaction mixture. Among the precursors investigated, we played with the monomer reactivity and their depletion rate.

5.4.3 One-pot synthesis: diffuse regime

To improve the amount of Yb incorporated in InP NCs we used another approach: we introduced the Yb^{3+} precursor in the flask together with In^{3+} precursor, OLAm and ODE. We explored different molar ratio ranging from 0.1 (10%) to 0.3 (30%) employing $Yb(OA)_3$ solution as Yb precursor. In this case, the ICP elemental analysis indicated that the extent of the substitution In^{3+} by Yb^{3+} was in line with the Yb^{3+}/In^{3+} feed molar ratio employed (see table in Figure 5.7).

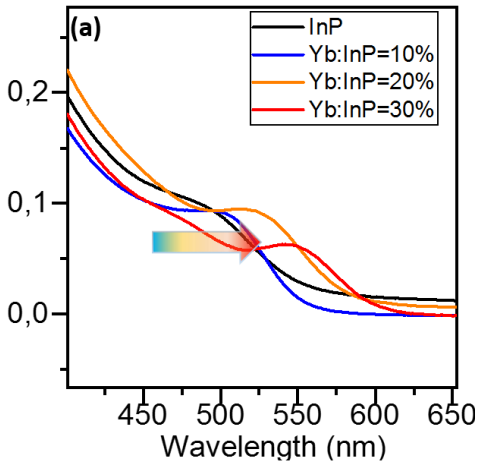

(b)

sample	First exc. Peak λ (nm) (nm)	Yb:In mol.ratio Introd. (%)	Final Yb:In mol.ratio (%)
InP	495	///	
Yb:InP=10%	540	10	9
Yb:InP=20%	560	20	17
Yb:InP=30%	570	30	26

Figure 5.7 (a) Comparative absorption spectra of bare InP NCs (black) and InP doped with Yb^{3+} in increasing amounts. Respectively curves correspond to: **(b)**ICP-OES elemental analysis on doped InP with various feed molar ratios.

While ICP suggests that the incorporation of Yb^{3+} is more successful with this method, the related absorption spectra redshifts are higher, indicating that Yb^{3+} ions have not been entered in InP crystal in this case either. Another indication of this comes from the absence of the Yb^{3+} emission at 975 nm in IR window. These results suggest that this could be a possible effect of a dopant lattice ejection during the growth in a self-purification process and the dopant is restricted onto the surface. Then, the excited surface confined Yb^{3+} ions would participate to a multi-phonon relaxation by coupling ligand vibrations, leading to non-radiative decay. This indicates that at the temperature used for these reactions the InP NCs will form an energetically

more favorable lattice than the doped InP expelling Yb^{3+} ions. Thus, one possibility is to encapsulate Yb^{3+} ions with S shell, as we did for the bare InP. Alternatively, the Yb^{3+} ions effectively entered the InP NCs, but the difference between the bandgap energy of the host NCs and the energy level of the dopant is too large to allow the excited state of a dot to decay and excite the Yb^{3+} ion. To overcome to this possibility, a co-doping system can be used, as described in the introduction of this chapter.

5.5 Conclusions and future work

In this chapter, we have shown a successful method to embed the Yb^{3+} ion in InP NCs via cation exchange and growth doping procedure. As mentioned at the beginning, the Yb^{3+} is suitable both as an acceptor and as an emitter due to its luminescent quantum efficiency close to 100% and its excited level energy (∼1.2 eV) which is roughly in accordance with the band gap of Si (∼1.1 eV). However, a sensitizer is often required to enforce the energy transfer mechanism to Yb^{3+} when NCs systems are used as hosts. This study was conducted in two steps: i) we investigated the procedure for incorporating the Yb^{3+} into InP systems by means of a cation exchange process; ii) we attempted to sensitize its emission. The doping effect was evaluated by absorption, photoluminescence (PL) and elemental analysis (ICP-OES). Our aim was to demonstrate the possibility of Yb^{3+} incorporation and its effectiveness of doping has been verified by elementary analyzes. Unfortunately, no emissions corresponding to the Yb^{3+} $^2F_{5/2} \rightarrow {}^2F_{7/2}$ transition wavelength have been detected after the excitation. An option may be the energy transfer from the excited state of the NCs to the dopant ion. This could be so large to need a sensitizer acting as a bridge among the two systems. A possible candidate is Eu^{3+}sensitizer, Tb^{3+}–Yb^{3+} [24,25], Pr^{3+}–Yb^{3+} [17,26], and Tm^{3+}–Yb^{3+} [27] systems. At the moment, we obtained only preliminary results and further measurements need to be performed for a more deep understanding. Therefore, it remains unclear if the Yb^{3+} ions reside at the nanocrystal surface in a sort of core@shell structure resulting in an excited state reduced by multi-phonon relaxation. For this purpose, an electron dispersive scattering (EDX) mapping can be employed. Then, a luminescent quantum yield calculation may provide insight of the efficiency of the energy transfer from the excited state of InP to the Yb^{3+} ions after excitation by means of an integrating sphere. This research can be applied to other lanthanide ions, and similar doping methods may be used thanks to the chemical similarity of the lanthanide group. Finally, various

NCs material can be studied like copper indium sulfide (CIS), which is attractive for its low toxicity compared to Cd-based NCs and Pb-based Perovskites NCs, and also for its size-tunable absorption in the visible region as shown in the following chapter.

REFERENCES

1. Altamirano-Lozano, M. *et al.* Cobalt in hard metals and cobalt sulfate, gallium arsenide, indium phosphide and vanadium pentoxide. *IARC Monogr. Eval. Carcinog. Risks to Humans* **86**, (2006).
2. Glassy, B. A. & Cossairt, B. M. Ternary synthesis of colloidal Zn3P2 quantum dots. *Chem. Commun.* **51**, 5283–5286 (2015).
3. Panthani, M. G. *et al.* SI High efficiency solution processed sintered CdTe nanocrystal solar cells: The role of interfaces. *Nano Lett.* **1**, 1–9 (2014).
4. Adam, S. *et al.* The effect of nanocrystal surface structure on the luminescence properties: Photoemission study of HF-etched InP nanocrystals. *J. Chem. Phys.* **123**, (2005).
5. Song, W. S. *et al.* Amine-derived synthetic approach to color-tunable InP/ZnS quantum dots with high fluorescent qualities. *J. Nanoparticle Res.* **15**, (2013).
6. Talapin, D. V. Experimental and theoretical studies on the formation of highly luminescent II-VI , III-V and core-shell semiconductor nanocrystals Doctor of Natural Sciences. (2002).
7. Talapin, D. V. *et al.* Etching of colloidal InP nanocrystals with fluorides: Photochemical nature of the process resulting in high photoluminescence efficiency. *J. Phys. Chem. B* **106**, 12659–12663 (2002).
8. Auzel, F., Jean-Louis, A. M. & Toudic, Y. Oscillator strengths, quantum efficiencies, and laser cross sections of Yb3+ and Er3+ in III-V compounds. *J. Appl. Phys.* **66**, 3952–3955 (1989).
9. Tsujii, N., Imanaka, Y., Takamasu, T., Kitazawa, H. & Kido, G. Photoluminescence of Yb3+-doped CuInS2 single crystals prepared by In-flux and chemical vapor transport methods. *J. Alloys Compd.* **408**–**412**, 791–795 (2006).
10. *Advances in Spectroscopy for Lasers and Sensing*. *Advances in Spectroscopy for Lasers and Sensing* (2006). doi:10.1007/1-4020-4789-4.
11. Paufler, P. K. A. Gschneidner, Jr., L. Eyring (eds.). Handbook on the Physics and Chemistry of Rare Earths, Vol. 16. North–Holland, Amsterdam 1993. 589 S. Preis US £ 309.50/Dfl. 420.75. ISBN 0–444–89782–8. *Cryst. Res. Technol.* **30**, 926–926 (1995).
12. Goodwin, D. W. Optical Spectra of Transparent Rare Earth Compounds. *Phys. Bull.* **30**, 525–525 (1979).
13. Barnes, C. Inorganic Chemistry (Housecroft, Catherine E.; Sharpe, Alan G.). *J. Chem. Educ.* **80**, 747 (2003).
14. Goodwin, D. W. Spectra and Energy Levels of Rare Earth Ions in Crystals. *Phys. Bull.* **20**, 525–525 (1969).
15. Andreev, T. *et al.* Optical study of excitation and deexcitation of Tm in GaN quantum dots. *Phys. Rev. B - Condens. Matter Mater. Phys.* **74**, 3–8 (2006).
16. Levinshten, M. E., Rumyantsev, S. L. & Shur, M. *Handbook Series on Semiconductor Parameters,Volume 1: Si, Ge, C (Diamond), GaAs, GaP, GaSb, InAs, InP, InSb*. *1* vol. 1 (1996).
17. Vergeer, P. *et al.* Quantum cutting by cooperative energy transfer in YbxY1−xPO4:Tb3+. *Physical Review B* vol. 71 (2005).
18. Shockley, W. & Queisser, H. J. Detailed Balance Limit of Efficiency of p-n Junction Solar Cells. *J. Appl. Phys.* **32**, 510–519 (1961).

19. Tessier, M. D. *et al.* Aminophosphines: A double role in the synthesis of colloidal indium phosphide quantum dots. *J. Am. Chem. Soc.* **138**, 5923–5929 (2016).

20. Tessier, M. D. *et al.* Aminophosphines: A double role in the synthesis of colloidal indium phosphide quantum dots. *J. Am. Chem. Soc.* **138**, 5923–5929 (2016).

21. Pietra, F. *et al.* Tuning the Lattice Parameter of In x Zn y P for Highly Luminescent Lattice-Matched Core/Shell Quantum Dots. *ACS Nano* **10**, 4754–4762 (2016).

22. Xie, R., Li, Z. & Peng, X. Nucleation kinetics vs chemical kinetics in the initial formation of semiconductor nanocrystals. *J. Am. Chem. Soc.* **131**, 15457–15466 (2009).

23. Mushonga, P., Onani, M. O., Madiehe, A. M. & Meyer, M. Indium phosphide-based semiconductor nanocrystals and their applications. *J. Nanomater.* **2012**, (2012).

24. Molina, P., Vasyliev, V., Vllora, E. G. & Shimamura, K. Tb 3+-Yb 3+ cooperative down and up conversion processes in Tb 0.81Ca 0.19F 2.81:Yb 3+ single crystals. *J. Appl. Phys.* **110**, (2011).

25. Ye, S., Zhu, B., Chen, J., Luo, J. & Qiu, J. R. Infrared quantum cutting in Tb3+, Yb3+ codoped transparent glass ceramics containing Ca F2 nanocrystals. *Appl. Phys. Lett.* **92**, (2008).

26. Zhang, Q. Y., Yang, G. F. & Jiang, Z. H. Cooperative downconversion in GdAl3(BO3)4: RE3+, Yb3+ (RE=Pr, Tb, and Tm). *Appl. Phys. Lett.* **91**, (2007).

27. Liu, X. *et al.* Cooperative downconversion and near-infrared luminescence of Tb 3+-Yb3+ codoped lanthanum borogermanate glasses. *Appl. Phys. B Lasers Opt.* **96**, 51–55 (2009).

Chapter 6. Cation Exchange in CuInS2 quantum Dots toward CuInS2@ZnS core@shell systems with Tunable Photoluminescence emission

Abstract

Ternary semiconductors NCs such as I-III-VI_2 type chalcopyrites ($CuInSe_2$-CISe, and $CuInS_2$-CIS) represent potential alternative materials to the Cadmium-based systems discussed in Chapter 4. This particular family of NCs can be prepared with different band gap not only by changing the size but also by varying the stoichiometry of the constituting elements. In this Chapter Copper Indium Sulfide NCs are prepared using a single-step heating-up method relying on the low thermal stability of the ter-dodecanethiol used as stabilizing agent, as solvent and as sulfur precursors. The obtained particles exhibit an emission varying from 710 to 940 nm. This range depends on the duration of the heating time (pre-heating) before the threshold temperature of 230°C for the growth process of ternary semiconductor NCs.

6.1 Introduction

As mentioned in previous chapters (Chapter 1) colloidal (NCs) have tunable optical transitions through manipulation of their size, shape, and surface. They are extremely promising for applications in many different areas[1–3] as optoelectronic devices working from the visible[2,4] to the near-infrared[1,5,6,7]and mid-infrared[8,9] spectral ranges. Examples of materials used to prepare these NCs are: CdTe (Chapter 4), CdSe, HgS, and PbS. Recently, the research interest had focus on alternative materials which do not contain toxic heavy metals such as Cd, Pb, As or Hg, and that offer a high flexibility for tuning band gap [10–12] (Figure 6.1 (a)). Ternary and multinary metals-chalcogenide materials are extensively investigated, i.e. $AgInS_2$,[13]$CuInSe_2$ (CISe)[7,13] and $CuInS_2$ (CIS)[3,10,13,14] because of their relative narrow bandgap values of 1.53 eV (CIS) and 1.05 eV (CISe) (see Figure 6.1 (b)), large absorption coefficients ($\alpha \sim 105$ cm^{-1})[7], PL emission ranging from the visible up to the NIR, large stoke shift, long stability of PL emission [15,16]and high QY. These classes of NCs have been studied for more than twenty years for biological *in vivo* imaging application, [10,17–19] solar power conversion [14,20,21] and light emitting diodes. [2,21,22]

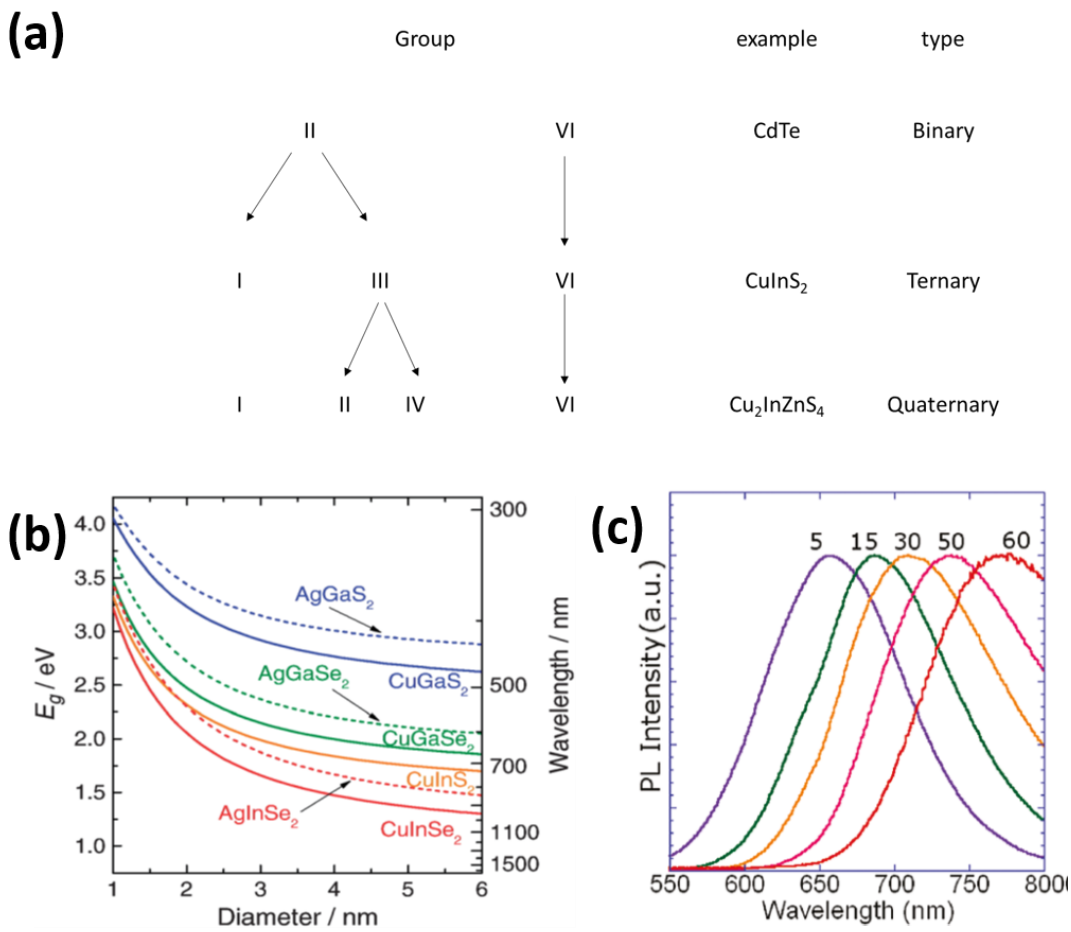

Figure 6.1. (a) Relationship between group II–VI, I–III–VI and I–II–IV–VI semiconductors. (b) evolution of the band gap with size for chalcopyrite type I-III-VI_2 semiconductor NCs using finite-depth-well effective mass approximation. (Adapted from Dmitry Aldakov *et al*. 2010 [7]) (c) Evolution of emission spectra during a typical synthesis, with numbers corresponding to reaction time in minutes. (from Liang Li *et al*., 2010 [23])

In particular, copper based I-III-VI systems have attracted great interest for their environmental compatibility, potential lower costs and very wide range of compositions and crystal structure. In contrast to other binary semiconductors, they show a certain degree of off-stoichiometry tolerance. This latter enables to avoid the formation of deep trap states that compromise the use of these materials. In fact, a pair of copper vacancies ($2\ V^{-}_{Cu}$) defects can balance the Indium (In^{+}_{Cu}) anti-site defects, thus removing the deep trap levels[23]. These copper vacancies can also be exploited as strategy to obtain a self-doped material, i.e. a p-type (Cu-enriched) or an n-type (In-enriched) doped compound (depending on its stoichiometry). Consequently it's possible to modulate the conductivity and realize CIS (or CISe) homojunction solar cell.[7]Also, the photoluminescence emission in CIS NC (see Figure 6.1) is

tuned from visible to NIR regions by increasing the size of the NCs and by tuning their stoichiometry changing the copper content.[23] Besides this, the ionic crystal lattices make them good candidates for cation exchange reactions. The incorporation of Cd, Zn, Sn or Ga is straightforward resulting in quaternary systems with further tuning of the bandgap and the PL QY.[11,12,24]

The copper-based chalcogenide compounds exhibit in the bulk the chalcopyrite crystal structure at room temperature, and zinc blende (ZB) and wurtzite (WZ) configuration are only stable at high temperature.[10,7,25] Their nanocrystalline forms, by contrast, can exhibit ZB and WZ configuration also at room temperature[7,14] (see Figure 6.6.2).

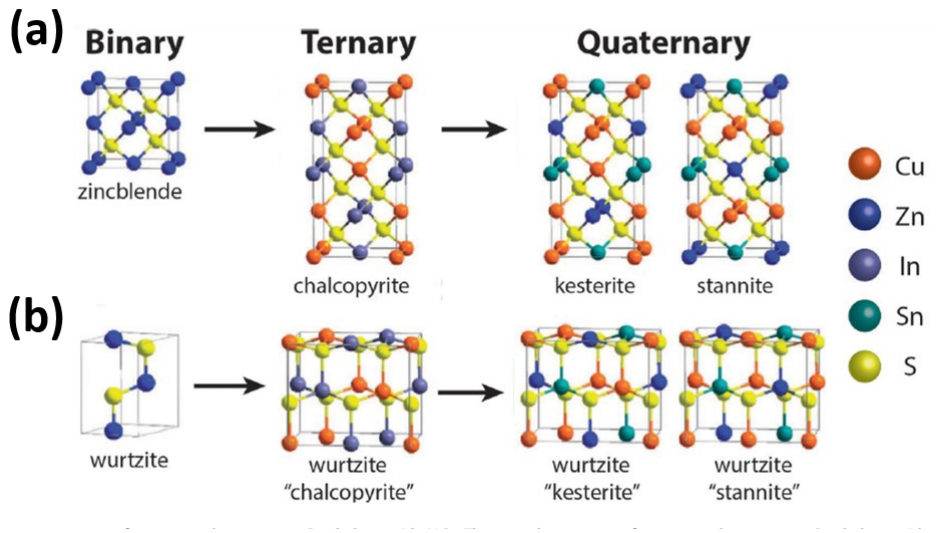

Figure 6.6.2. Crystal structures of ternary and quaternary copper chalcogenide NCs which derives from that of the binary analogues (a) if the binary NCs have a zinc blende structure, the resulting ternary present a chalcopyrite structure whilst the quaternary NCs present stannite or kerestite structure (b) if ternary compounds are developed on wurtzite structure, the resulting NCs also have a wurtzite from Chenghui Xia *et al.,* 2013) [26]

For all these reasons, this type of NCs has a large interest among ternary and quaternary systems. However, the synthesis of colloidal ternary NCs as CIS of controlled size, shape, composition is currently a topic of a very active research because it is still underdeveloped compared to II-VI and Copper Chalcogenide NCs and has yet to reach the same level of mastery. The reason is that the reactivity of the three precursors has to be finely balance in order to avoid the formation of binary $Cu_{2-x}S$ NCs (instead of $CuInS_2$) and this makes the control on the nucleation and growth rates of CIS NCs more challenging.

Several approaches have been investigated to synthesize CIS NCs. Chenghui Xia *et al.* started from a template of $Cu_{2-x}S$ then converted into CIS by partial cation exchange of Cu^{+} to In^{3+}.[10] This strategy may overcome the difficulty in balancing the reactivities of multiple precursors (In, Cu, S) allowing a precise control over the final composition of the NCs. Unfortunately, this protocol is very time-consuming (the reaction takes 3 days [10]) and it is thus not well suited for the preparation of a large number of different samples. Other groups used a direct synthesis for CIS NCs, by hot injection or heat-up synthesis. In the first method a sulfur source solution of 1-dodecanthiol (1-DDT) and tert-dodecanthiol (t-DDT) was rapidly injected into the mixture solution of Cu (I) and In (III) in oleic acid and oleylamine.[18] Because of the higher reactivity of the Cu monomers compared to indium in solution, copper sulfide seeds were obtained. The reasons for this are two-fold: (i) oleic acid (hard Lewis base) stabilizes efficiently the indium cations (hard Lewis acid) (ii) t-DDT is a soft Lewis base which binds to copper cations in a copper thiolate complex which presents a relatively low thermal stability and decomposes to copper sulfide at around 100°C.[13,14,18,27] Despite the good shape control, hot-injection synthetic methods to produce NIR emitting CIS are not well suited for large-scale production. This because their synthesis depends on the fast precursors' injection to induce nucleation and/or produce large amounts of waste solvent. [23]Thus, the most common alternative direct synthesis protocol of CIS is the heating-up approach. It consists in a mixture of copper iodide or acetate, CuI or Cu(Ac), indium acetate, $In(Ac)_3$,as cationic precursors, and tert-dodecanethiol (t-DDT)[18,25,28,29 which] plays the multifunctional role of sulfur source, ligand and solvent. Anyway, in the heat-up approach, the exact formation mechanism of colloidal CIS NCs is still under debate. Recent studies presented the evidence that the CIS NCs are grown by two stages of reaction: i) the in situ nucleation of Cu_2S as seeds particles [30,31,32] ; ii) at around 230°C, when CIS nucleates on the seed NCs, the growth takes place at the heterointerface between the two materials[14] (see Figure 6.3 (a)). Increasing the reaction time after the growth begins, the Cu_2S seed particles disappear from the $CuInS_2$ due to the high diffusivity of copper in the anionic lattice. [7,31]

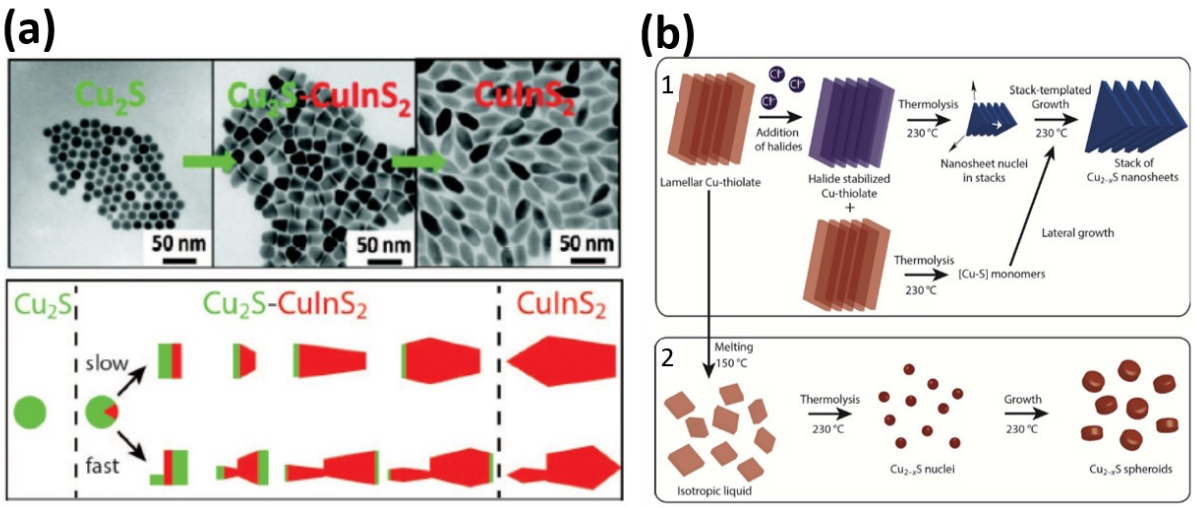

Figure 6.3. (a) growth mechanism of CIS NCs: the first Cu_2S NCs nucleate after, a small domain of CIS nucleates heterogeneously onto the Cu_2S seeds. From Ward van der Stam *et al.* [14] (b) schematic formation mechanism of $Cu_{2-x}S$ (sheets or spheroids) in presence(1) or in absence (2) of Chloride. From Ward van der Stam *et al.* [33]

Several papers have suggested that the CIS formation can be a attributed to a pre-generation step in which an intermediate copper-thiolate $Cu(SR)_x$ complex [26,27] is formed. Cu alkanethiolates are self -assembled supramolecular compounds that take the form of lamellar phase templates [34–36] with its inter-layer distance equal to the spacing of a bilayer of C12 alkyl chains.[30] Cu-alkythiolates complexes has a relatively low thermal stability and it are known to melt into a columnar mesophase at low temperature (143.5 °C for Cu-DDT) leading to monomer conversion into Cu_2S nuclei.[18,30,33] Bryck and Van der Stam *et al.* [26,27] suggested that the Cu-S bond increase the energetic barrier for C-S bond thermolysis in the lamellar phase stability requiring higher temperature to CIS formation. Moreover the authors suggested that an addition of halides elements, such as Cl^- or I^- , will reinforce the in-plane attractive forces further increasing the decomposition energetic barrier and the anisotropic nucleation and growth along the Cu-S planes, resulting in nanosheet formation [27,30](see Figure 6.4). For all these reasons, it appear clear that the capping agent play a decisive role in this process stability of the Cu(SR)x intermediate plays a crucial rule in its decomposition[26] affecting the reaction temperature or the resulting CIS NCs largely depends on the size of the Cu_2S seeds.

In these reactions, the lamellar copper- thiolate complexes remain intact beyond the Cu_{2-x} S nucleation threshold (230°C).

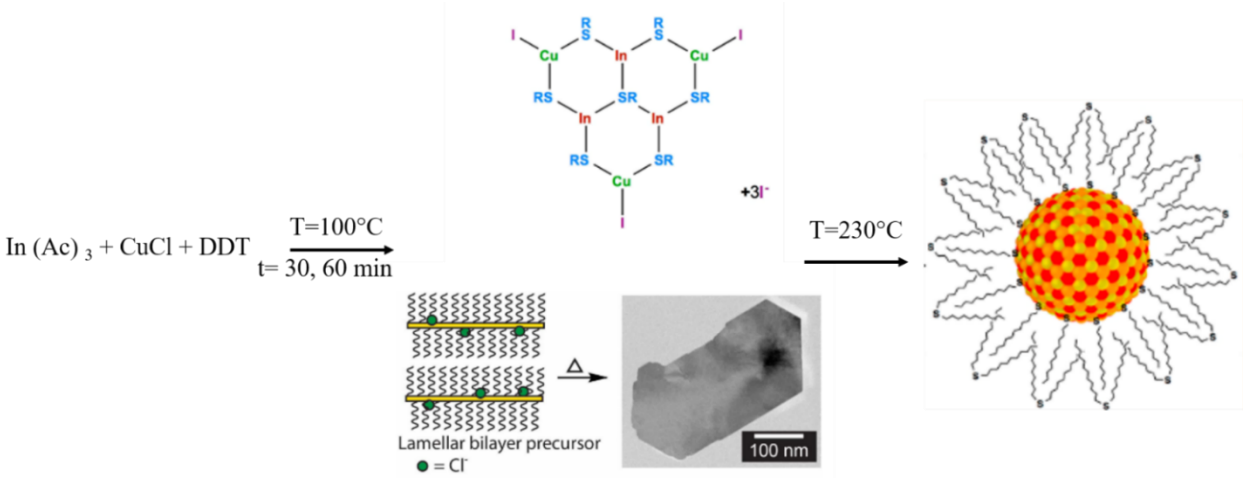

Figure 6.4. Schematic representation of intermediate product formed during the complexation stage with DDT at low temperature and hypothetical structure corresponding complexation of the metal precursors resulting in their coordination by thiolate molecules according to Bryk *et al.* and M. Gromova *et al.* The product of long pre-heating at 100-120°C is the complexation by thiolate molecules of metal precursors.

Yet, many aspects related to the reaction mechanism and surface passivation of the NCs still remain elusive to date. Among the open questions, the effect of the intermediate product formed during the complexation stage and the pre-heating time of the degassing on the reaction kinetics, as well on the PL emission wavelength of the subsequently formed NCs. Here, we address one of these questions, in particular, the influence of heating time at 100°C (pre-heating) before the threshold temperature of 230°C on the growth process of CIS nanocrystals exploiting the decomposition of copper thiolate complexes. Gromova *et al.* provided a new approach to elucidate what happens in the pre-nucleation step and evidenced that a good control over this stage plays a pivotal role in PL emission modulation in NIR. In the first part of this chapter, we demonstrate that is possible to optimize a fine-tuning of the emission wavelength of CIS NCs just acting on the pre-heating time and avoiding multiple hot injections. Afterwards, we exploit cation exchange reaction once again to growth a ZnS inorganic shell to enhance the NCs surface protection and then their PL QY and stability. We show that by changing its thickness (by tuning the Zn precursor amount), we are able to precisely tune the PL emission of the final stable NCs. The novelty of this approach lays in the fact that is possible to achieve emission in the NIR

spectral region by a simple heat up methods. Indeed, although Van der Stam *et al. had* already demonstrated the NIR emission in dot-in rod CuInS2/CuInSe2 core@shell NCs, though not fully investigated, and Leach et al. had observed a NIR emission at 950 nm in WZ-CIS NCs, hot injections methods were still used. Finally, these methods can be implemented into scale up synthesis to obtain system with a precise final emission wavelength.

6.2 Experimental Part

6.2.1 Synthesis of CuInS2 Nanocrystals

CIS NCs were synthesized following the heat-up technique. The synthesis has been performed in two phases consisting in (1) the complexation and seeding of Cu_2S nuclei at 100-120°C and (2) the CIS nucleation and growth at 230°C. We used a mixture of copper iodide (0.4 mmol) and indium acetate (0.4 mmol) as cationic precursors, and tert-dodecanethiol (t-DDT, 5 ml) served as the main sulfur source, due to its easy thermal decomposition[12] and its simultaneous ligand stabilization. The reaction mixture was degassed at 120°C and then, under nitrogen, this temperature was maintained for different intervals ranging from 1h to 5h before rising the temperature to 230°C. After 5- 50 minutes, depending on desired size, the nanocrystals were cooled back down to room temperature. The CIS QDs were purified by centrifugation. The final solution of CIS QDs was added with toluene and excess ethanol. The toluene and ethanol form an azeotrope, allowing for the removal of unreacted reagents and byproducts. The CIS QDs are however not soluble in the solution and crash out forming a precipitated at the bottom. The centrifuged solution was re-suspended in toluene. The benefit of the heat-up method is its potential for up-scaling of the NCs.

6.2.2 Synthesis of CuInS2 @ZnS Nanocrystals

For the growth of a ZnS shell, we used zinc stearate as Zn precursor, mixed with ODE and TOP, whilst we used t-DDT as sulfur precursor.

The exchange with Zn^{2+} cations was performed after growing with 4h of pre-heating CIS NCs at 260°C for 30 min with 4h of pre-heating. Specifically, the crude solution obtained from the synthesis was heated at 120°C. We studied different Zn: In molar ratios of 0.8:1, 1.5:1 and 2:1.

after which the flask was cooled to room temperature and the NCs were then separated by addition of ethanol followed by centrifugation. The NCs were washed three times by repeated dissolution in toluene and re- precipitation in ethanol.

6.3 Results and Discussion

Figure 6.4 shows the pre nucleation step according to M. Gromova *et al* [30]*:* in particular, nucleation stage requires the availability of sulfur ions, which are generated by the decomposition of DDT molecules. Long preheating at 100°-120°C has the effect of to lead to an accomplishment of the complexation of the metal precursors by thiolate molecules. This favors the lamellar template to lead anisotropic nucleation and growth along the Cu-S planes cleavage of S-C bond and then it gives sulfur availability during thermolysis and CIS nucleation that starts at 170°C. Thus, longer pre-heating changes the kinetics of the reactivity of sulfur precursor leading to larger nuclei. However, what is not clear is how to exploit this mechanism. For these reasons, we studied the effect of extending the pre-heating time.

Figure 6.5 illustrates the optical absorption and photoluminescence spectra of $CuInS_2$ NCs, where the absorption spectrum shows the typically nearly featureless profile of ternary quantum dots[30]. The absorption spectrum exhibits a weak shoulder at ~570 nm, indicating the position of the quantum dot band-edge. The emission peak is centered at 730 nm, suggesting a wide Stoke shift, which exceeds that of the standard core CdSe[3738], PbS[39] or PbSe[40]quantum dots where it usually a few nm. This is a general characteristic of I-III-VI_2 systems of pure CIS and CISe and their alloy composition.

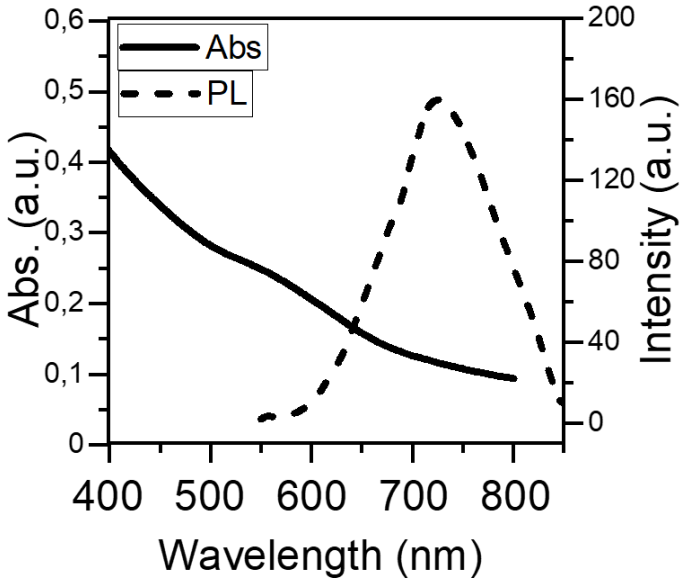

Figure 6.5. UV-vis absorption and emission (dashed line) spectra of CIS particles in toluene solution resulting from 1h at 120°C of preheating time. The mixture was heated to 230°C. Photoluminescence was measured using an excitation wavelength of 400 nm

TEM micrographs in Figure 6.6 show the size evolution for different stages of the reaction with 1 h of pre-heating, conducted at 230°C leading to the formation of quasi-prismatic NCs. 5 minutes after the growing temperature (T_G) is set at 230°C, the mean diameter is 1.7 nm. The XRD pattern of these samples is biphasic and can be assigned to Cu_2S and WZ CIS. The incorporation of indium in Cu_2S seeds has been confirmed by ICP-OES with a large excess of sulfur likely originated from thiols present on the surface of the NCs. In the subsequent stages of the reaction, the composition changes from copper rich (at minutes 5) to a final compound with a stoichiometry of $Cu_{0.9}$ $In_{0.9}S_2$. This is close to the expected value for copper indium disulfide, in a partial topotactic Cu for In cation exchange (CE). The XRD corroborates that the CIS formation is completed within 50 minutes at 230°C.

The result of these measurements can be directly compared to the reactions with higher pre-heating time described in the next sections of this chapter. In fact, all of them were performed under the same conditions, namely, the same molar ratio of precursors and the same growth temperature.

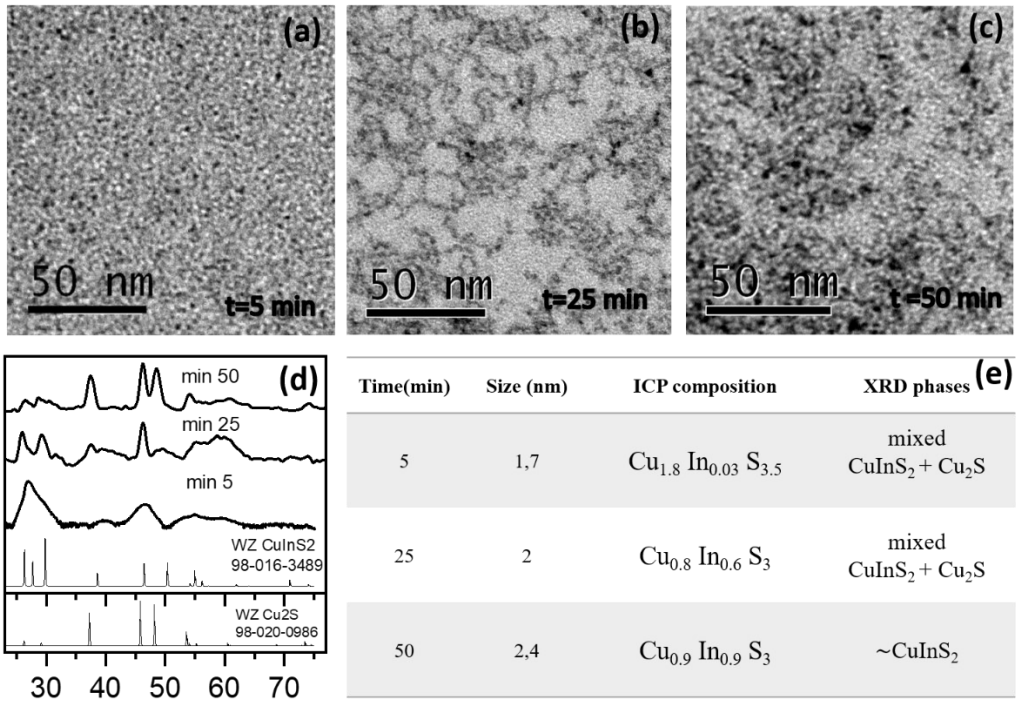

(e)

Time(min)	Size (nm)	ICP composition	XRD phases
5	1,7	$Cu_{1.8}\ In_{0.03}\ S_{3.5}$	mixed $CuInS_2 + Cu_2S$
25	2	$Cu_{0.8}\ In_{0.6}\ S_3$	mixed $CuInS_2 + Cu_2S$
50	2,4	$Cu_{0.9}\ In_{0.9}\ S_3$	~$CuInS_2$

Figure 6.6. (a,b,c) Overview TEM images of particles obtained in reaction at 230°C with 1h of pre-heating. (a) 5 min (b) 25 min (c) 50 min. Cu:In:S ratio calculated by ICP-OES are reported on the images (d) XRD pattern of aliquots taken from the reaction mixture at 230°C with 1h of pre-heating at 120°C at different reaction times together with the reference XRD pattern for Cu2S and CIS. (e) size, composition and crystallographic phases of CIS NCs prepared with 1 h of degassing at different reaction time. CIS composition was measured by ICP. The size was measure by TEM microscope.

6.3.1 Effect of the pre-heating time

Based on the assumptions reported above, we expect that increasing the pre-heating time (time during which the mixture is kept at 120° C), we could obtain larger sheets of lamellar Cu_2S seeds and, thus, larger CIS NCs products. This can be confirmed comparing the results with the experiment performed with 1h of pre-heating. As mentioned above, taking into consideration Bryck *et al.* and Gromova *et al.* studies, [30] we expect that Cu_2S seeds NCs begin to form from Cu-S lamellar phase when the temperature is held at 120°C for long time. We also expect that the lamellar supramolecular order phase become bigger. Afterwards, as soon as the temperature reaches 230°C, the consecutive CIS will be generated on big sheets with interesting effects on the wavelength of the emission.

To better understand the effect of the pre-heating time, samples were collected as soon they achieved the growth temperature and characterized by TEM, XRD, ICP-OES and by optical spectroscopy.

TEM was used to investigate the size evolution of CIS NCs. Figure 6.7 shows the diameter of the quasi prismatic $CuInS_2$ NCs that were obtained after various pre-heating times at 120°C. Their diameters, respectively of 2.5 nm, 7 and 10 nm correspond to the diameter of CIS NCs as corroborated by XRD diffractograms with a wurtzitic crystal structure (for 3h, 4h and 5 h of pre-heating, respectively). In addition to that, the NCs exhibits a composition richer in indium with respect to the sample at "shorter" pre-heating time of 1h, being $Cu_{0.3}In_{0.6}S_{3.7}$ for 3h of pre-heating and $Cu_{0.7}In_{0.7}S_{2.8}$ for 5 h. In all the cases, the particles are sulfur rich. This can be related to the presence of thiols in the ligand shell. Consistently with the increasing particles size of NCs, the photoluminescence (PL) emission spectra red shifts (see Figure 6.7 (e)) with the emission of CIS NCs peak from 710 nm after just 1 hour of pre-heating up to 940 nm after 5 hours. The PL

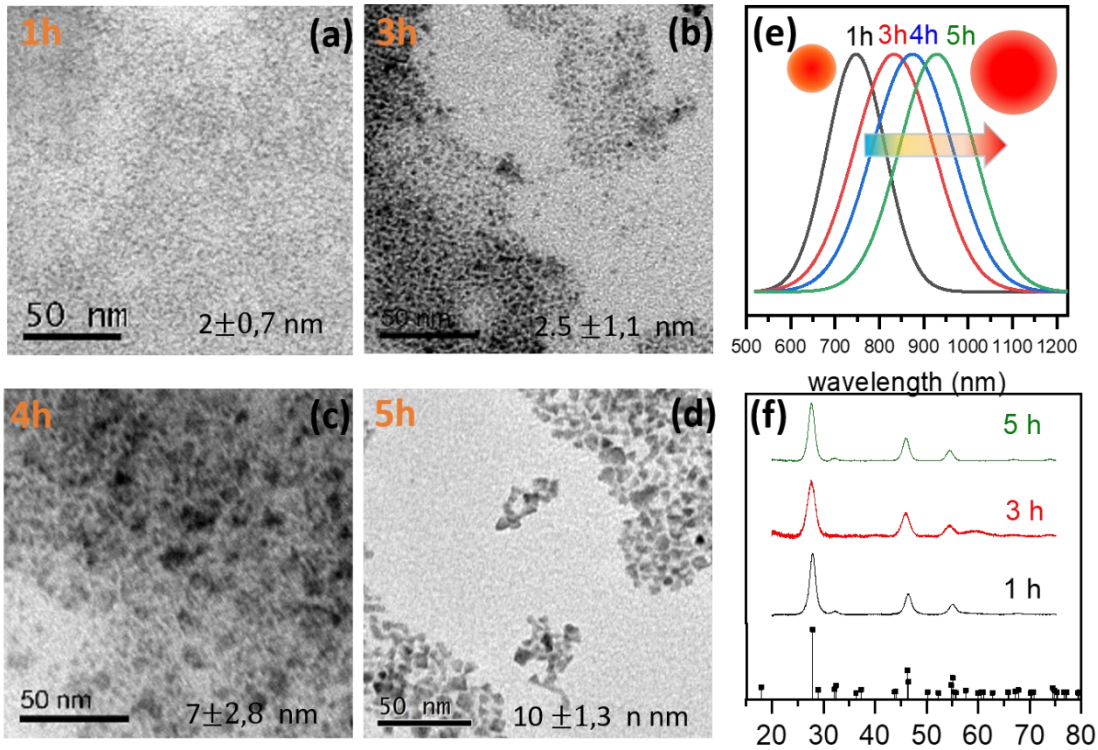

Figure 6.7. CIS TEM images as soon as they achieved 230 ° C with varying preheating time length. In particular after (a) 1h (b) 3 h (c) 4 h (d) 5h.(e) PL emission measurements of CIS particles obtained at 230°C for different duration of pre-heating time: 1h (black curve), 3h (red curve), 4h (blue curve), 5h (green curve). (f) XRD patterns of CIS particles obtained with different pre-heating treatment. Reference: Roquesite ICSD:98-062-8063

properties of the resulting NCs were found to be strongly dependent on the pre-heating time while the other reaction parameters, such as reaction temperature (120°C), the amount of DDT, and Cu:In ratio were kept constant.[12,10] Considering the obtained results, it seems that the pre-heating time plays a pivotal role in CIS formation. It is possible to suppose that the Indium incorporation in NCs stoichiometry starts as soon as the temperature reaches 230°C. We speculate that Cu_2S seeds form and growth during the preheating time at 120°C, while this is reported to occur typically at 230°C [18,30]. This helps us to understand and use the underlying growth mechanism to control the PL properties of the resulting NCs. Such a process is quite different from previous reports on the preparation of CIS NCs with a similar solvothermal method [7,10,26,27,29,30,41] where the Cu_2S seeds formation and CIS growth were observed only once the temperature of 230°C was reached. The novelty of this study is that Cu_2S seeds formation and growth has exploited by means of long pre-heating time. Moreover, for the first time a red-shifted emission up to 940 nm with a simple heat-up synthesis has been achieved Figure 6.7. This demonstrates the simplicity of this procedure, which consists to keep growing the core till 10 nm without further precursors injection in an easy one-step preparation.

6.3.2 Effect of the CuIn:Zn ratio

Once the growth of CIS NCs has been investigated, the next step was to enhance the QDs stability by a ZnS overcoating. This was performed by means of cation exchange of $CuInS_2$ NCs with Zn cations. This secondary crystalline growth passivates surface defects where the charge carriers can be trapped or can relax non-radiatively. In this way the PL QY can be increased. $CuInS_2$ and ZnS have similar crystallographic structures, and the lattice mismatch between the two materials is only 2.2%[12,19,42]; therefore, copper and indium ions can be easily replaced by zinc ions, and homogeneous alloys can be produced. In doing this, however, we expect a blueshift of the PL because the band gap of bulk ZnS (3.6 eV) is substantially higher than that of CIS (1.5 eV), it is reasonable to observe that the PL band gap of the obtained CuInS2@ZnS NCs is higher than the bare CIS.

The exchange with Zn^{2+} cations was performed after growing with 4h of pre-heating CIS NCs at 260°C for 30 min with 4h of pre-heating. Specifically, the crude solution obtained from the synthesis was heated at 120°C (still under inert atmosphere) and then a solution of zinc stearate

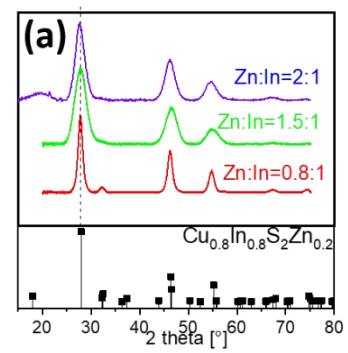

(b)

Zn:In precursor	CIS size (nm)	CIZS size (nm)	ICP composition	Blu shift (nm)
0,8	7±2,8	7,1 ± 2,2	$Cu_{0.8}\ In_{0.73}\ Zn_{0.45}\ S_2$	10
1,5	7±2,8	7,8 ± 1,2	$Cu_{0.38}\ In_{0.58}\ Zn_{0.81}S_2$	54
2	7±2,8	8,4±2	$Cu_{0.23}\ In_{0.9}\ Zn_{1.4}S_2$	70

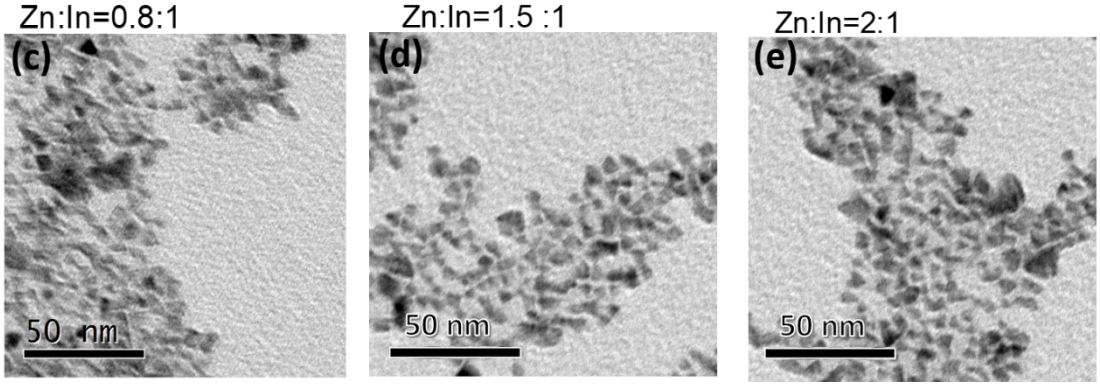

Figure 6.8. reaction temperature of 260°C after a preheating treatment of 4h at 120°C. (a) XRD patterns of CuInS@ZnS NCs obtained by partial cation exchange with Cu/In ions in a ratio of Zn:In of 0.8:1, 1.5:1 and 2:1 (b) CIZS composition measured by ICP. $\lambda_{em.}$ wavelength corresponding to the maximum of the emission peak exciting at 450 nm. (c) TEM images during partial cation exchange with Zn: In feed molar ratio of 0.8:1 (d) 1.5:1 (e) 2:1.

dissolved in ODE and TOP was added dropwise. The temperature was raised to 230°C for 45 minutes (this last step was crucial for improving the PL QY).We studied different Zn:In molar ratios of 0.8:1, 1.5:1 and 2:1. after which the flask was cooled to room temperature and the NCs were then separated by addition of ethanol followed by centrifugation. The NCs were washed three times by repeated dissolution in toluene and re- precipitation in ethanol. This procedure leaded to NCs with a quaternary composition. XRD diffractograms in Figure 6.8 correspond to $CIZS_2$ in the chalcopyrite phase, with a slight shift of the peaks corresponding observed for Zn:In=2:1. The significant variation of the CIZS NCs is the Cu stoichiometry, while the In:Zn and In:S ratios varied less (see Table in Figure 6.8).

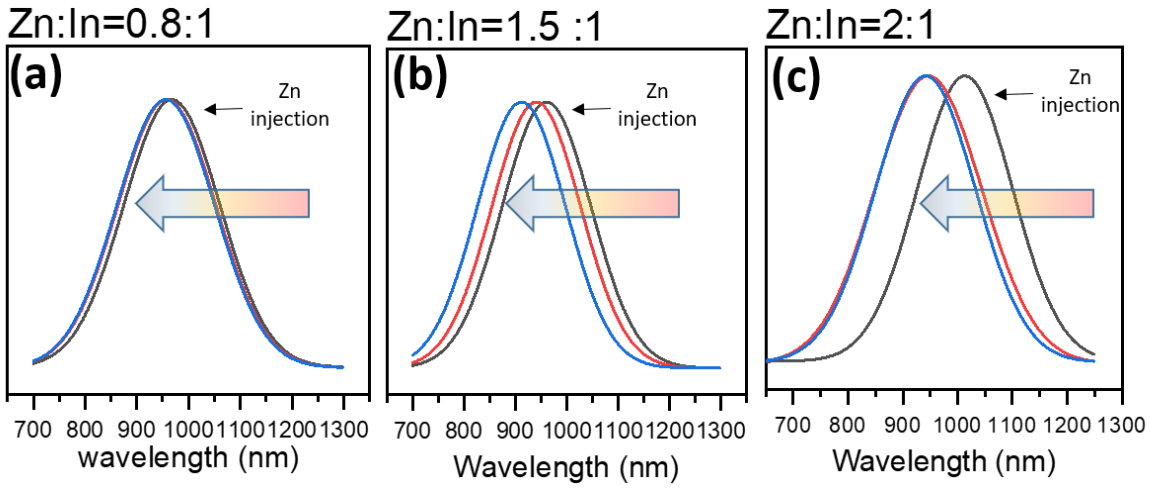

Figure 6.9. PL emission spectra during partial cation exchange with Zn: In feed molar ratio of 0.8:1 (d) 1.5:1 (e) 2:*1* The black curve corresponds to minutes 5 after Zn injection; red curve corresponds to minute 25 after Zn injections and blue curve corresponds to minutes 50 after the Zn injections

The PL spectra blue-shifted with respect to those of their parent CIS NCs. The shift was about 10 to 70 nm with variation of the Zn:In precursor ratio from 0.8 to 2 (see Figure 6.9). Spectral blue shifts have been invariably observed after ZnS shelling of CP CIS QDs and have been attributed to a number of reasons. For example, upon overgrowth of a ZnS shell using both Zn and S precursors was attributed to the etching of the core before the shell growth.[23] Exposing the CIS core to Zn precursors in the absence of a S precursor, as in this case, have been observed to induce even a larger blue-shifts[43]. A pronounced blue-shifts were demonstrated by previous studies [43,44] to be due to partial Zn^{2+} for In^{3+} and Cu^{+} CE followed by interdiffusion, resulting in gradient $(CuInZn)S_2$ alloy QDs with the same size as the parent CIS QDs but larger band gaps. The addition of mixed Zn and S precursors to core CIS leads to a simultaneous ZnS overgrowth and Zn interdiffusion resulting in core@shell NCs with gradient CIZS alloyed core and overcoated by a ZnS shell with a spectral blu-shift.[43,44]

It is interesting to note that in the case of Zn:In= 0.8:1 the blue shift is not remarkably, while the elemental analysis confirmed the Zn presence in the NCs. This may be associated with the case of the ZnS shell growth on the outer layer of the parent CIS with no change in the band gap. When increasing the Zn content, the blue shift is much more remarkable and uniform indicating that, in addition to the ZnS formation, the Zn must have diffused into the core. An additional increasing of the Zn amount, as in the last case in which Zn amount introduced was Zn:In =2:1,

lead to a blue shift which does not shift further after 25 minutes indicating that the Zn interdiffusion and alloying into the CIS core was complete.

As a result, the optical properties of CIS NCs with an average core size of 7 nm and emission around 940 nm, can be continuously tuned from those of core@shell to those of homogenously alloy NCs, with slight variation of the NCs size

However, it appears that more studies need yet to be done to validate this assumption, like the composition analysis as the elemental quantification by EDS to understand the shell thickness and Zn distribution into the core. Further support on the alloyed- core@shell composition may come by comparing high resolution XPS of the CIS NCs with those of the CISZ NCS. Moreover, the change of the PL decay times in the CIZS NCs with respect to the CIS NCs may also be helpful to understand the change of composition, i.e. a change of the ternary into a quaternary system.

6.4 Conclusions

My work focused on the study of the effect of the pre-heating treatment on the nucleation and growth stages of the $CuInS_2$ NCs synthetized using DDT and on the effects of the Zn introduction in such synthetized NCs. The bandgap of the CIS NCs can be tuned acting on the pre-heating time. The exact geometry of the stacks of Cu-dodecanethiolate formed at 100-120°C cannot be determined with the presently available data, however the photoemission measurements suggest that a CIS formation starts before the nucleation step and it must be connected to an increase of dissemble of stack lamellar Cu-DDT complexes at temperature below the C-S thermolysis. This induces a $Cu_{2-x}S$ nucleation at sufficiently high supersaturations leading to the formation of big CIS NCs as soon as the temperature achieve 230°C. Remains remarkably the simplicity of the growth induced by this simple step, in which the cleavage of C-S bond occurs and affect the availability of the S source. Since no one has reported in literature a 1040 nm emission avoiding multiple hot injections, our aim is to explore the PL emission modulation by tuning the preheating time. We also explored the effect of the ZnS shell growth around CIS core NCs by means of the cation exchange, to achieve control on a precise modulation of the PL. Thanks to the current results this strategy can be applied to some other I-II-VI_2 compounds, e.g., CuGaSe, $CuInSe_2$. Although this promising method may be considered to scale up the fabrication, obtaining a final stable system with a precise emission wavelength is still challenging and more studies are needed.

REFERENCES

1. Konstantatos G, Sargent EH. *Colloidal Quantum Dot Optoelectronics and Phtovotaics*. (G. Konstantatos ES, ed.).
2. Kagan CR, Lifshitz E, Sargent EH, Talapin D V. Building devices from colloidal quantum dots. *Science (80-)*. 2016;353(6302). doi:10.1126/science.aac5523
3. Talapin D V., Lee JS, Kovalenko M V., Shevchenko E V. Prospects of colloidal nanocrystals for electronic and optoelectronic applications. *Chem Rev*. 2010;110(1):389-458. doi:10.1021/cr900137k
4. Ning Z, Dong H, Zhang Q, Voznyy O, Sargent EH. Solar cells based on inks of n-type colloidal quantum dots. *ACS Nano*. 2014;8(10):10321-10327. doi:10.1021/nn503569p
5. Gupta S, Kershaw S V., Susha AS, et al. Near-infrared-emitting CdxHg1-xSe nanorods fabricated by ion exchange in an aqueous medium. *ChemPhysChem*. 2013;14(12):2853-2858. doi:10.1002/cphc.201300084
6. Rogach AL, Eychm??ller A, Hickey SG, Kershaw S V. Infrared-emitting colloidal nanocrystals: Synthesis, assembly, spectroscopy, and applications. *Small*. 2007;3(4):536-557. doi:10.1002/smll.200600625
7. Aldakov D, Lefrançois A, Reiss P. Ternary and quaternary metal chalcogenide nanocrystals: Synthesis, properties and applications. *J Mater Chem C*. 2013;1(24):3756-3776. doi:10.1039/c3tc30273c
8. Chen M, Guyot-Sionnest P. Reversible Electrochemistry of Mercury Chalcogenide Colloidal Quantum Dot Films. *ACS Nano*. 2017;11(4):4165-4173. doi:10.1021/acsnano.7b01014
9. Guyot-Sionnest P. Electrical transport in colloidal quantum dot films. *J Phys Chem Lett*. 2012;3(9):1169-1175. doi:10.1021/jz300048y
10. Xia C, Meeldijk JD, Gerritsen HC, De Mello Donega C. Highly Luminescent Water-Dispersible NIR-Emitting Wurtzite CuInS2/ZnS Core/Shell Colloidal Quantum Dots. *Chem Mater*. 2017;29(11):4940-4951. doi:10.1021/acs.chemmater.7b01258
11. Lox JFL, Dang Z, Lê Anh M, Hollinger E, Lesnyak V. Colloidal Cu-Zn-In-S-Based Disk-Shaped Nanocookies. *Chem Mater*. 2019;31(8):2873-2883. doi:10.1021/acs.chemmater.9b00005
12. Li J, Parisi J, Kolny-Olesiak J. Synthesis of CuInS2-ZnS Alloyed nanorods and hybrid nanostructures. In: *Materials Research Society Symposium Proceedings*. Vol 1780. ; 2015:7-16. doi:10.1557/opl.2015.771
13. Zhong H, Bai Z, Zou B, Colloidal I. Tuning the Luminescence Properties of III–Nanocrystals for Optoelectronics and Biotechnology Applications. *Chem Lett*. 2012;3 SRC-G:3167-3175.
14. Van Der Stam W, Berends AC, De Mello Donega C. Prospects of Colloidal Copper Chalcogenide Nanocrystals. *ChemPhysChem*. 2016;17(5):559-581. doi:10.1002/cphc.201500976
15. Kolny-Olesiak J. Synthesis of copper sulphide-based hybrid nanostructures and their application in shape

control of colloidal semiconductor nanocrystals. *CrystEngComm*. 2014;16(40):9381-9390. doi:10.1039/c4ce00674g

16. Wang H, Butler DJ, Straus DB, et al. Air-stable CuInSe2 nanocrystal transistors and circuits via post-deposition cation exchange. *ACS Nano*. 2019;13(2):2324-2333. doi:10.1021/acsnano.8b09055
17. Song WS, Yang H. Efficient white-light-emitting diodes fabricated from highly fluorescent copper indium sulfide core/shell quantum dots. *Chem Mater*. 2012;24(10):1961-1967. doi:10.1021/cm300837z
18. Li J, Bloemen M, Parisi J, Kolny-Olesiak J. Role of copper sulfide seeds in the growth process of CuInS2 nanorods and networks. *ACS Appl Mater Interfaces*. 2014;6(22):20535-20543. doi:10.1021/am5061454
19. Hessel CM, P. Pattani V, Rasch M, et al. Copper selenide nanocrystals for photothermal therapy. *Nano Lett*. 2011;11(6):2560-2566. doi:10.1021/nl201400z
20. Taylor RA, Ramasamy K. Colloidal quantum dots solar cells. *SPR Nanosci*. 2017;4:142-168. doi:10.1039/9781782620358-00142
21. Kolny-Olesiak J, Weller H. Synthesis and application of colloidal CuInS2 semiconductor nanocrystals. *ACS Appl Mater Interfaces*. 2013;5(23):12221-12237. doi:10.1021/am404084d
22. Liu Y, Gibbs M, Puthussery J, et al. Dependence of carrier mobility on nanocrystal size and ligand length in pbse nanocrystal solids. *Nano Lett*. 2010;10(5):1960-1969. doi:10.1021/nl101284k
23. Li L, Pandey A, Werder DJ, Khanal BP, Pietryga JM, Klimov VI. Efficient Synthesis of Highly Luminescent Copper Indium. *J Am Chem Soc*. 2011;133:1176-1179.
24. Wang X, Pan D, Weng D, et al. A general synthesis of Cu-In-S based multicomponent solid-solution nanocrystals with tunable band gap, size, and structure. *J Phys Chem C*. 2010. doi:10.1021/jp103572g
25. Bujak P. Core and surface engineering in binary, ternary and quaternary semiconductor nanocrystals—A critical review. *Synth Met*. 2016;222(2015):93-114. doi:10.1016/j.synthmet.2016.04.002
26. Chang J, Waclawik ER. Controlled synthesis of CuInS2, Cu2SnS3 and Cu2ZnSnS4 nano-structures: Insight into the universal phase-selectivity mechanism. *CrystEngComm*. 2013;15(28):5612-5619. doi:10.1039/c3ce40284c
27. Bryks W, Lupi E, Ngo C, Tao AR. Digenite Nanosheets Synthesized by Thermolysis of Layered Copper-Alkanethiolate Frameworks. *J Am Chem Soc*. 2016;138(41):13717-13725. doi:10.1021/jacs.6b08264
28. De Trizio L, Prato M, Genovese A, et al. Strongly fluorescent quaternary Cu-In-Zn-S nanocrystals prepared from Cu 1-xInS 2 nanocrystals by partial cation exchange. *Chem Mater*. 2012;24(12):2400-2406. doi:10.1021/cm301211e
29. Zhong H, Zhou Y, Ye M, et al. Controlled synthesis and optical properties of colloidal ternary chalcogenide CuInS2 nanocrystals. *Chem Mater*. 2008;20(20):6434-6443. doi:10.1021/cm8006827
30. Gromova M, Lefrançois A, Vaure L, et al. Growth Mechanism and Surface State of CuInS2 Nanocrystals Synthesized with Dodecanethiol. *J Am Chem Soc*. 2017;139(44):15748-15759. doi:10.1021/jacs.7b07401

31. Lu X, Zhuang Z, Peng Q, Li Y. Controlled synthesis of wurtzite CuInS2 nanocrystals and their side-by-side nanorod assemblies. *CrystEngComm*. 2011;13(12):4039-4045. doi:10.1039/c0ce00451k
32. Kruszynska M, Borchert H, Parisi J, Kolny-Olesiak J. Synthesis and shape control of CuInS2 nanoparticles. *J Am Chem Soc*. 2010;132(45):15976-15986. doi:10.1021/ja103828f
33. Van Der Stam W, Rabouw FT, Geuchies JJ, et al. In Situ Probing of Stack-Templated Growth of Ultrathin Cu2-xS Nanosheets. *Chem Mater*. 2016;28(17):6381-6389. doi:10.1021/acs.chemmater.6b02787
34. Sandhyarani N, Pradeep T. Current understanding of the structure, phase transitions and dynamics of self-assembled monolayers on two- and three-dimensional surfaces. *Int Rev Phys Chem*. 2003. doi:10.1080/0144235031000069705
35. Espinet P, Lequerica MC, Martín-Alvarez JM. Synthesis, structural characterization and mesogenic behavior of copper(I) n-alkylthiolates. *Chem - A Eur J*. 1999. doi:10.1002/(SICI)1521-3765(19990702)5:7<1982::AID-CHEM1982>3.0.CO;2-6
36. Levchenko AA, Yee CK, Parikh AN, Navrotsky A. Energetics of self-assembly and chain confinement in silver alkanethiolates: Enthalpy-entropy interplay. *Chem Mater*. 2005. doi:10.1021/cm050961i
37. Meinardi F, McDaniel H, Carulli F, et al. Highly efficient large-area colourless luminescent solar concentrators using heavy-metal-free colloidal quantum dots. *Nat Nanotechnol*. 2015;10(10):878-885. doi:10.1038/nnano.2015.178
38. Meinardi F, Colombo A, Velizhanin KA, et al. Large-area luminescent solar concentrators based on Stokes-shift-engineered nanocrystals in a mass-polymerized PMMA matrix. *Nat Photonics*. 2014;8(5):392-399. doi:10.1038/nphoton.2014.54
39. Stewart JT, Padilha LA, Qazilbash MM, et al. Comparison of carrier multiplication yields in PbS and PbSe nanocrystals: The role of competing energy-loss processes. *Nano Lett*. 2012;12(2):622-628. doi:10.1021/nl203367m
40. Semonin OE, Johnson JC, Luther JM, Midgett AG, Nozik AJ, Beard MC. Absolute photoluminescence quantum yields of IR-26 Dye, PbS, and PbSe quantum dots. *J Phys Chem Lett*. 2010;1(16):2445-2450. doi:10.1021/jz100830r
41. Pan D, An L, Sun Z, et al. Synthesis of Cu - In - S Ternary Nanocrystals with Tunable. *J Am Chem Soc*. 2008:5620-5621.
42. Mei S, Zhu J, Yang W, et al. Tunable emission and morphology control of the Cu-In-S/ZnS quantum dots with dual stabilizer via microwave-assisted aqueous synthesis. *J Alloys Compd*. 2017;729:1-8. doi:10.1016/j.jallcom.2017.09.133
43. Park J, Kim SW. CuInS2/ZnS core/shell quantum dots by cation exchange and their blue-shifted photoluminescence. *J Mater Chem*. 2011. doi:10.1039/c0jm03194a

44. Nam DE, Song WS, Yang H. Facile, air-insensitive solvothermal synthesis of emission-tunable CuInS2/ZnS quantum dots with high quantum yields. *J Mater Chem*. 2011. doi:10.1039/c1jm12437d

Final thoughts

Cation exchange (CE) reactions in colloidal nanocrystals have been widely studied in the last 25 years as a versatile tool to prepare nanoscale materials with diverse compositions, structures, and shapes without having to develop new synthetic methods to produce each individual nanostructure. We exploited this tool on colloidal semiconductor NCs belonging to II-VI, III-V and I-III-VI_2 types to tune their optical transition and modulate their PL emission from visible to the near-infrared (NIR).

Thus, in the first part, we studied CdTe NCs system (II-VI type) that is extensively used in bulk optoelectronics materials for its narrow band gap. $Hg^{2+} \rightarrow Cd^{2+}$ cation exchange (CE) reactions were used to transform colloidal CdTe nanocrystals (NCs, 4-6 nm in size) into CdTe@HgTe core@shell nanostructures. This was achieved by working under a slow CE rate, which limited the exchange to the surface of the CdTe NCs. The products of the CE were observed to evolve when annealed at temperature as low as 200°C. In this case the superficial Hg content was found much lower than that in the starting NCs, while the residual CdTe cores sintered with a concomitant removal of the native surface ligands. We used our CdTe@HgTe NCs ink to fabricate a proof-of-concept photodetector with a photoresponse up to 0.5 A/W. Anyway, considering (i) the temperature typically high (above 350°C) used for the fabrication of thin films of CdTe in photovoltaic technology and (ii) the post process ligand stripping steps, our novel strategy opens the door to include CE protocols as valid alternatives to lower the overall cost of the production. Clearly, if our procedure will be employed in the future, it would definitely require an assessment of the correlated environmental risks.

Subsequently we studied Cd-free systems like InP QDs. The aim was to develop a synthesis method to incorporate lanthanide ions into InP quantum dots and to demonstrate energy transfer from the InP host to the lanthanide dopant. For this purpose, the Yb^{3+}ions were chosen because of its luminescent efficiency is close to 100%. The incorporation of the lanthanide ion was investigated by changing the Yb:In molar employing a hot- injection method to synthetized InP and In(Zn)P colloidal semiconductor. To incorporate the Yb^{3+} dopant ions, the role of the length of the ligand used during doping was also explored. As an alternative doping method, a one pot synthesis route to dope InP or In(Zn)P NCs was utilized. The doping effect was evaluated by absorption, photoluminescence (PL) and elemental analysis ICP-OES. Our aim was to demonstrate the possibility of Yb^{3+} incorporation and its effectiveness of doping was verified

by elementary analyzes. Unfortunately, no emissions corresponding to the Yb^{3+} $^2F_{5/2} \rightarrow {}^2F_{7/2}$ transition wavelength were documented upon excitation. An option may be the energy transfer from the excited state of the NCs to the dopant ion is that large that need a sensitizer acting as a bridge among the two systems. A possible candidate is Eu^{3+}sensitizer, and subsequently Tb $^{3+}$–Yb $^{3+}$ [30,31], Pr $^{3+}$–Yb^{3+} [24,32], and Tm $^{3+}$–Yb^{3+} [33] systems. Up to now, we obtained only preliminary results and further measurements needs to be performed for a more deep understanding. It remains unclear if the Yb^{3+} ions reside at the nanocrystal surface in a sort of core@shell structure resulting in an excited state reduced by multi-phonon relaxation. A luminescent quantum yield calculation may provide insight of the efficiency of the energy transfer from the excited state of InP to the Yb^{3+} ions after excitation by means of an integrating sphere.

Finally, in the last chapter we reported a study on Copper Indium Sulfide nanocrystals (I-III-VI_2 type ternary semiconductor NCs) as potential alternative materials to Cd-based systems. They were prepared using a single-step heating-up method relying on the low thermal stability of ter- dodecanethiol used as stabilizing agent, solvent and sulfur precursors. The aim of this project was to obtain a fine tuning of the PL emission by Zn introduction in CIS NCs through cation exchange (CE). However, the data suggested that the bandgap of the CIS NCs can be conveniently tuned via variation of the pre-heating time where presumably the stack lamellar Cu-DDT complexes dissemble at below the C-S thermolysis. This induces a $Cu_{2-x}S$ nucleation at sufficiently high supersaturations leading to the formation of big CIS NCs as soon as the temperature achieve 230°C. The obtained particles exhibit an emission varying from 710 to 940 nm. The simplicity of this method suggests the potential preparation of NCs in up-scaled production. However, obtaining a final stable system with a precise emission wavelength is still challenging and more studies are needed.

In conclusion, several NCs syntheses have been developed exploiting cation exchange reaction to meet the requirements for the production of NIR semiconductor NCs. Yet, the appealing challenge for cation exchange is to produce a technologically relevant high-quality material that is complicated to produce by other means. The steep learning curve in this field is in rapid progress and lead to expect further improvements.

Acknowledgements

Undertaking this PhD has been a truly life-changing experience for me and it would not have been possible to do without the support and guidance that I received from many people.

Firstly, I would like to express my sincere gratitude to my advisors Prof. Liberato Manna and Dr. Luca De Trizio for the opportunity to join their team and to have given me access to the laboratory and research facilities, for their support of my Ph.D study, for their patience, and immense knowledge. Their guidance helped me in all the time of research and writing of this thesis.

My sincere thanks also goes to Dr. Beatriz Martin-Garcia, Dr. Davide Spirito, for their serenity, their encouragement and their invaluable help: without your precious support it would not be possible to conduct this research.

My deep appreciation goes out to the IIT team members, in particular to S. Marras M. Prato for the technical support on the XRD and XPS data acquisition and interpretation.

I would also say thanks to Prof. M. Curri and to Prof. A. Cabot for their comments and suggestions that allowed me to improve my thesis.

My biggest thanks goes to my friends Den and Aym.: without your help this work would not have been achievable.

I thank my fellow labmates in for the stimulating discussions, for the sleepless nights we were working together before deadlines, and for all the fun we have had in the last years.

Last but not the least, I would like to thank my family for supporting me spiritually throughout writing this thesis and my my life in general.